CHAPTER VI

Accurate Prediction of Rotational Nonequilibrium Effects

During the initial development of the MPC hybrid method, the ability to simulate rotational nonequilibrium effects in the continuum module had not yet been incorporated. Therefore, not only did the hybrid interfaces need to be placed in regions of translational equilibrium, but also in regions where it could be accurately assumed that the translational and rotational energy modes were in equilibrium. In the one-dimensional shock wave study that was first performed using the MPC method [65], the gradient-length local Knudsen number with a threshold value of 0.05 was found to accurately position the pre-shock and post-shock hybrid interfaces, despite its inability to directly account for thermal nonequilibrium effects. However, it was noted in Ref. [65] that an additional parameter may be needed in future MPC hybrid simulations to specifically indicate regions of rotational nonequilibrium so that the particle module would be used rather than the continuum module. In a more recent study of transitional, hypersonic flow over a two-dimensional cylinder, Schwartzentruber, *et al.* [66] proposed the following parameter to be used in conjunction with the gradient-length local Knudsen number based on mass density, translational temperature, and velocity magnitude:

$$Kn_{ROT-NEQ} = 5 \times \frac{T_{trans} - T_{rot}}{T_{rot}}. \tag{6.1}$$

The parameter in Eq. 6.1 is reminiscent of the translational-rotational energy exchange source term of the rotational energy conservation equation introduced in Chapter II, and further detailed in Chapter IV. Because the difference between the translational and rotational temperatures drives the exchange of energy between these modes in the continuum module, it was proposed that this difference should also be used to predict rotational nonequilibrium. However, it does not capture the possibility of a nonequilibrium rotational EDF. The $Kn_{ROT-NEQ}$ parameter was found to be critical for accurately predicting the location of the post-shock hybrid interface in transitional, hypersonic, blunt-body flows. In order to avoid the use of another parameter, attempts were made to enlarge the particle region surrounding the shock by reducing the Kn_{GLL} threshold value. However, the resulting locations of the other hybrid interfaces were far too sensitive to the threshold value for this to be a viable option. Therefore, this new parameter was employed with the same threshold value of 0.05 so that hybrid interfaces were placed in regions where the relative difference between the translational and rotational temperatures was less than 1%.

Later, when a separate rotational energy equation was included in LeMANS [38], and the MPC method was extended to simulate rotational nonequilibrium effects in simple gases [22], the matter of predicting thermal nonequilibrium was revisited. Because the continuum domain accounted for differences between the translational and rotational temperatures, the coefficient in Eq. 6.1 was relaxed to a factor of 0.5. An additional gradient-length local Knudsen number was also calculated with respect to the rotational temperature because of the presence of the rotational temperature gradient in the calculation of the rotational heat flux. However, extensive parametric studies concerning the coefficient in Eq. 6.1 and the threshold value appropriate for

these additional thermal nonequilibrium parameters were not published. It was also commonplace to manually enlarge the particle region surrounding the boundary layer of a transitional, hypersonic, blunt-body flow to achieve better agreement between surface properties predicted by the MPC method and those of full DSMC simulations.

Because of the ambiguity associated with this original $Kn_{ROT-NEQ}$ parameter, and in order to improve the *automatic* detection of both translational and thermal nonequilibrium effects in the MPC method, a new rotational nonequilibrium parameter is proposed in this chapter. This new parameter is evaluated in the context of transitional, hypersonic, blunt-body flows involving both a simple gas and a mixture of chemical species. Finally, the accuracy of the MPC method when employing this new parameter relative to a full DSMC simulation is determined, and compared to the accuracy achieved by the MPC method with the original $Kn_{ROT-NEQ}$ parameter.

6.1 A New Rotational Nonequilibrium Detection Parameter

Although the gradient-length local Knudsen number is empirical and, therefore, not guaranteed to be capable of predicting translational nonequilibrium in all cases, one of its benefits is that it is physically intuitive. When the gradient-length local Knudsen number has a small value, it is known that a continuum approach such as CFD is a physically accurate simulation technique. However, when the the gradient-length local Knudsen number has a large value, the results from a continuum approach become less accurate and a kinetic theory-based approach must be used. It is desirable for a thermal nonequilibrium detection parameter to invoke the same physical intuition as the gradient-length local Knudsen number.

As described in Chapter IV, the product of the rotational collision number, Z_{rot}, and the mean collision time, τ_c, is the characteristic relaxation time of the rotational energy mode, τ_{rot}. If rotational nonequilibrium effects were ignored altogether, then τ_{rot} would be equivalent to τ_c because *every* collision would allow for the translational

and rotational energies to be redistributed according to the degrees of freedom associated with each mode. However, in reality, only one out of every Z_{rot} collisions results in translational-rotational energy exchange, and rotational nonequilibrium is a direct consequence of this collision inefficiency. It is reasonable, therefore, that any reliable means of detecting rotational nonequilibrium effects should include these characteristic quantities. The new parameter that is proposed and evaluated in this chapter is

$$Kn_{rot} = \lambda_{rot} \left| \frac{\nabla T_{rot}}{T_{rot}} \right| = (\tau_{rot}) \sqrt{\frac{8RT_{trans}}{\pi}} \left| \frac{\nabla T_{rot}}{T_{rot}} \right| = (Z_{rot})\, \lambda \left| \frac{\nabla T_{rot}}{T_{rot}} \right|, \tag{6.2}$$

which is the same as the gradient-length local Knudsen number evaluated as a function of T_{rot}, except for the presence of the rotational collision number. This is not the same as simply using a different threshold value for $Kn_{GLL}\left(T_{rot}\right)$ because the rotational collision number is a function of the translational temperature. The product of Z_{rot} and λ has the physical significance of being the average distance a simulator particle travels prior to undergoing a rotationally inelastic collision. Therefore, a *rotational* mean free path is being used to represent the microscopic length scale of interest in this new parameter.

In the interest of thoroughness, the efficacy of the current continuum breakdown parameters should also be evaluated periodically as the capabilities of the MPC hybrid method continue to be developed. As such, this new parameter is evaluated alongside those currently used to detect continuum breakdown. The results of this analysis, as applied to simulations of both a simple gas and a mixture of chemical species, are presented in the next section. Because the original $Kn_{ROT-NEQ}$ rotational energy nonequilibrium parameter was originally employed to extend the post-shock hybrid interface further downstream, the bow shock region is the focus of the following analysis. However, it will also be shown that the newly proposed parameter given

in Eq. 6.2 is also capable of automatically determining an appropriate location for the hybrid interface that demarcates the boundary layer in a transitional, hypersonic, blunt-body flow.

6.2 Initial Placement of Hybrid Interfaces

As was done in Ref. [14], where the gradient-length local Knudsen number was first proposed for detecting failure of the continuum assumptions of the Navier-Stokes equations, the errors between full CFD and full DSMC simulations are calculated and compared to current measures of continuum breakdown employed in the MPC method and the newly proposed Kn_{rot} parameter. This is done not only to determine an appropriate threshold value for this new rotational nonequilibrium parameter, but also to re-evaluate the efficacy of the gradient-length local Knudsen number in consideration of recent extensions to the MPC hybrid method.

6.2.1 Simple Gas Study

The first case used to investigate the prediction of rotational nonequilibrium effects using the new parameter given in Eq. 6.2 is that of a Mach 12, Kn_∞ 0.01 flow of N_2 over a two-dimensional cylinder. This is the same case simulated in Chapter V. For simplicity of evaluation, the specific cases studied in this chapter ignore excitation of the vibrational energy mode. In order to determine whether or not a given continuum breakdown parameter is effective, the regions of the flow field in which the continuum and molecular descriptions differ must first be identified. Because previously noted failures of the gradient-length local Knudsen number have occurred in the fore body, full CFD and full DSMC simulation results are compared along the stagnation streamline and two additional extraction lines, as illustrated in Fig. 6.1.

The error, ϵ, between full CFD and full DSMC simulation results is defined as

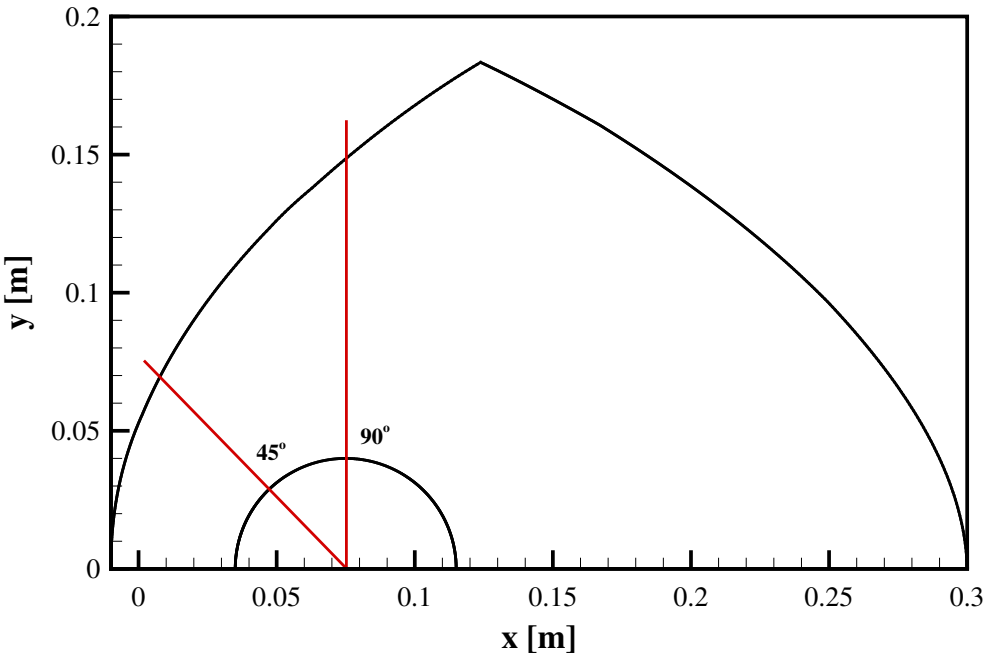

Figure 6.1: Computational domain and data extraction lines.

$$\epsilon = \frac{Q_{CFD}}{Q_{DSMC}} - 1, \tag{6.3}$$

where Q is any macroscopic property of interest. The errors in translational temperature, rotational temperature, velocity magnitude, and mass density along the stagnation streamline are plotted against the distance from the cylinder surface, normalized by the cylinder radius, in Fig. 6.2. Two dashed black lines are also plotted to indicate the upper and lower error bounds of $\pm 5\%$. Note that even though this level of accuracy was found to be too strict in Chapter V due to the statistical error associated with the DSMC method, because this was the accuracy goal used during the original assessment of the gradient-length local Knudsen number, it will continue to be used here.

According to Fig. 6.2, the hybrid interfaces should intersect the stagnation streamline such that DSMC is used between 0.319 and 0.646 radii from the cylinder surface to accurately simulate the strong nonequilibrium effects in the shock wave. There should also be a particle region enclosing the surface of the cylinder in order to ac-

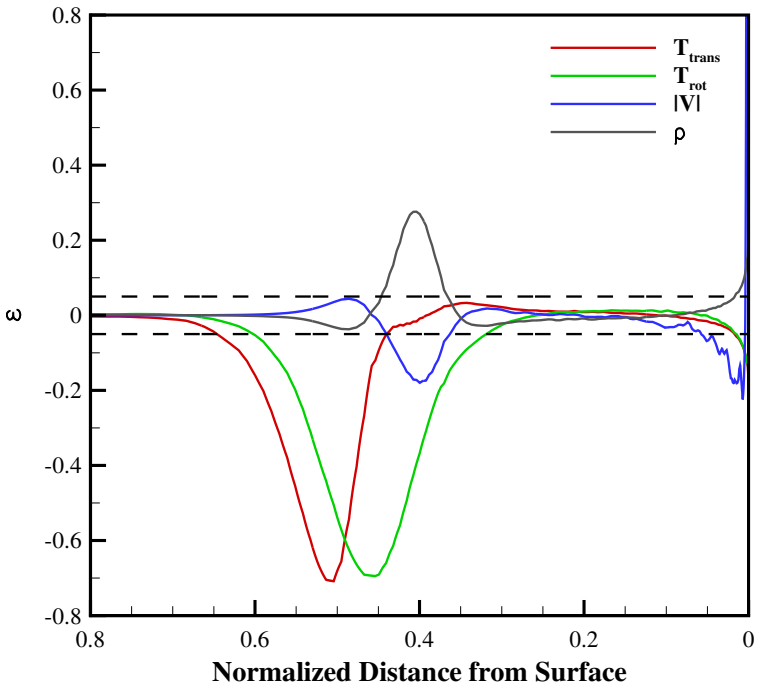

Figure 6.2: Errors between full CFD and full DSMC results along the stagnation streamline for the Mach 12, Kn_∞ 0.01 flow of N_2 over a two-dimensional cylinder.

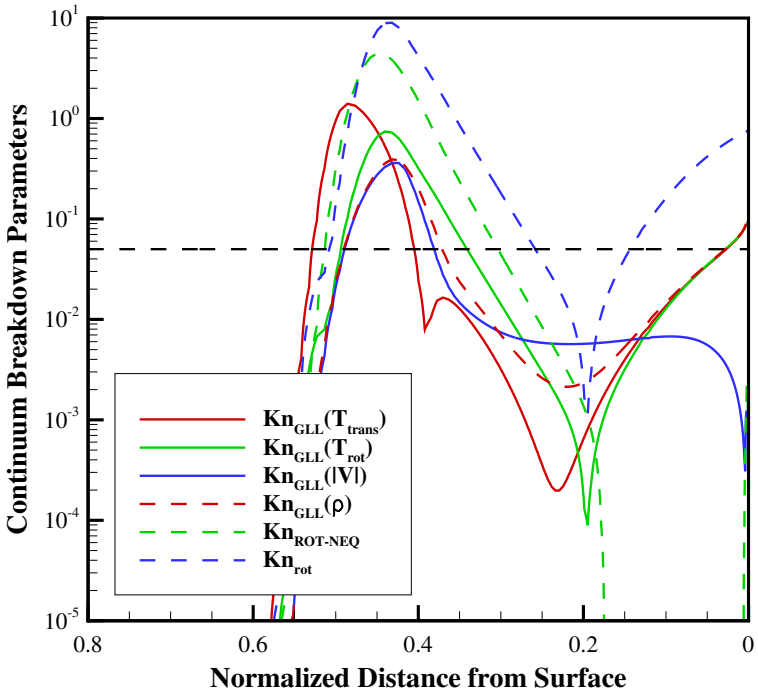

Figure 6.3: Continuum breakdown parameters based on a full CFD solution along the stagnation streamline for the Mach 12, Kn_∞ 0.01 flow of N_2 over a two-dimensional cylinder.

curately simulate the boundary layer, which extends to 0.057 radii from the cylinder surface. The values of the various continuum breakdown parameters currently employed in the MPC hybrid method, and the new Kn_{rot} parameter, are plotted along the stagnation streamline in Fig. 6.3. These continuum breakdown parameters are calculated from the full CFD solution of this flow field. Therefore, in an MPC hybrid simulation, these results would be used for initial placement of the hybrid interfaces.

Due to the underestimation of the shock thickness by the Navier-Stokes equations, the location upstream of the shock wave where the differences between CFD and DSMC first exceed $\pm 5\%$ is not accurately predicted by the continuum breakdown parameters shown in Fig. 6.3. In this test case, the value of the gradient-length local Knudsen number based on translational temperature exceeds the threshold value of 0.05 at a normalized distance of 0.529 from the cylinder surface. This would place the pre-shock hybrid interface much further downstream than required for accurate and consistent exchange of information between the particle and continuum domains. The inability of the gradient-length local Knudsen number to accurately predict the onset of continuum breakdown at the shock front has been noted by Wang and Boyd [88], and if the initial hybrid interfaces were not adjusted as the hybrid solution evolved, this would lead to inaccurate results. However, because these continuum breakdown parameters are re-calculated periodically throughout the simulation, and the hybrid interfaces are moved accordingly, this has not posed a problem for past simulations. As will be shown later in this chapter, the pre-shock hybrid interface will be automatically repositioned to a near-equilibrium region as the simulation evolves, obviating any concerns about the initial placement of this hybrid interface. Thus, the location of the pre-shock hybrid interface as predicted by the initial CFD solution will not be discussed further.

Whereas the pre-shock hybrid interface moves upstream substantially during the course of a hybrid simulation, the post-shock and boundary layer hybrid interfaces

experience minimal change. Therefore, their initial placement relative to regions in which full CFD and full DSMC simulation results disagree gives greater insight to the effectiveness of these continuum breakdown parameters. According to Fig. 6.2, the post-shock hybrid interface should be placed at a maximum of 0.319 radii from the cylinder surface in order to envelope the shock wave in a particle region. Fig. 6.3 illustrates that without some indicator of rotational nonequilibrium effects, the post-shock hybrid interface would be located at a normalized distance of 0.341, where significant errors between CFD and DSMC are present. Thus, an additional parameter is required. The value of the $Kn_{ROT-NEQ}$ parameter decreases below 0.05 at a normalized distance of 0.304, placing the post-shock hybrid interface in an appropriate position slightly downstream of the shock.

Because of the isothermal boundary condition enforced at the cylinder surface in the CFD simulation, the value of the $Kn_{ROT-NEQ}$ parameter in the boundary layer is much smaller than the threshold value of 0.05. The gradient-length local Knudsen number also fails to position the boundary layer hybrid interface upstream of the location where CFD and DSMC begin to deviate by more than $\pm 5\%$. Whereas the error in the velocity magnitude exceeds the lower error bound at a normalized distance of 0.057, the gradient-length local Knudsen number based on the rotational temperature exceeds the threshold value of 0.05 at a normalized distance of 0.028—much too close to the cylinder surface.

Focusing now on the value of Kn_{rot} along the stagnation streamline, even though an appropriate threshold value has yet to be determined, it can be seen from Fig. 6.3 that this new parameter offers an advantage over the original $Kn_{ROT-NEQ}$ parameter near the surface of the cylinder. An optimal choice for the threshold value for this new parameter would maintain a similar position for the post-shock hybrid interface while increasing the size of the boundary layer particle region relative to the other continuum breakdown parameters. When the value of $Kn_{ROT-NEQ}$ decreases below

0.05 downstream of the shock wave, the Kn_{rot} parameter has a value of approximately 0.2. Near the cylinder surface, Kn_{rot} takes this value at a normalized distance of 0.090, which would enlarge the particle region surrounding the boundary layer such that the hybrid interface is placed in a near-equilibrium region of the flow field, based on the level of agreement exhibited in Fig. 6.2. Therefore, comparison of the full CFD and full DSMC results along the stagnation streamline, along with the values of the various continuum breakdown parameters, shows that the new Kn_{rot} parameter with a threshold value of 0.2 may be an effective alternative to $Kn_{ROT-NEQ}$.

The errors between full CFD and full DSMC along the 45° extraction line are plotted in Fig. 6.4. Again, the strong nonequilibrium effects in the shock wave and the boundary layer are apparent in this plot. A notable difference between Fig. 6.4 and Fig. 6.2 is the profile of velocity magnitude error near the cylinder surface. The no-slip boundary condition is enforced along the entire cylinder surface in the CFD simulation, whereas DSMC inherently allows for velocity slip. At the stagnation point, the velocity magnitude must go to zero in both simulations, so that the scatter associated with the DSMC solution can be of the same order as the velocity itself. This leads to large oscillations in Fig. 6.2 near the cylinder surface. The velocity tangent to the cylinder surface at the point where it intersects the 45° extraction line is nonzero according to the full DSMC results, leading to no oscillations in the velocity magnitude error near the cylinder surface in Fig. 6.4.

According to the errors plotted in Fig. 6.4, the rotational temperature predicted by CFD is the last macroscopic property to come into agreement with DSMC downstream of the shock wave. This occurs at a normalized distance of 0.472 from the cylinder surface. The inability of CFD to accurately simulate the nonequilibrium effects in the boundary layer is confirmed by errors in all macroscopic properties of interest exceeding ±5% at nearly the same distance from the cylinder surface. The error in translational temperature exceeds the lower error bound at a normalized distance of

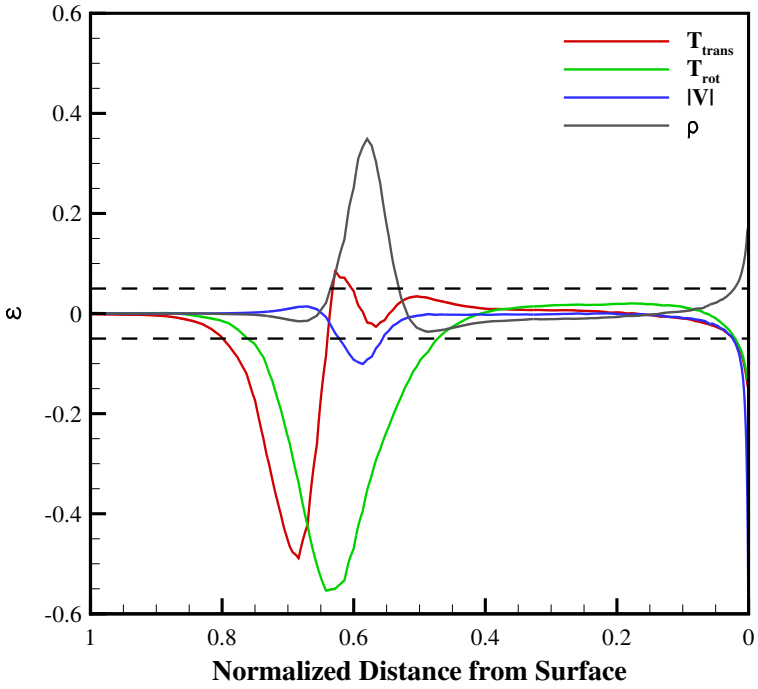

Figure 6.4: Errors between full CFD and full DSMC results along the 45° extraction line for the Mach 12, Kn_∞ 0.01 flow of N_2 over a two-dimensional cylinder.

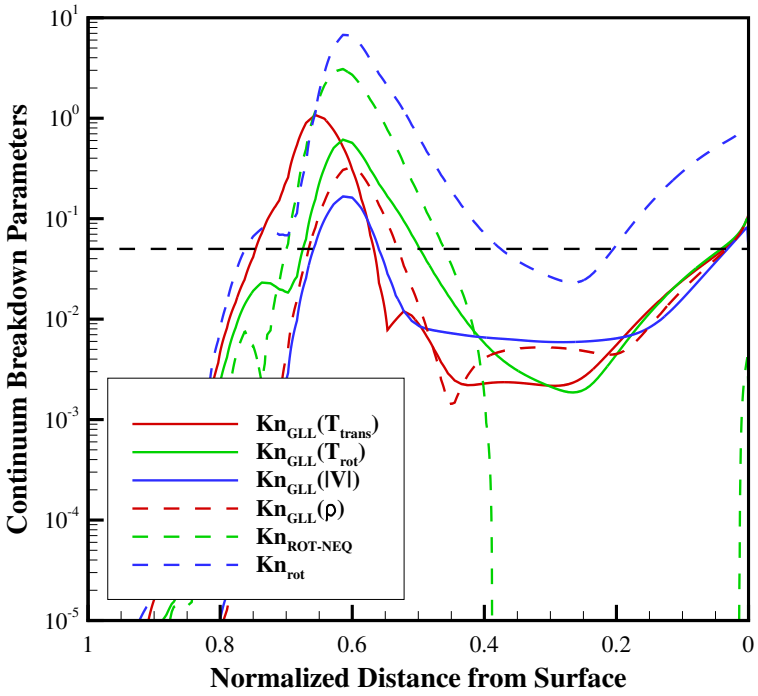

Figure 6.5: Continuum breakdown parameters based on a full CFD solution along the 45° extraction line for the Mach 12, Kn_∞ 0.01 flow of N_2 over a two-dimensional cylinder.

0.024. As was the case along the stagnation streamline, the original $Kn_{ROT-NEQ}$ parameter accurately predicts the location of the post-shock hybrid interface at a distance of 0.461 radii from the cylinder surface, but fails to predict the need for a particle region in the boundary layer. This is illustrated in Fig. 6.5. However, the value of $Kn_{GLL}(T_{rot})$ exceeds the threshold value of 0.05 at a normalized distance of 0.042 from the cylinder surface, which does provide a conservative estimate of the thickness of the boundary layer region. Therefore, according to these results alone, the combination of the gradient-length local Knudsen number and $Kn_{ROT-NEQ}$ is sufficient for accurately positioning hybrid interfaces in near-equilibrium regions of the flow field along the 45° extraction line. Use of the new Kn_{rot} parameter (with a threshold value of 0.2) in place of $Kn_{ROT-NEQ}$ would only serve to provide a more conservative estimate of rotational nonequilibrium, as the post-shock and boundary layer hybrid interfaces would be placed at normalized distances of 0.452 and 0.127, respectively.

Figure 6.6 shows the errors between full CFD and full DSMC simulation results along the 90° extraction line. As was the case with the other extraction lines, the rotational temperature predicted by CFD is the last macroscopic property to come into agreement with DSMC in the post-shock region at a normalized distance of 1.29 from the cylinder surface. Strong nonequilibrium effects in the boundary layer are first indicated by the error in velocity magnitude, which exceeds the lower error bound approximately 0.102 radii from the cylinder surface. The $Kn_{ROT-NEQ}$ parameter and the gradient-length local Knudsen number are able to accurately predict the initial placement of the post-shock and boundary layer hybrid interfaces at normalized distances of 1.28 and 0.127, respectively. Again, the new Kn_{rot} parameter provides a more conservative measure of rotational nonequilibrium, predicting that the post-shock hybrid interface be located at a normalized distance of 1.27 from the cylinder and the boundary layer hybrid interface be placed approximately 0.326 cylinder radii

from the surface.

Based on these simple gas simulation results, the benefit of using the Kn_{rot} rotational nonequilibrium parameter instead of the $Kn_{ROT-NEQ}$ is most evident along the stagnation streamline. In order to present a more complete evaluation of this new parameter, and because one of the main objectives of the current work is to extend the MPC method's capabilities to include mixtures of chemical species, a gas comprised of 50% N_2/50% N (by mole) is examined in the next section.

6.2.2 Gas Mixture Study

The second flow field of interest in this evaluation of the new Kn_{rot} rotational nonequilibrium parameter is that of a Mach 10, Kn_∞ 0.01 flow of a 50% N_2/50% N (by mole) gas mixture over a two-dimensional cylinder. The mixture mean free path is calculated as

$$\lambda = \sum_{i=1}^{s} \frac{n_i}{n} \left\{ \sum_{j=1}^{s} \left[\pi d_{ref,ij}^2 n_j \left(\frac{T_{ref}}{T_{trans}} \right)^{\omega_{ij}-1/2} \left(1 + \frac{m_i}{m_j} \right)^{1/2} \right] \right\}^{-1}, \qquad (6.4)$$

in accordance with the VHS collision model. With a freestream temperature of $217.45K$, and the reference collision diameters given in Appendix A, this results in freestream densities of $4.522 \times 10^{-5} kg/m^3$ and $2.261 \times 10^{-5} kg/m^3$ for N_2 and N, respectively. The freestream velocity is $3{,}594 m/s$, and the cylinder surface employs an isothermal boundary condition where the temperature is maintained at $1{,}000K$. It should be noted that calculation of the new Kn_{rot} rotational nonequilibrium parameter for gas mixtures employs the mixture average rotational relaxation time as calculated using Eq. 4.40, and the specific gas constant, R, calculated for the mixture.

The full CFD solution is verified to be grid-independent on a computational mesh comprised of approximately 41,100 cells. This same mesh is used to obtain the full DSMC solution after being refined to comply with DSMC cell size requirements using the automatic refinement algorithm outlined in Chapter III. A constant time step of

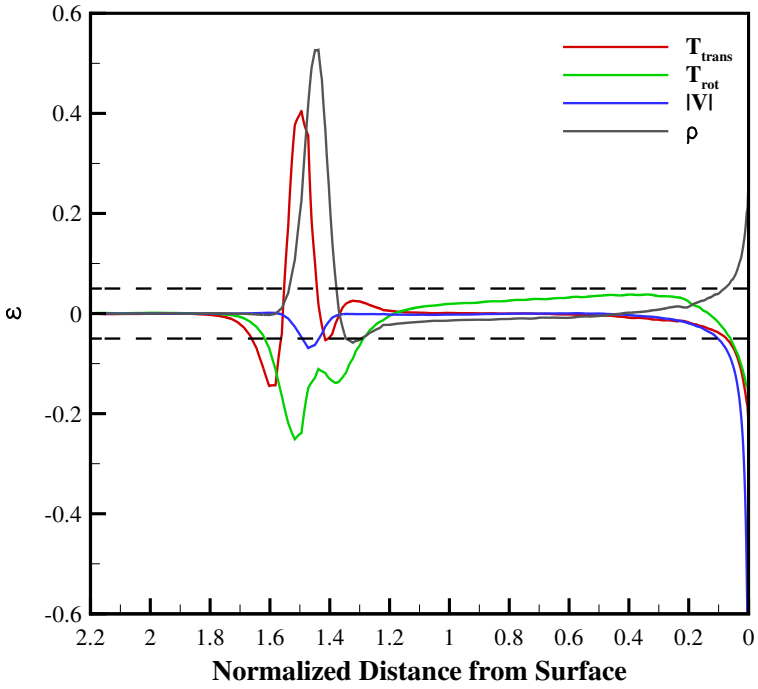

Figure 6.6: Errors between full CFD and full DSMC results along the 90° extraction line for the Mach 12, Kn_∞ 0.01 flow of N_2 over a two-dimensional cylinder.

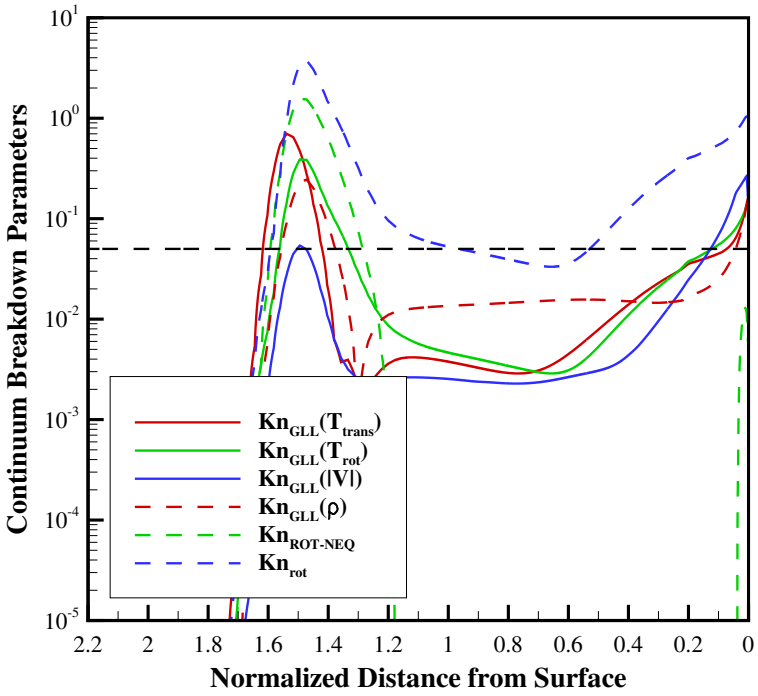

Figure 6.7: Continuum breakdown parameters based on a full CFD solution along the 90° extraction line for the Mach 12, Kn_∞ 0.01 flow of N_2 over a two-dimensional cylinder.

$1 \times 10^{-8} s$ is used in the full DSMC simulation; this time step is verified to be less than the local mean collision time throughout the flow domain. The maximum time step employed in the full CFD simulation is $1 \times 10^{-7} s$. In order to maintain a minimum of 40 particles per cell (approximately 20 particles of each species per cell), a constant numerical weight of 2×10^{12} is specified everywhere except near the cylinder surface, where reduced cell-based numerical weights are used. Vibrational excitation is again ignored in these simulations so that the merit of each of the rotational nonequilibrium parameters can be clearly determined. The CFD and DSMC simulations compared here employ consistent physical models, which have been detailed in Chapter IV.

Following the same procedure as described in the previous section, the errors between the full CFD and full DSMC simulation results for this flow field, along with the initial predictions of continuum breakdown based on the full CFD solution, are calculated along the stagnation streamline and two additional extraction lines. Figure 6.8 shows the errors in various macroscopic properties along the stagnation streamline. Again, the initial placement of the pre-shock hybrid interface is not discussed.

According to Fig. 6.8, the post-shock hybrid interface should be located no more than 0.377 radii from the cylinder surface, as this is the approximate location where the rotational temperature predicted by CFD comes back into agreement with that predicted by DSMC. The error in velocity magnitude indicates that the boundary layer hybrid interface should be located at least 0.077 cylinder radii from the surface. Looking now at Fig. 6.9, where the various continuum breakdown parameters are plotted along the stagnation streamline, the value of $Kn_{ROT-NEQ}$ crosses the threshold indicated by the dashed black line at a normalized distance of 0.372. The new Kn_{rot} parameter takes the value of 0.2 at a normalized distance of 0.375, so either one of these rotational nonequilibrium parameters could be used to predict the location of the post-shock hybrid interface. Note that if the gradient-length local Knudsen num-

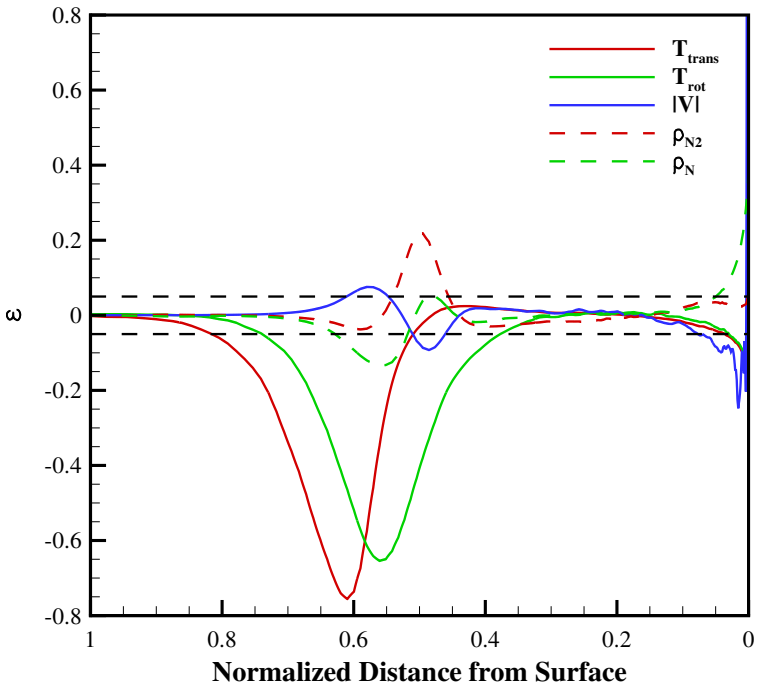

Figure 6.8: Errors between full CFD and full DSMC results along the stagnation streamline for the Mach 10, Kn_∞ 0.01 flow of 50% N_2/50% N over a two-dimensional cylinder.

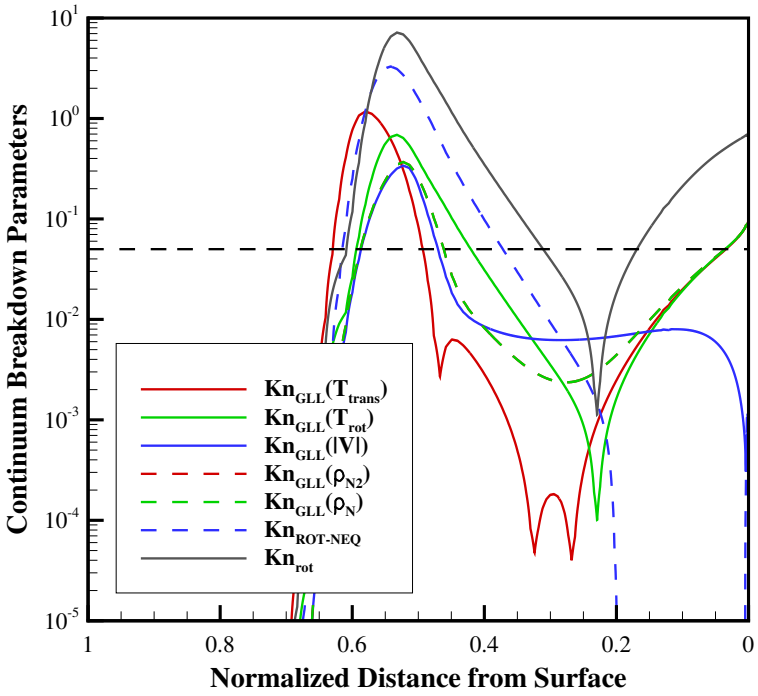

Figure 6.9: Continuum breakdown parameters based on a full CFD solution along the stagnation streamline for the Mach 10, Kn_∞ 0.01 flow of 50% N_2/50% N over a two-dimensional cylinder.

ber is the only continuum breakdown parameter considered, the post-shock hybrid interface would be located within the shock wave at a normalized distance of 0.421.

Neither the gradient-length local Knudsen number nor the $Kn_{ROT-NEQ}$ parameter are capable of accurately predicting the thickness of the boundary layer along the stagnation streamline. The first indication of strong nonequilibrium effects near the surface is when the value of $Kn_{GLL}\left(T_{rot}\right)$ exceeds 0.05 at a normalized distance of 0.035 from the cylinder surface. The Kn_{rot} parameter takes on a value of 0.2 at a normalized distance of 0.103, which is a conservative estimate of where the hybrid interface should be placed so that DSMC can be used in the boundary layer rather than CFD.

Similar conclusions can be drawn by analyzing the full CFD and full DSMC results along the 45° extraction line. The errors between these two solutions and the values of the continuum breakdown parameters are shown in Fig. 6.10 and Fig. 6.11, respectively. Again, the Kn_{rot} parameter with a threshold value of 0.2 predicts that the boundary layer hybrid interface be placed at a normalized distance of 0.142 from the cylinder surface, which is conservative considering the errors in macroscopic properties do not exceed $\pm 5\%$ until a normalized distance of 0.071. The gradient-length local Knudsen number provides a more accurate estimate of continuum breakdown than $Kn_{ROT-NEQ}$, but still under predicts the thickness of the boundary layer along the 45° extraction line. The new Kn_{rot} parameter is also more accurate at predicting the location of the post-shock hybrid interface at a normalized distance of 0.552, as compared to the $Kn_{ROT-NEQ}$ parameter, which places the interface at a normalized distance of 0.556. As can be seen in Fig. 6.10, the error in rotational temperature falls within the target accuracy range downstream of the shock at a normalized distance of 0.554 from the cylinder surface.

Lastly, the errors between the full CFD and full DSMC results along a 90° extraction line are plotted in Fig. 6.12. According to these results, the post- shock hybrid

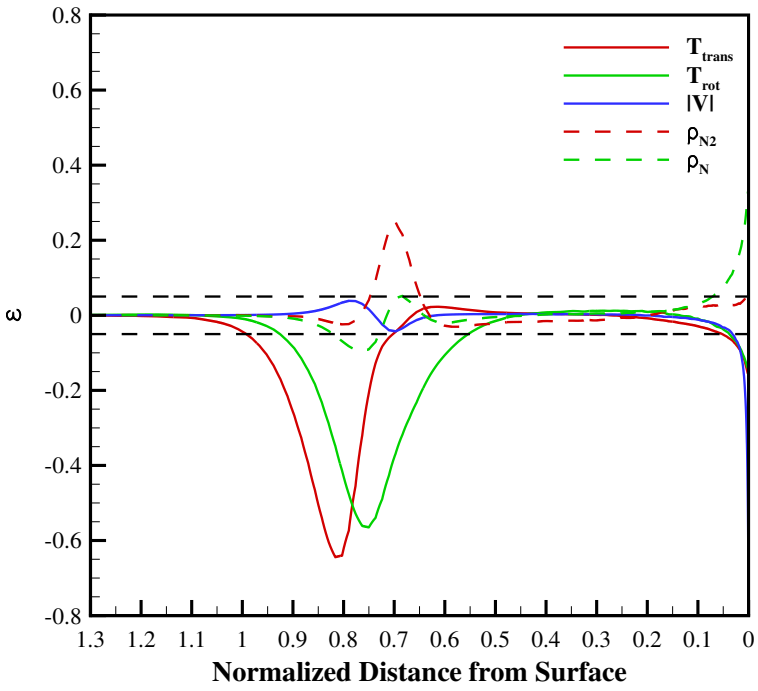

Figure 6.10: Errors between full CFD and full DSMC results along the 45° extraction line for the Mach 10, Kn_∞ 0.01 flow of 50% N_2/50% N over a two-dimensional cylinder.

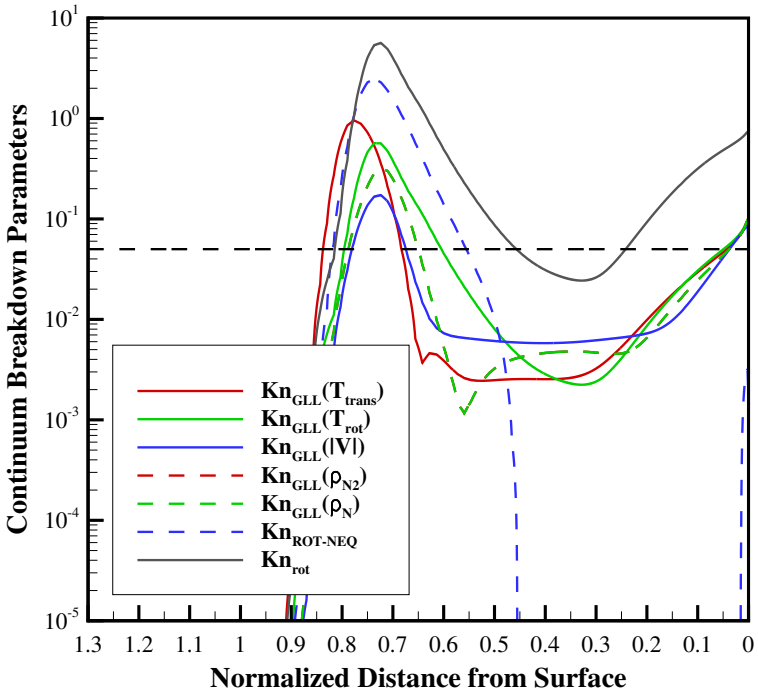

Figure 6.11: Continuum breakdown parameters based on a full CFD solution along the 45° extraction line for the Mach 10, Kn_∞ 0.01 flow of 50% N_2/50% N over a two-dimensional cylinder.

interface should be located at a maximum of 1.496 radii from the cylinder surface. Additionally, the boundary layer hybrid interface should be located at least 0.188 radii from the cylinder surface. Upon comparing these error profiles to the continuum breakdown parameters plotted in Fig. 6.13, it is evident that none of the continuum breakdown parameters that have been used in the past accurately predict the correct placement of either the post-shock or the boundary layer hybrid interfaces. The value of $Kn_{ROT-NEQ}$ decreases below the threshold value of 0.05 at a normalized distance of 1.512, where the errors between CFD and DSMC still exceed the target error range of $\pm 5\%$. The Kn_{rot} parameter decreases below a value of 0.2 at a normalized distance of 1.506. Although this is more conservative than $Kn_{ROT-NEQ}$, this position is still in a region of nonequilibrium, as dictated by the initial CFD solution. However, use of the Kn_{rot} parameter and a threshold value of 0.2 does provide a reasonable measure of nonequilibrium in the boundary layer. According to this parameter, the hybrid interface should be placed at a distance of 0.344 radii from the cylinder surface, which is upstream of the location where errors in macroscopic properties exceed $\pm 5\%$. The gradient-length local Knudsen number places this hybrid interface too close to the cylinder surface at a normalized distance of 0.142.

6.2.3 Conclusions from Simple Gas and Gas Mixture Studies

As just exhibited, a great deal of information can be derived by performing careful comparisons of the errors between CFD and DSMC results, and the values of various continuum breakdown parameters, throughout a given flow field of interest. This is precisely the methodology followed by Boyd, *et al.* [14] when the gradient-length local Knudsen number was originally proposed and investigated, and is an integral component of verifying any hybrid DSMC/CFD approach. Although this evaluation of the new Kn_{rot} rotational nonequilibrium parameter is by no means exhaustive, it does provide insight into its effectiveness and advantages over the original $Kn_{ROT-NEQ}$

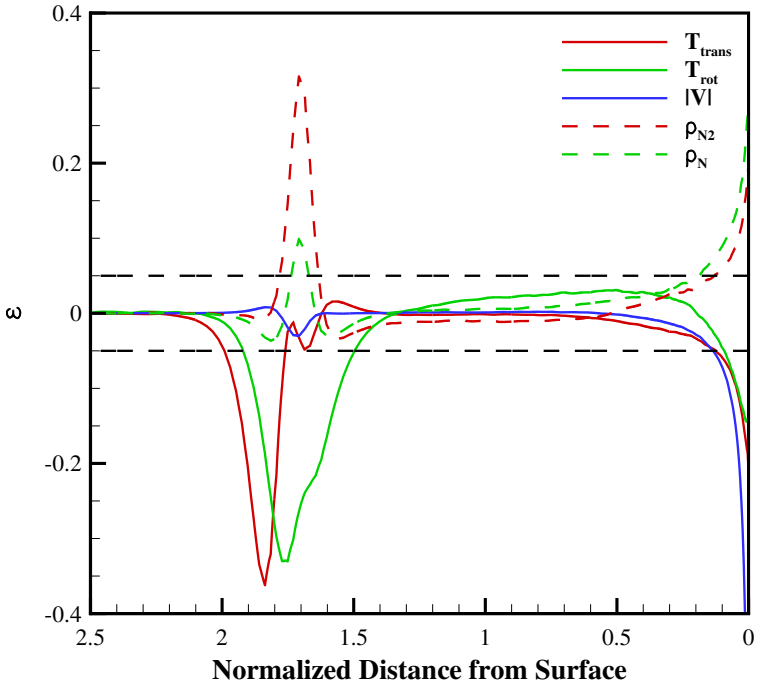

Figure 6.12: Errors between full CFD and full DSMC results along the 90° extraction line for the Mach 10, Kn_∞ 0.01 flow of 50% N_2/50% N over a two-dimensional cylinder.

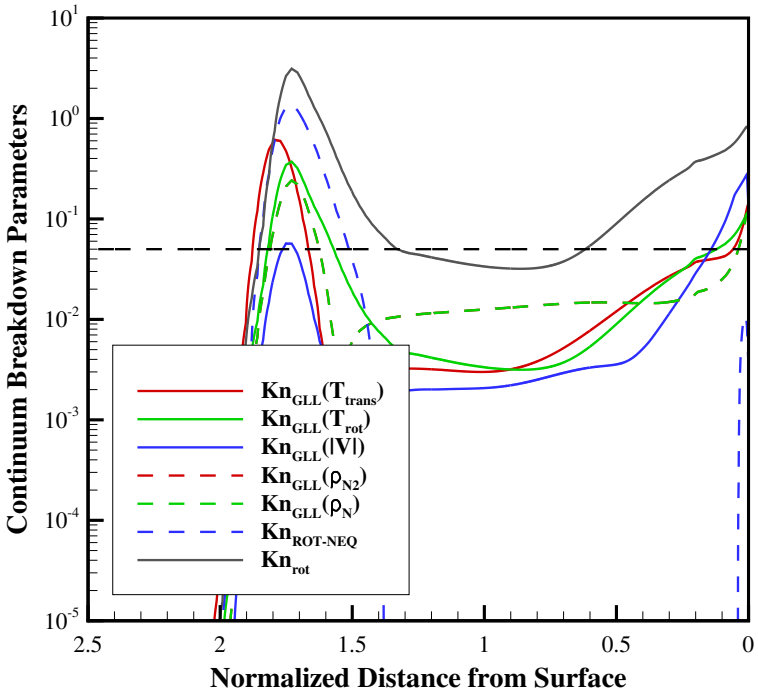

Figure 6.13: Continuum breakdown parameters based on a full CFD solution along the 90° extraction line for the Mach 10, Kn_∞ 0.01 flow of 50% N_2/50% N over a two-dimensional cylinder.

parameter and gradient-length local Knudsen number. For example, in neither the simple gas study nor the gas mixture study was the gradient-length local Knudsen number able to accurately predict the thickness of the boundary layer over the entire fore body. This is an important finding of this study, as the gradient-length local Knudsen number has been the cornerstone of continuum breakdown prediction in the MPC hybrid method since its inception. Manually increasing the thickness of the particle domain that envelopes the boundary layer proved useful in past simulations using the MPC method, but in the interest of furthering both the generality and the applicability of the MPC hybrid method, such shortcomings must be identified and corrected.

The original $Kn_{ROT-NEQ}$ parameter is fairly effective at predicting the correct location of the post-shock hybrid interface, for which it was intended, without being overly conservative. This is more true for the simple gas study than it is for the gas mixture study, where the failures have been highlighted in the previous section. In many cases, Kn_{rot} takes on a value of 0.2 at the same approximate distance from the cylinder surface as $Kn_{ROT-NEQ}$ takes on a value of 0.05 to indicate where the post-shock hybrid interface should be located. It should also be noted that a larger threshold value for Kn_{rot} would still be appropriate for most of the fore body region in the simple gas case. However, for all but one of the six extraction lines examined here, a threshold value of 0.2 enables a conservative estimate for the initial placement of both the post-shock and boundary layer hybrid interfaces.

6.3 MPC Results

This new Kn_{rot} parameter, in conjunction with the gradient-length local Knudsen number, is employed to demarcate particle and continuum regions of an MPC hybrid simulation of the Mach 12, Kn_{∞} 0.01 simple gas case examined in Section 6.2.1. After hybrid results are obtained, they are not only compared to full CFD and full

DSMC simulation results, but also those from a hybrid solution obtained by using the original $Kn_{ROT-NEQ}$ parameter. Unlike the results presented in Chapter V, hybrid interface locations are determined solely by these continuum breakdown parameters, i.e. DSMC is not forced to be used within a certain distance of the cylinder surface.

Many of the same conclusions from the previous section can be drawn from the initial placement of the hybrid interfaces when using each rotational nonequilibrium parameter. These initial hybrid interfaces are plotted in the upper pane of Fig. 6.14, where the red interfaces are obtained with the original $Kn_{ROT-NEQ}$ parameter and the blue interfaces are obtained with the new Kn_{rot} parameter. It can be seen that the particle region enveloping the bow shock wave is comparable in size, whether employing the Kn_{rot} or the $Kn_{ROT-NEQ}$ parameter. The new parameter predicts the same initial post-shock hybrid interface location for which the original parameter was first proposed, and as the simulation progresses, adjusts the post-shock hybrid interface to a more conservative location slightly downstream of the final post-shock hybrid interface predicted by the $Kn_{ROT-NEQ}$ parameter. The final positions of the hybrid interfaces in this simulation are plotted in the lower pane of Fig. 6.14.

The difference between the pre-boundary layer hybrid interface locations is much more evident. The new Kn_{rot} parameter predicts a thicker nonequilibrium boundary layer region that neither the $Kn_{ROT-NEQ}$ parameter nor the gradient-length local Knudsen number is able to consistently predict. This expanded particle region in the fore body then smoothly transitions to a slightly larger near-wake region in which DSMC is also used. As alluded to in the previous section, the largest difference between the initial and final hybrid interfaces is the position of the pre-shock hybrid interface. Again, this is why the initial location of the pre-shock hybrid interface as calculated by the full CFD solution is not as concerning as that for the post-shock and boundary layer hybrid interfaces.

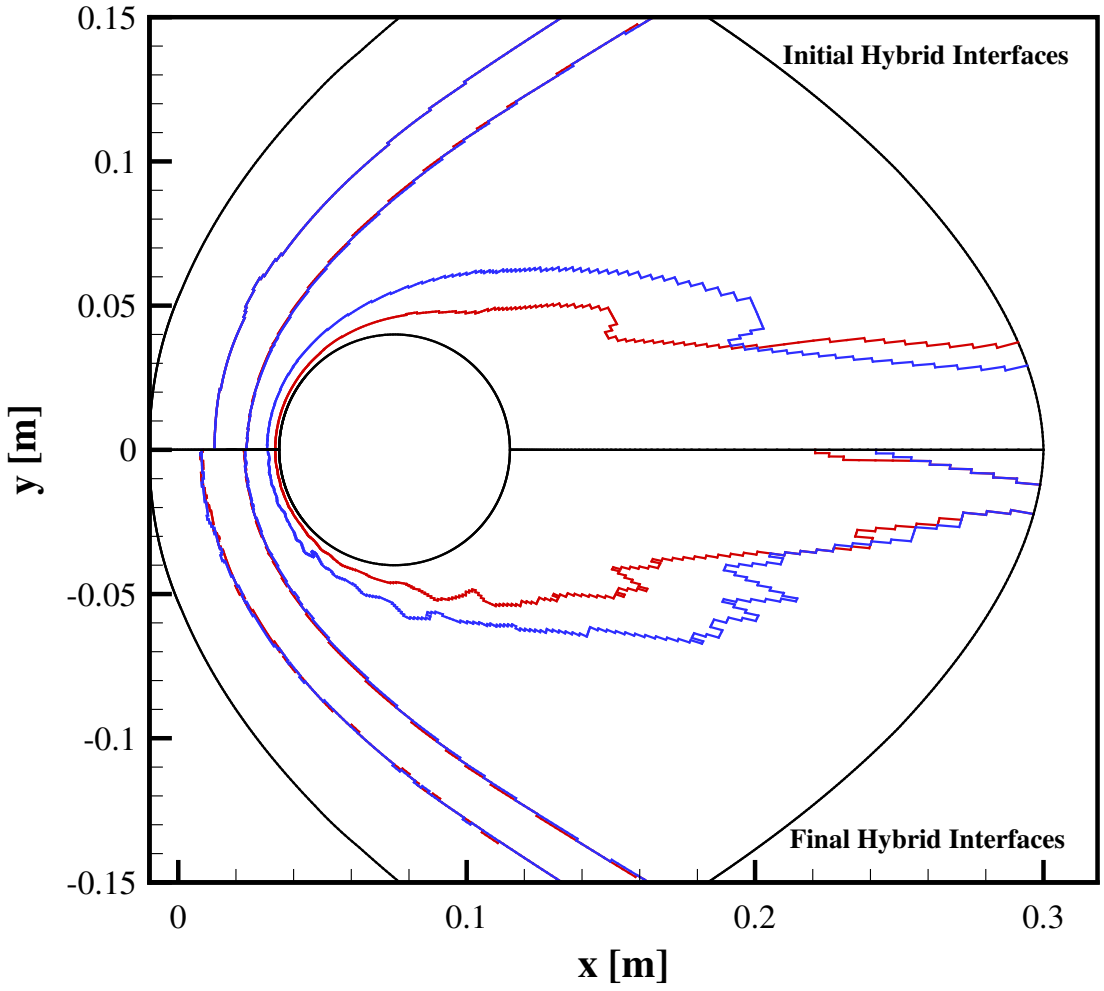

Figure 6.14: Initial (upper pane) and final (lower pane) hybrid interfaces, where Kn_{rot} interfaces are shown blue, and $Kn_{ROT-NEQ}$ interfaces are shown in red.

6.3.1 Flow Field Properties

Various flow field properties are first compared in order to evaluate the ability of the MPC method to reproduce results from a full DSMC simulation when the new Kn_{rot} parameter is employed to predict regions of strong rotational nonequilibrium effects. A comparison of the contours of translational temperature is plotted in Fig. 6.15, where DSMC results are shown as flooded contours, MPC hybrid results using the new Kn_{rot} parameter are shown as lines in the upper pane, and MPC hybrid results using the original $Kn_{ROT-NEQ}$ parameter are shown as lines in the lower pane. The differences between these two sets of MPC results are much more subtle than those between the MPC and full CFD results discussed in Chapter V, for example. However, because of the subsonic region in the fore body of the cylinder, incorrect placement of the pre-boundary layer hybrid interface has far-reaching effects upstream, which leads to disagreement between the translational temperature profiles within the diffuse shock wave. There are also differences between contours of translational temperature in the near-wake. The same observations can be made from the contours of rotational temperature plotted in Fig. 6.16.

Because the gradient-length local Knudsen number was initially supplemented by the $Kn_{ROT-NEQ}$ parameter in order to extend the post-shock hybrid interface downstream to a region of near-equilibrium, a closer examination of the translational and rotational temperatures along the stagnation streamline is warranted. First, translational and rotational temperatures given by DSMC, CFD, and the MPC hybrid method employing the $Kn_{ROT-NEQ}$ parameter are plotted in Fig. 6.17. The hybrid interfaces that demarcate particle and continuum regions in the MPC method are also shown as vertical black lines. The onset of the shock wave predicted by the MPC method is preceded by that predicted by full DSMC. Within the particle region enveloping the shock wave, the hybrid results for the translational and rotational temperatures lie between those given by the full CFD and full DSMC solutions. In

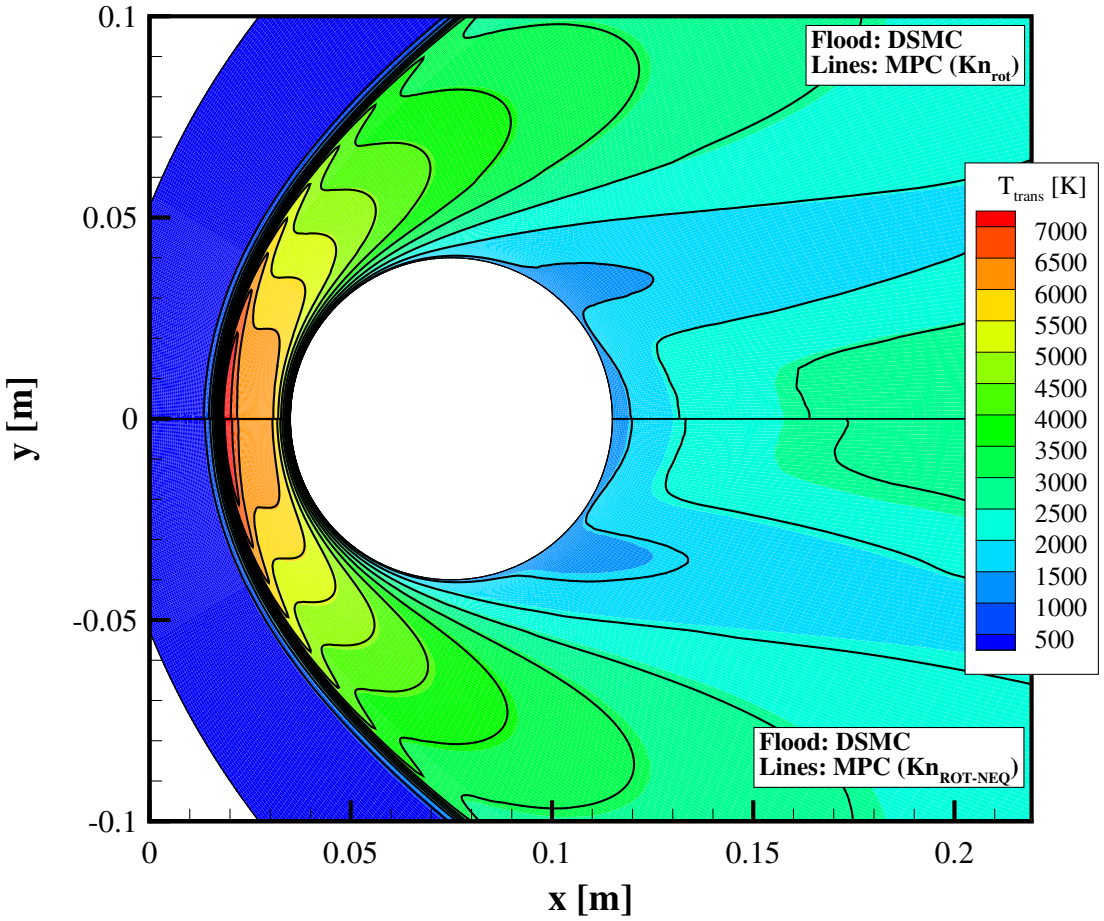

Figure 6.15: Contours of translational temperature, with DSMC results shown as flooded contours, MPC results where Kn_{rot} is used as lines in the upper pane, and MPC results where $Kn_{ROT-NEQ}$ is used as lines in the lower pane.

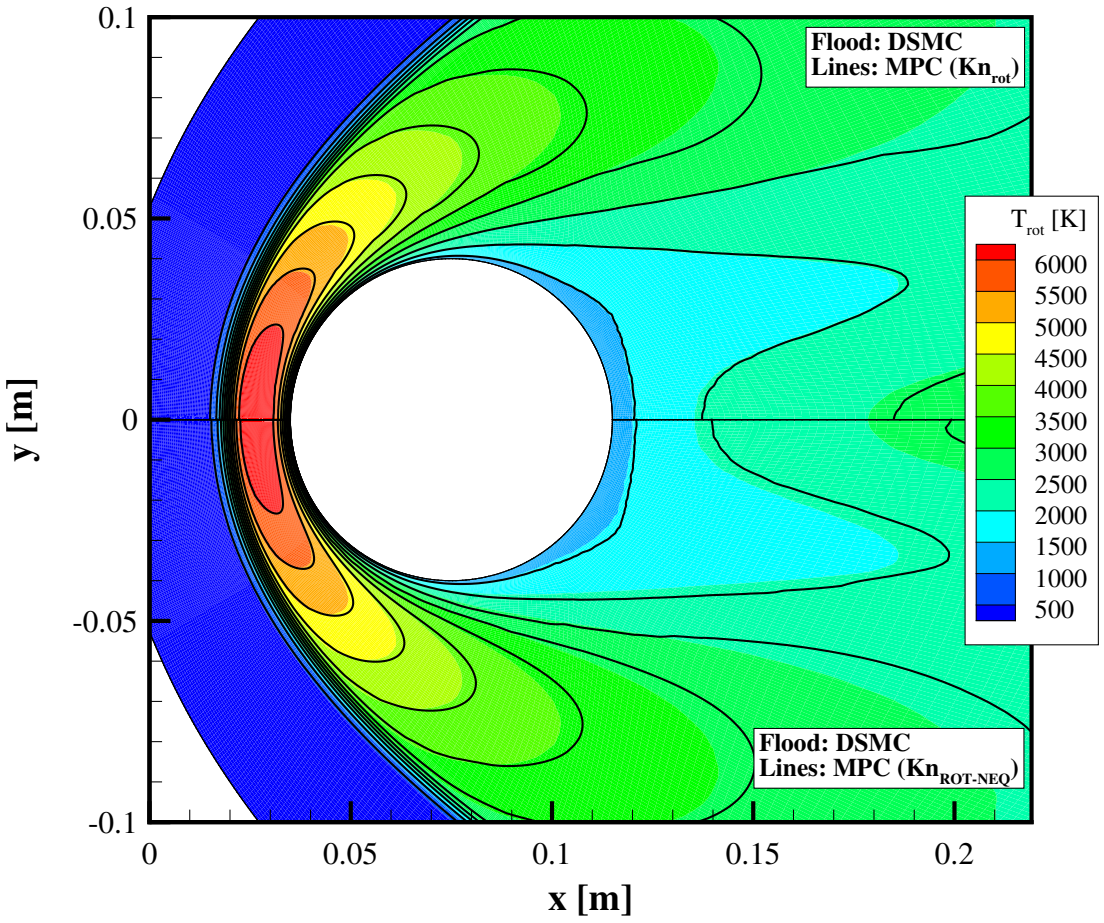

Figure 6.16: Contours of rotational temperature, with DSMC results shown as flooded contours, MPC results where Kn_{rot} is used as lines in the upper pane, and MPC results where $Kn_{ROT-NEQ}$ is used as lines in the lower pane.

contrast, translational and rotational temperature profiles obtained with the MPC hybrid method and the new Kn_{rot} parameter used in place of the $Kn_{ROT-NEQ}$ parameter are in much better agreement with full DSMC, as shown in Fig. 6.18.

Magnified views of the translational and rotational temperature profiles near the post-shock hybrid interface are shown in Figs. 6.19 and 6.20. The hybrid results plotted in Fig. 6.19 are obtained using the original $Kn_{ROT-NEQ}$ parameter. Although the MPC method is in reasonable agreement with full DSMC in terms of the translational temperature, there is a fairly large discrepancy between the rotational temperature profiles at this location. The hybrid results obtained using the new Kn_{rot} parameter are in much better agreement with full DSMC, as shown in Fig. 6.20.

Translational and rotational temperature profiles are also shown on a magnified scale in the region surrounding the pre-boundary layer hybrid interface in Figs. 6.21 and 6.22. It is observed that the full DSMC results are actually in better agreement with the full CFD results than with those given by the MPC method when the $Kn_{ROT-NEQ}$ parameter is used. Here, the MPC method under predicts the translational and rotational temperatures by approximately $200K$. Much closer agreement is achieved when the new Kn_{rot} parameter is used, as is evident in Fig. 6.22. Comparison of Figs. 6.21 and 6.22 also clearly illustrates that use of the new Kn_{rot} parameter in place of the original $Kn_{ROT-NEQ}$ parameter moves the pre-boundary layer hybrid interface upstream by $2.5mm$, whereas the other hybrid interfaces approximately retain their same locations.

A consistent and quantitative evaluation of the flow field results obtained using the MPC hybrid method is also performed in the same manner described in Chapter V. The errors incurred in translational temperature, rotational temperature, velocity magnitude, and mass density throughout the computational domain as a result of employing the MPC hybrid method and the new Kn_{rot} parameter are plotted in Figs. 6.23 through 6.26. The final hybrid interfaces are also plotted so that localized

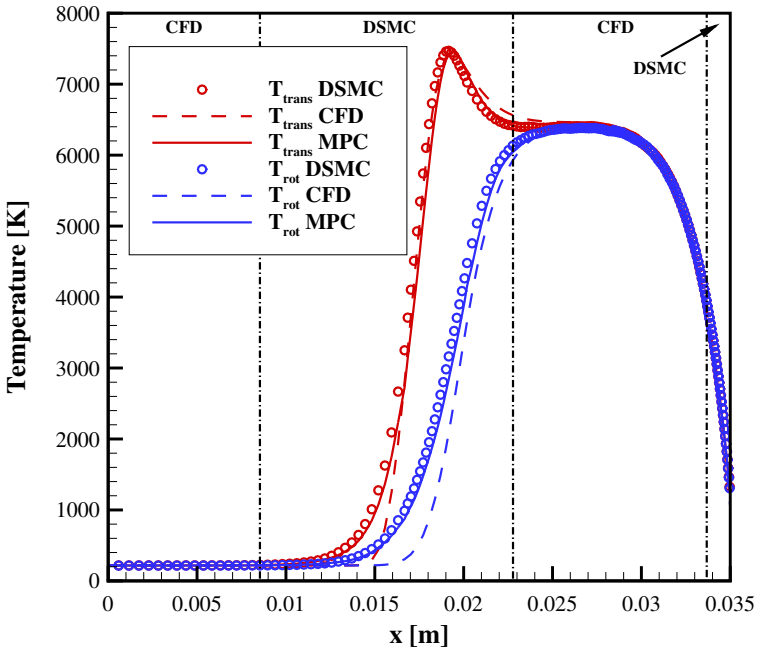

Figure 6.17: Translational and rotational temperatures along the stagnation streamline, with MPC results obtained using the original $Kn_{ROT-NEQ}$ parameter.

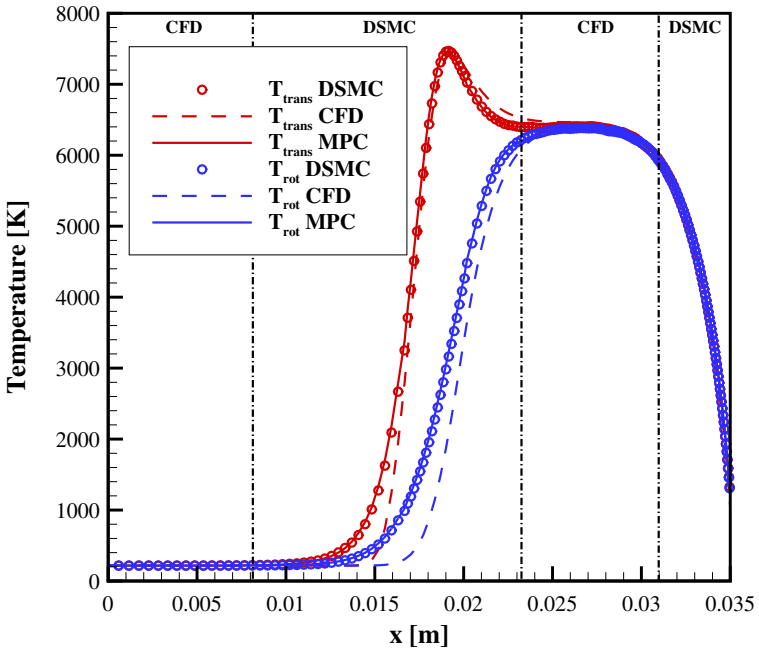

Figure 6.18: Translational and rotational temperatures along the stagnation streamline, with MPC results obtained using the new Kn_{rot} parameter.

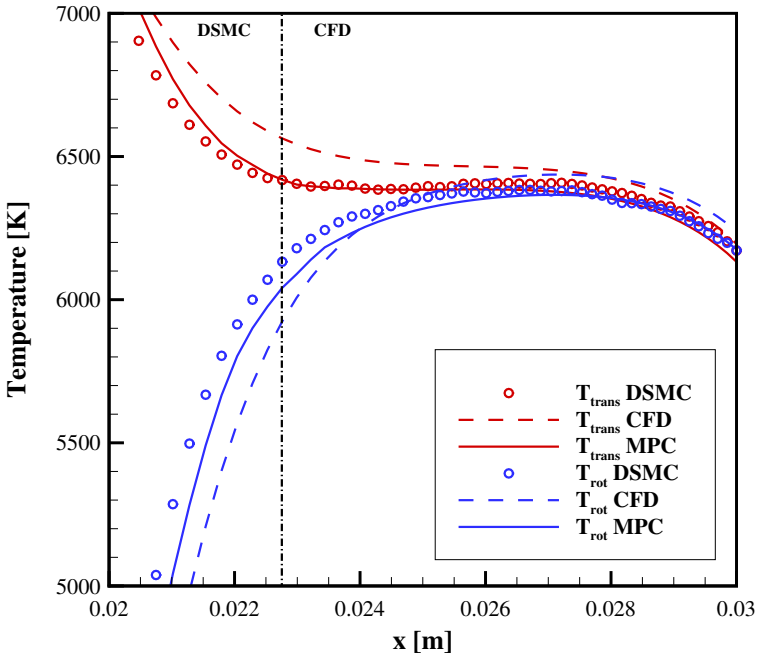

Figure 6.19: Translational and rotational temperatures along the stagnation streamline, with MPC results obtained using the original $Kn_{ROT-NEQ}$ parameter, near the post-shock hybrid interface.

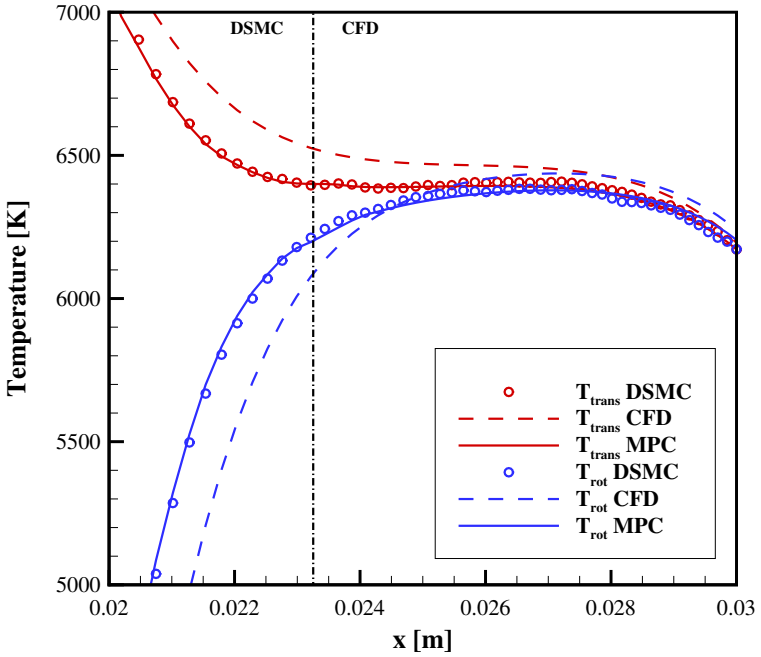

Figure 6.20: Translational and rotational temperatures along the stagnation streamline, with MPC results obtained using the new Kn_{rot} parameter, near the post-shock hybrid interface.

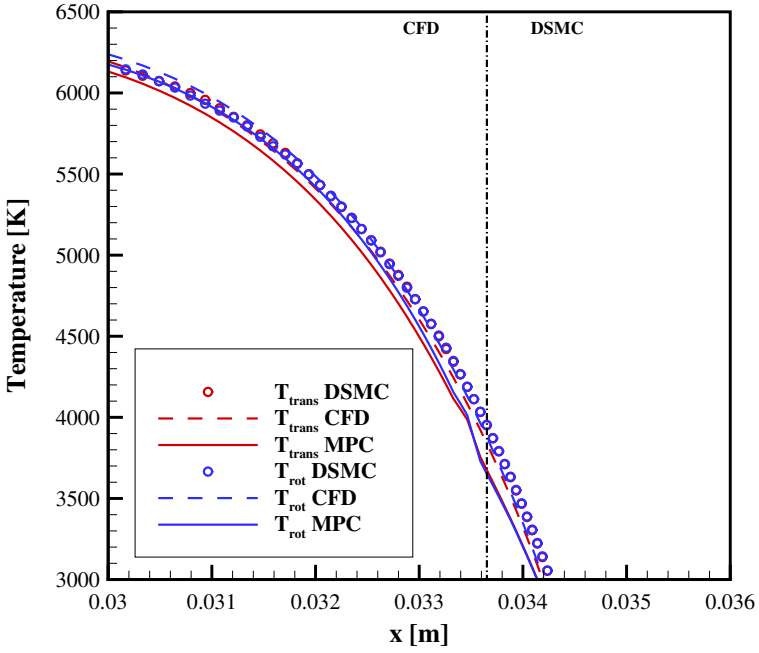

Figure 6.21: Translational and rotational temperatures along the stagnation streamline, with MPC results obtained using the original $Kn_{ROT-NEQ}$ parameter, near the pre-boundary layer hybrid interface.

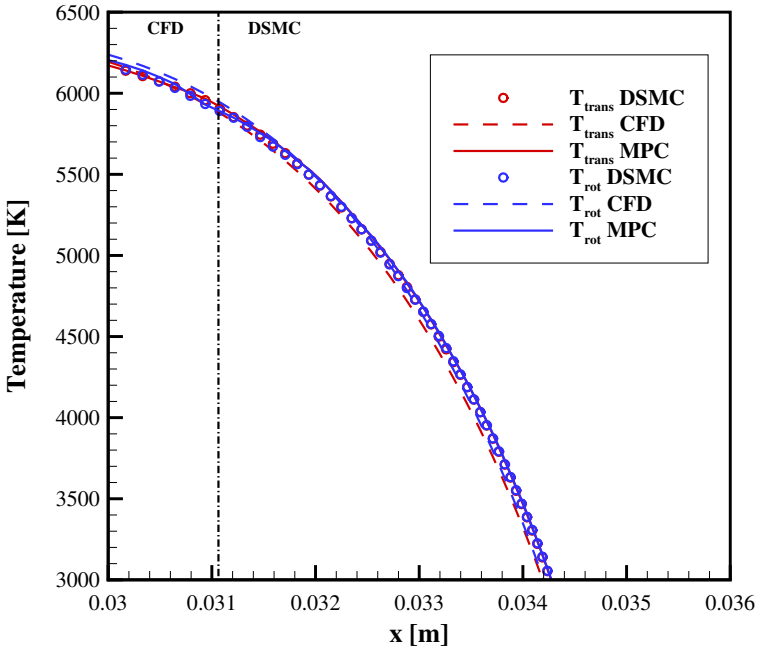

Figure 6.22: Translational and rotational temperatures along the stagnation streamline, with MPC results obtained using the new Kn_{rot} parameter, near the pre-boundary layer hybrid interface.

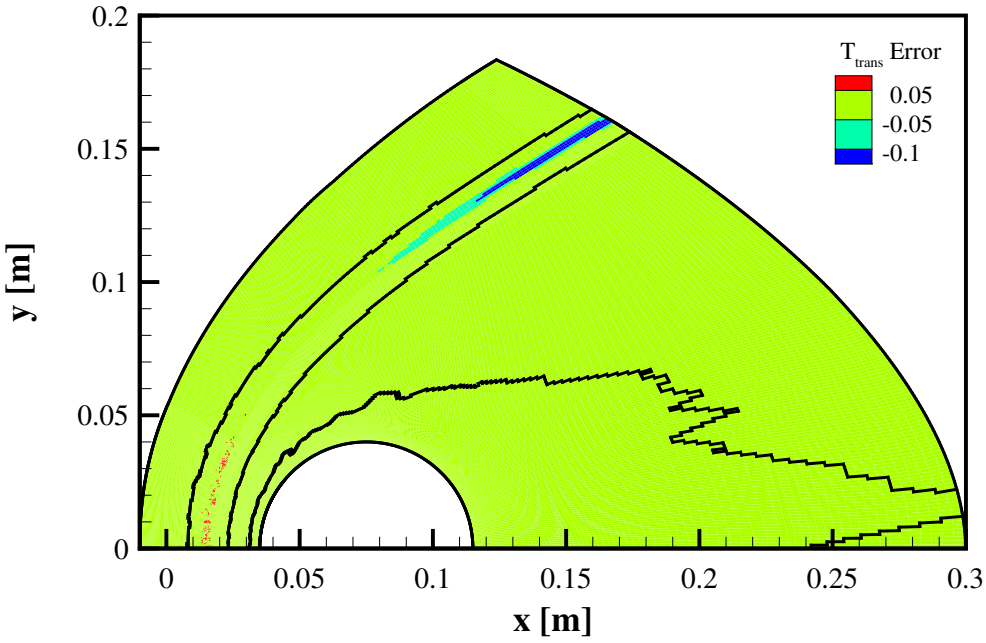

Figure 6.23: Contours of translational temperature errors of the MPC method relative to full DSMC when Kn_{rot} is used, with hybrid interfaces shown as black lines.

errors can be identified as being in either particle or continuum regions of the flow field. Both the physical extent and numerical ranges of these flow field errors, as provided in Table 6.1, have been reduced relative to the baseline accuracy results discussed in Section 5.3. The relative errors of these new MPC results measured in the L_2 norm, which are given in Table 6.2, have also been reduced.

The hybrid interfaces enveloping the shock wave in this Mach 12, Kn_∞ 12 flow of N_2 over a two-dimensional cylinder have remained virtually unchanged, despite the improvements made to the MPC hybrid method in Chapter V and the use of a new rotational nonequilibrium parameter explored in the current chapter. Even so, the physical accuracy of the MPC method relative to full DSMC in the upper shock wave region has improved with each successive development. This result is indicative of numerical errors generated in the fore body being propagated upwards along the shock wave, and highlights the far-reaching effects that the fore body flow has on the rest of the simulation domain.

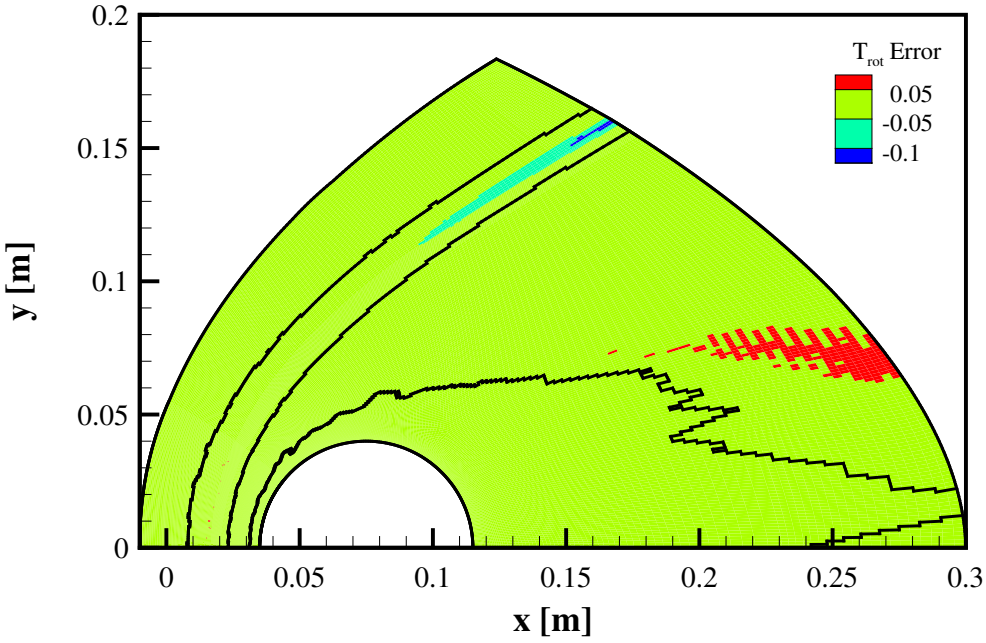

Figure 6.24: Contours of rotational temperature errors of the MPC method relative to full DSMC when Kn_{rot} is used, with hybrid interfaces shown as black lines.

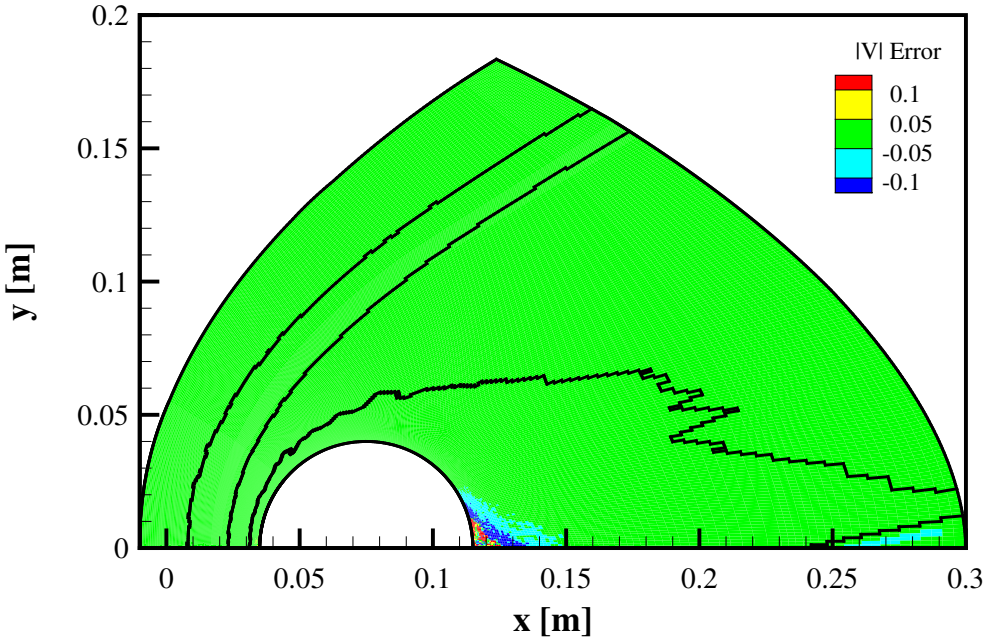

Figure 6.25: Contours of velocity magnitude errors of the MPC method relative to full DSMC when Kn_{rot} is used, with hybrid interfaces shown as black lines.

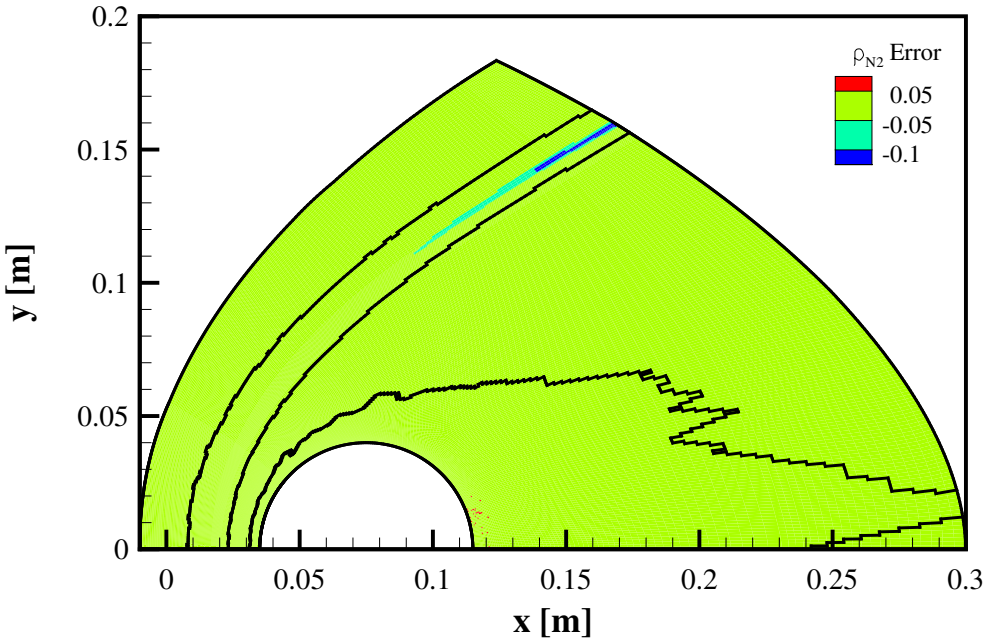

Figure 6.26: Contours of mass density errors of the MPC method relative to full DSMC when Kn_{rot} is used, with hybrid interfaces shown as black lines.

Table 6.1: Ranges of new MPC errors relative to full DSMC for the Mach 12, Kn_∞ 0.01 flow of N_2 over a two-dimensional cylinder.

Property	**New MPC Results**
T_{trans}	-0.15 $\leq \epsilon \leq$ 0.08
T_{rot}	-0.11 $\leq \epsilon \leq$ 0.06
ρ_{N2}	-0.14 $\leq \epsilon \leq$ 0.06

Table 6.2: Relative errors of new MPC results measured in the L_2 norm for the Mach 12, Kn_∞ 0.01 flow of N_2 over a two-dimensional cylinder.

Property	**New MPC Results**
T_{trans}	0.008
T_{rot}	0.011
$\|V\|$	0.005
ρ_{N2}	0.005

6.3.2 Surface Properties

Although it is important that use of the new Kn_{rot} parameter has significantly improved the agreement between MPC and full DSMC in terms of the flow field properties, as discussed in Section 5.3, the physical accuracy of the surface properties is of utmost importance. The profiles of surface pressure coefficient, heat transfer coefficient, and shear stress coefficient as predicted by the MPC method, full CFD, and full DSMC are plotted in Figs. 6.27 through 6.29. There is very little difference between the profiles of surface pressure coefficient predicted by the MPC method when the new Kn_{rot} parameter is used instead of the original $Kn_{ROT-NEQ}$ parameter, as seen in Fig. 6.27. However, there is a noticeable improvement in the profile of heat transfer coefficient when the new rotational nonequilibrium parameter is used. This is the reason why, in past MPC hybrid simulations, the particle region surrounding the boundary layer was forced to extend further upstream than that automatically dictated by the $Kn_{ROT-NEQ}$ parameter. Like the surface pressure coefficient, there is very little difference between MPC predictions of the shear stress coefficient along the cylinder surface, whether the original or new rotational nonequilibrium parameter is used.

The quantitative errors between the surface properties predicted by the MPC method using the new Kn_{rot} parameter and those predicted by a full DSMC simulation are plotted in Figs. 6.30 through 6.32. The largest error in surface pressure coefficient is approximately 5.1%, which is slightly less than the maximum error exhibited in previous results discussed in Section 5.3. A systematic positive error is seen in the wake, but overall, the level of accuracy in the surface pressure coefficient is maintained. The agreement between the heat transfer coefficient profile predicted by the MPC method and full DSMC has noticeably improved as a result of using the new Kn_{rot} parameter. The largest error here is approximately 5.2% and occurs in the wake, which is expected to be problematic because of the reduced number

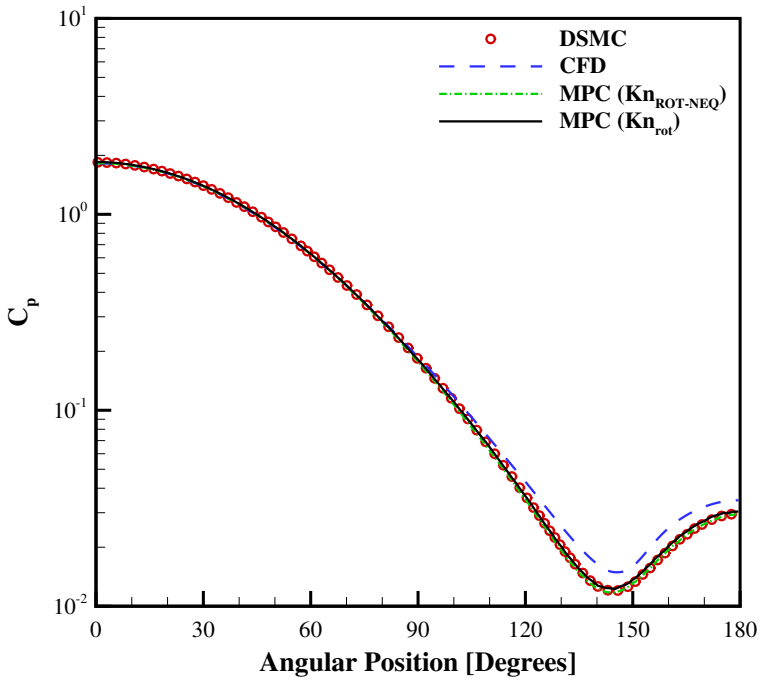

Figure 6.27: Surface pressure coefficient along the cylinder surface for the Mach 12, Kn_∞ 0.01 flow of N_2 over a two-dimensional cylinder.

of simulator particles in this region. The profile of shear stress coefficient also exhibits improved agreement relative to previous results. Whereas the errors between MPC and full DSMC results are still very large near the stagnation point and in the wake region due to near-zero velocity magnitudes, a relative accuracy of $\pm 5\%$ is maintained from an angular position of approximately 12° to 153°. This level of accuracy is maintained over a larger portion of the cylinder surface than when the original $Kn_{ROT-NEQ}$ parameter is used in conjunction with manually increasing the thickness of the boundary layer particle region, as seen in the results of Section 5.3.

6.3.3 Computational Performance

An MPC simulation using the new Kn_{rot} parameter to predict rotational nonequilibrium effects requires approximately 13.4 million DSMC simulator particles, whereas an MPC simulation using the original $Kn_{ROT-NEQ}$ parameter requires approximately 10.8 million particles. However, the latter of these simulations yields surface heat

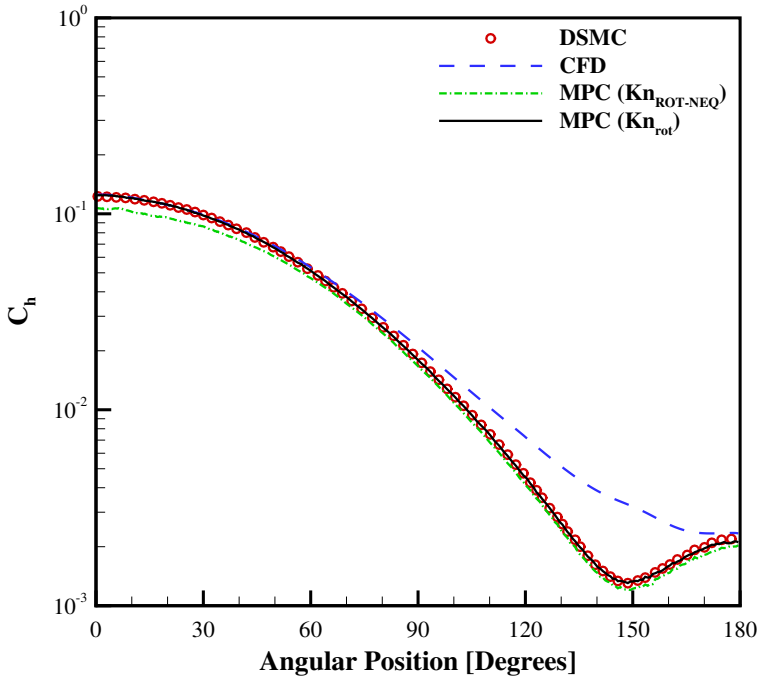

Figure 6.28: Heat transfer coefficient along the cylinder surface for the Mach 12, Kn_∞ 0.01 flow of N_2 over a two-dimensional cylinder.

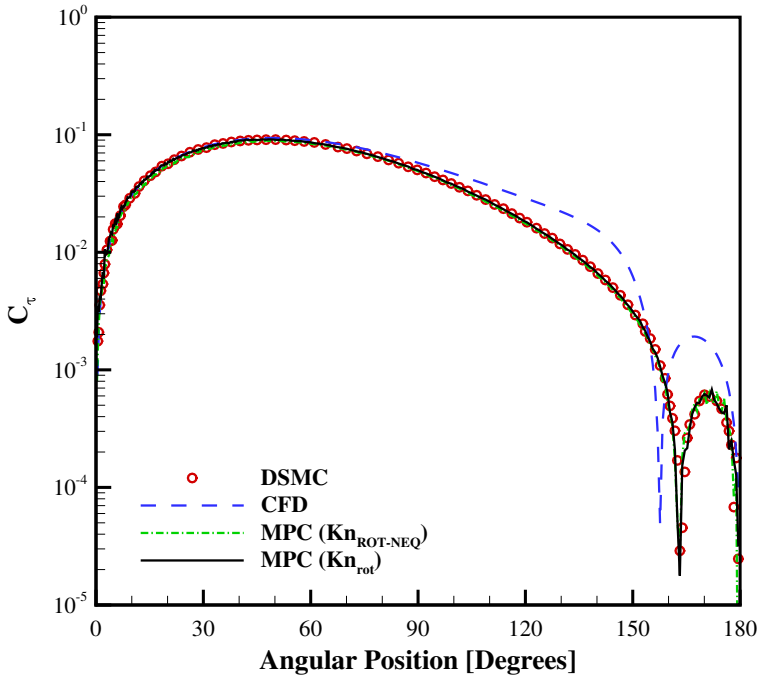

Figure 6.29: Shear stress coefficient along the cylinder surface for the Mach 12, Kn_∞ 0.01 flow of N_2 over a two-dimensional cylinder.

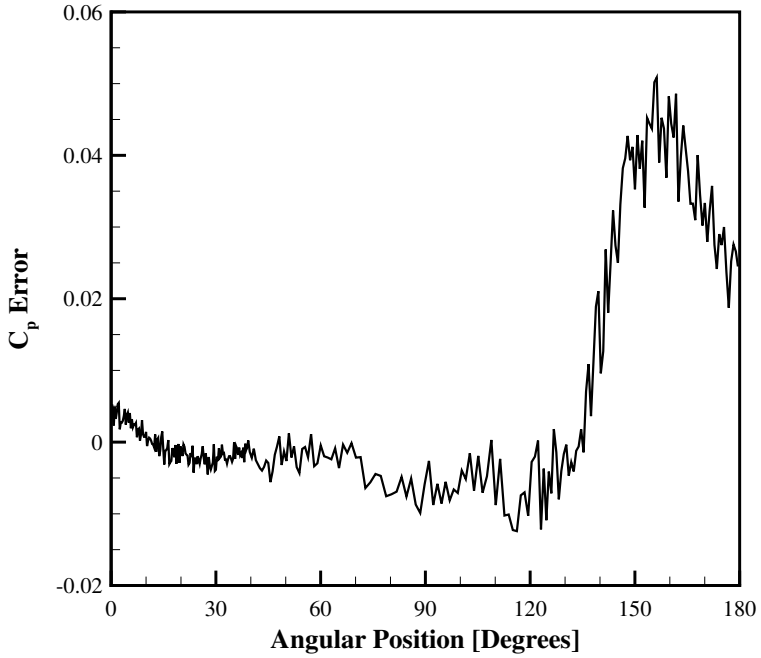

Figure 6.30: Surface pressure coefficient errors of the MPC method relative to full DSMC when Kn_{rot} is used.

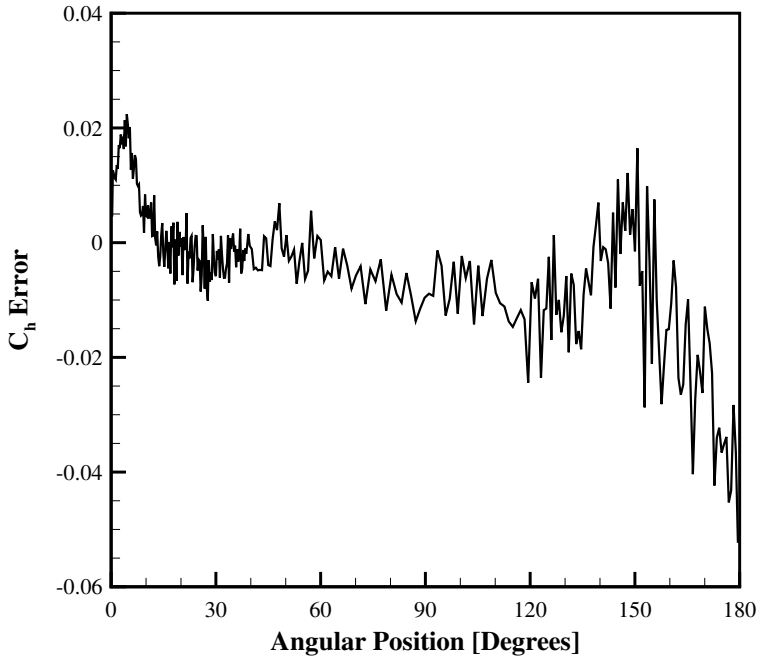

Figure 6.31: Heat transfer coefficient errors of the MPC method relative to full DSMC when Kn_{rot} is used.

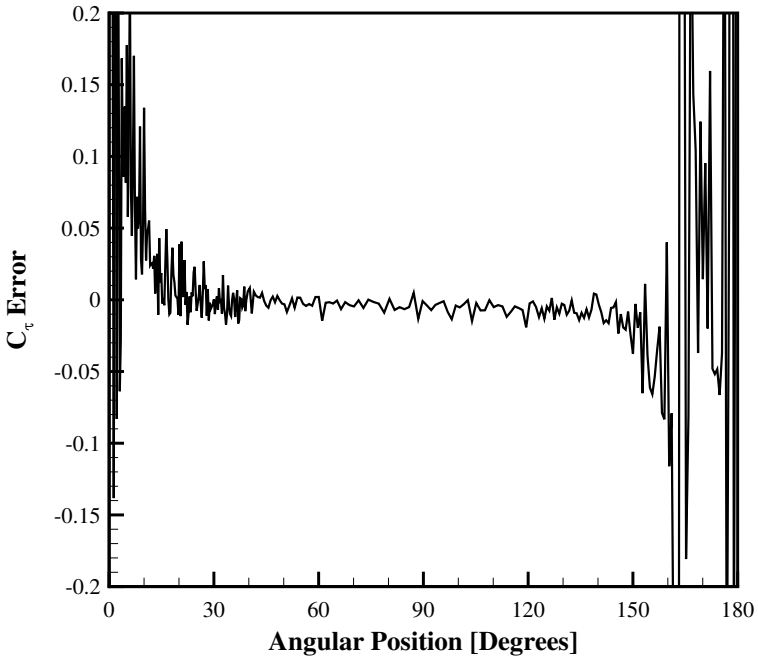

Figure 6.32: Shear stress coefficient errors of the MPC method relative to full DSMC when Kn_{rot} is used.

transfer coefficient results that are in very poor agreement with those from full DSMC, as seen in Fig. 6.28. Because of this, the more meaningful comparison is between those MPC results obtained using the new Kn_{rot} parameter, and those presented at the end of Chapter V, which were obtained by forcing DSMC to be used within $5mm$ of the cylinder surface. In that simulation, approximately 12.2 million particles were required. The particle region surrounding the wake in this most recent simulation is larger compared to that in Chapter V, and this accounts for the increase in the total number of particles.

Based on the number of particles required in this most recent MPC simulation and the number of particles required in the corresponding full DSMC simulation, an ideal speedup factor of 2.13 is calculated. The actual speedup factor as determined by comparing the total computational cost of the MPC simulation (288 hours) and the total computational cost of the full DSMC simulation (763 hours) is 2.65, and surpasses the ideal calculation. There are a couple of reasons why the current MPC

Table 6.3: Computational performance statistics for the Mach 12, Kn_∞ 0.01 flow of N_2 over a two-dimensional cylinder.

	CFD	**DSMC**	**MPC**
Normalized CPU Time	1.0	33.2	12.5
Normalized Memory	1.0	11.5	7.40
# Particles	-	28.5×10^6	13.4×10^6
# Continuum Cells	41,122	-	19,796
# Particle Cells	-	58,809	33,419
# Processors	4	22	10
Sampling/Total DSMC Steps	-	100,000/180,000	100,000/104,040

simulation, which requires a larger number of particles relative to the case presented in Chapter V, appears to require less computational time. For one, because the same number of processors are used in each simulation, there are more particles assigned to each processor in the most recent simulation, and therefore, less computational effort spent communicating between processors. In addition, to determine the variability in measured computational times, three identical DSMC simulations are performed. The resulting computational times differ by as much as 9%, depending on how the processors are divided among computing nodes and other factors. Similarly, the results of the memory profiling software also vary, but to a lesser degree. The computational performance statistics are summarized in Table 6.3.

6.4 Interim Conclusions

In this chapter, detailed comparisons of full DSMC and full CFD results for transitional, hypersonic, blunt-body flows of both a simple gas and a mixture of chemical species were performed. Various continuum breakdown parameters were then evaluated in terms of their ability to predict regions of excessive disagreement between these full DSMC and full CFD solutions along three flow field extraction lines. Although the gradient-length local Knudsen number was examined, too, this study was specifically aimed towards comparing the previously proposed $Kn_{ROT-NEQ}$ parame-

ter for predicting rotational nonequilibrium effects and a new Kn_{rot} parameter. Upon determining a suitable threshold value of 0.2, this new Kn_{rot} parameter was implemented in the MPC method and found to be capable of accurately *and* automatically positioning both the post-shock hybrid interface and the hybrid interface surrounding the boundary layer of the simple gas test case presented earlier in Chapter V. These most recent MPC results exhibit improved accuracy throughout the flow field, including the upper shock region, compared to those results presented in Chapter V. In addition, surface properties are within approximately $\pm 5\%$ of those obtained with a full DSMC simulation, except in regions where macroscopic properties are particularly prone to statistical scatter. Therefore, in future simulations using the MPC method, continuum breakdown will be determined by calculating

$$Br = \max\left(Kn_{GLL-T_{trans}}, Kn_{GLL-\rho}, Kn_{GLL-|V|}, Kn_{GLL-T_{rot}}, Kn_{GLL-e_{vib}}, \frac{1}{4}Kn_{rot}\right), \tag{6.5}$$

and employing a threshold value of 0.05 to determine whether a computational cell is assigned to the particle or continuum domains.

CHAPTER VII

Hybrid Simulations of Mixtures of Chemical Species

One of the objectives of the present work is to extend the capabilities of the MPC hybrid method to include mixtures of chemical species. Such a development not only broadens the applicability of this hybrid approach to more realistic atmospheric flows, but also serves as a preliminary step towards the method's ability to accurately simulate thermochemical nonequilibrium effects in the future. It was shown in Chapter II that consideration of multiple chemical species further complicates the governing equations of fluid flow by requiring an additional transport coefficient that describes mass diffusion effects. A discussion of how the MPC method accommodates multiple chemical species in a gas mixture is first presented. In particular, the topics of continuum breakdown prediction and consistent exchange of information across hybrid interfaces are addressed. The ability of the MPC method to accurately and efficiently simulate gas mixtures is first demonstrated for the case of a Mach 10, Kn_∞ 0.01 flow of 50% N_2/50% N (by mole) over a two-dimensional cylinder; this is the same case for which the new Kn_{rot} rotational nonequilibrium parameter was evaluated in Chapter VI. Next, a gas mixture composed of 80% N_2/20% O_2 (by mole) is considered. Here, the rotational energy modes of N_2 and O_2 are allowed to relax at rates that are independent of one another by employing the particle selection method

for calculating translational-rotational energy exchange probabilities, as described in Chapter IV. Finally, a gas comprised of two species with very different molecular weights is simulated using the MPC hybrid method, and results are compared to both full CFD and full DSMC simulation results. This last case presents an interesting challenge to the MPC method and the assumptions made during its development.

7.1 Multispecies Considerations

In Chapter III, the particle generation procedure proposed by Garcia and Alder [26] for simple, monatomic gases was described. Stephani, *et al.* [75] proposed a similar approach for sampling particle properties—velocities *and* internal energies—from a generalized Chapman-Enskog distribution that is applicable to gas mixtures with internal energy modes. As was seen in Chapter II, the generalized Chapman-Enskog distribution function is much more involved than that describing a simple, monatomic gas. A rigorous derivation was presented, and the necessity of the generalized Chapman-Enskog formulation was evaluated in the context of hypersonic, flat-plate boundary layer flow and hypersonic flow over a two-dimensional cylinder involving a five-species air mixture. For these cases, the magnitudes of the other transport processes were much larger than that of mass diffusion. Therefore, it was determined that the effect of including the mass diffusion in both the prediction of continuum breakdown and the sampling of particle properties was negligible. In addition, although the rotational and vibrational heat fluxes were found to contribute substantially to continuum breakdown in the boundary layer flow, these specific transport terms were not required to accurately predict the onset of nonequilibrium effects upstream of the bow shock wave. The post-shock region and stagnation point were not examined in this analysis, however, so no valid conclusions could be drawn regarding the relative importance of the various perturbation terms of the generalized Chapman-Enskog distribution in these regions.

For this first application of the MPC hybrid method in simulating gas mixtures, several simplifying assumptions are made. Regarding the prediction of continuum breakdown that was explored in Chapter VI, besides accounting for the mass density of each component species separately, there are no additional terms considered in the breakdown calculation when a gas mixture is simulated. Any significant changes in mixture composition should be observable in the gradient-length local Knudsen number calculated for the density of each species. Also, as noted in Chapter IV, the particle domains of the MPC hybrid simulations and full DSMC simulations presented here employ the VHS collision model, which assumes that simulator particles are isotropically scattered upon colliding. Although capable of accurately reproducing the macroscopic coefficient of viscosity, the VHS model is not capable of accurately capturing mass diffusion effects. Therefore, it does not make sense at this stage of development to include the mass diffusion perturbation of the Chapman-Enskog distribution function when sampling particle properties along hybrid interfaces; the increased accuracy provided by this more rigorous approach cannot be sustained in the particle domains. Excluding the mass diffusion when generating new simulator particles is also consistent with the observations made by Stephani, *et al.* [75].

Based on these assumptions, the same particle generation procedure proposed by Garcia and Alder [26] is used for sampling particle properties in MPC simulations involving gas mixtures. The only difference is that the normalized shear stress and translational heat flux are now calculated using the mixture rules described in Chapter IV. This results in all newly generated particles for each species having the same average velocity, i.e. the diffusion velocity is assumed to be zero, while the differences in molecular weight are used to alter the spread of the distribution functions, resulting in different thermal velocities. For example, if a binary gas mixture comprised of species A and B is considered, the average velocity of all newly generated A particles will be the same as the average velocity of all newly generated B particles. However,

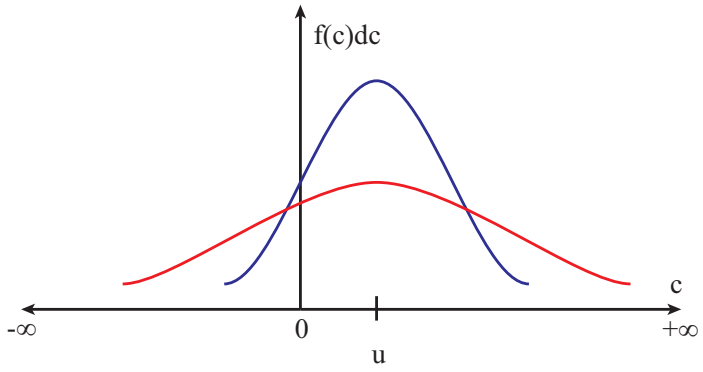

Figure 7.1: Illustration of two different VDFs, where the molecular weight of particles represented by the red line is less than that of the particles represented by the blue line.

if each A particle has a lower mass than each B particle, their individual molecular velocities will be sampled from a wider distribution, as illustrated in Fig. 7.1.

7.2 Verification of the MPC Method: 50% N_2/50% N

Using the physical models described in Chapter IV, the Mach 10, Kn_∞ 0.01 flow of 50% N_2/50% N (by mole) over a two-dimensional cylinder is simulated using the MPC hybrid method. In particular, the particle module employs the VHS model parameters for the N_2-N_2, N_2-N, and N-N collision classes that were derived to be consistent with the Gupta Mixing Rule used in the continuum module. This is the same case examined in Section 6.2.2, where full CFD and full DSMC simulation results were compared in order to assess the merits of the various continuum breakdown parameters used in this work. For meaningful flow field, surface property, and computational performance comparisons, the same cell-based numerical weights that were used in the full DSMC simulation are also used in this hybrid simulation. The time step size and total number of sampled time steps are also specified to be the same.

The initial and final hybrid interfaces automatically determined by the MPC method for this flow field are plotted in Fig. 7.2. Again, the post-shock and pre-boundary layer hybrid interfaces remain relatively stationary throughout the course

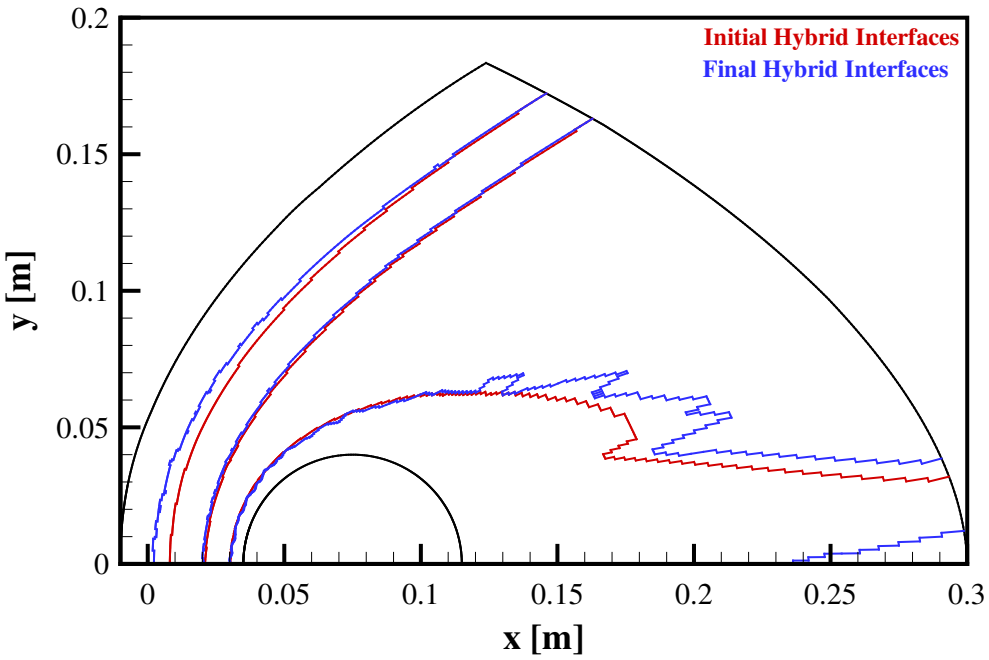

Figure 7.2: Initial and final hybrid interfaces for the Mach 10, Kn_∞ 0.01 flow of 50% N_2/50% N over a two-dimensional cylinder.

of the simulation. However, as the initial CFD solution of the shock wave is improved by the DSMC method, the pre-shock hybrid interface moves upstream substantially. This accommodates the thicker, more diffuse shock wave that results when the strong nonequilibrium effects are accurately simulated. It should be reiterated that the continuum breakdown parameters used here, namely, the gradient-length local Knudsen number and the Kn_{rot} parameter introduced in the previous chapter, have automatically positioned these hybrid interfaces. The only user-defined parameters are the empirically determined threshold values that differentiate what are considered near-equilibrium and nonequilibrium computational cells.

7.2.1 Flow Field Properties

A comparison of the contours of velocity magnitude obtained with full DSMC, full CFD, and the MPC hybrid method is shown in Fig. 7.3. The results obtained with the MPC method are in excellent agreement with the full DSMC results, as ev-

idenced by the nearly indistinguishable flooded and lined contours in the upper pane of Fig. 7.3. There are slight discrepancies in the near-wake region, but the accuracy of the initial continuum solution has been greatly improved. For context, the contours of velocity magnitude predicted by the full DSMC and full CFD simulations are shown in the lower pane. As expected, the CFD solution indicates the shock onset to be much further downstream than in the DSMC solution, and the shock thickness is also under predicted. The CFD solution also exhibits a larger wake region, which will become more apparent in the surface properties discussed later in this section. Similar conclusions can be drawn from the contours of translational temperature and rotational temperature plotted in Figs. 7.4 and 7.5, respectively. One observation worth emphasizing is seen in the near-wake region of Fig. 7.5. There is an abrupt decline in the agreement between the results obtained with full DSMC and the MPC method that occurs along the hybrid interface. This may indicate that the flow field has not reached a true steady state at the time the hybrid interfaces are locked, which is possible considering the reduced collisionality in this region. This discrepancy may also be due to the manner in which rotational energies are sampled and assigned to newly generated particles along hybrid interfaces. Deschenes, *et al.* [22] proposed sampling from a Boltzmann distribution defined by the macroscopic rotational temperature, but the generalized Chapman-Enskog distribution may, in fact, be required to achieve the same physical accuracy as the full DSMC simulation. This discrepancy between contours of rotational temperature can also be observed in the simple gas results shown in Fig. 6.16.

The relative errors in macroscopic fluid properties between the MPC flow field results and those obtained with full DSMC are plotted in Figs. 7.6 through 7.10. The numerical ranges of these errors, which are given in Table 7.1, are consistent with those calculated for the simple gas case evaluated in Chapter VI. The relative errors measured in the L_2 norm for these MPC results are again much smaller than

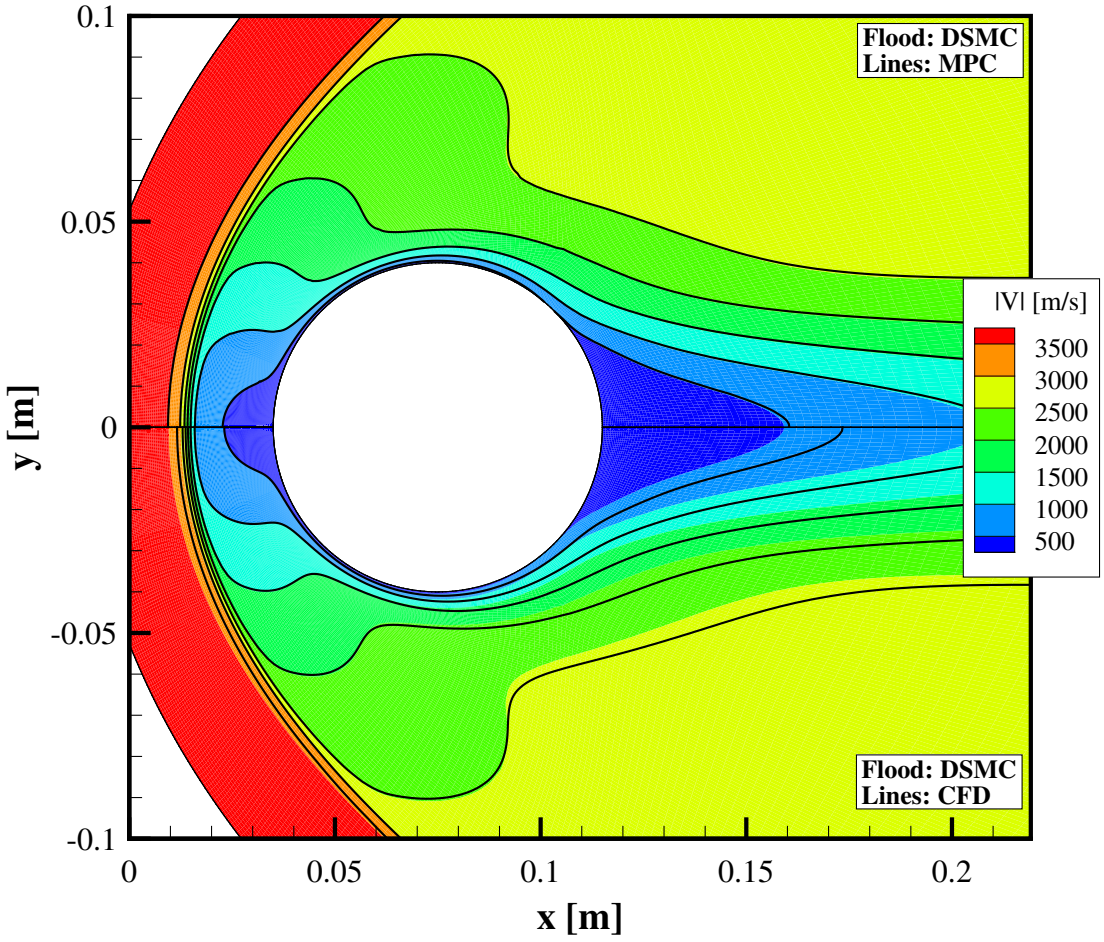

Figure 7.3: Contours of velocity magnitude for the Mach 10, Kn_∞ 0.01 flow of 50% N_2/50% N over a two-dimensional cylinder.

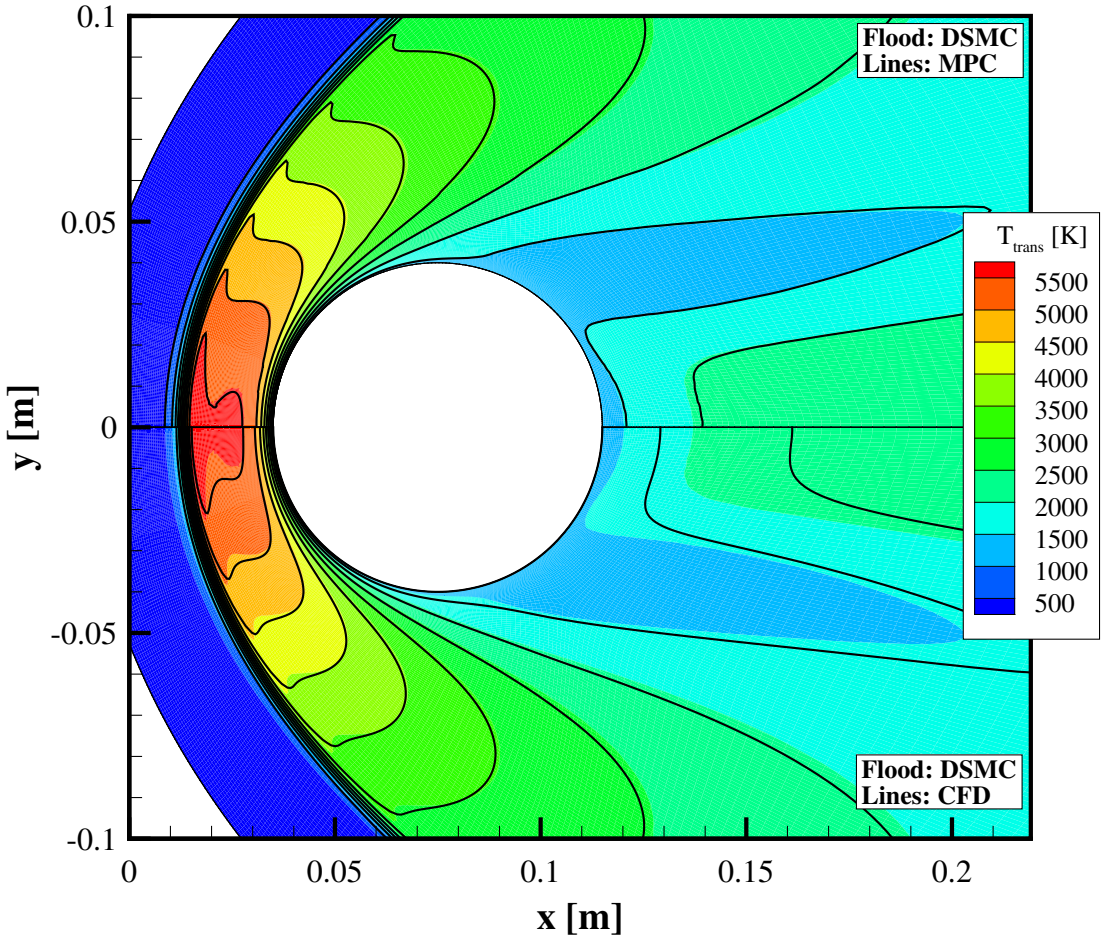

Figure 7.4: Contours of translational temperature for the Mach 10, Kn_∞ 0.01 flow of 50% N_2/50% N over a two-dimensional cylinder.

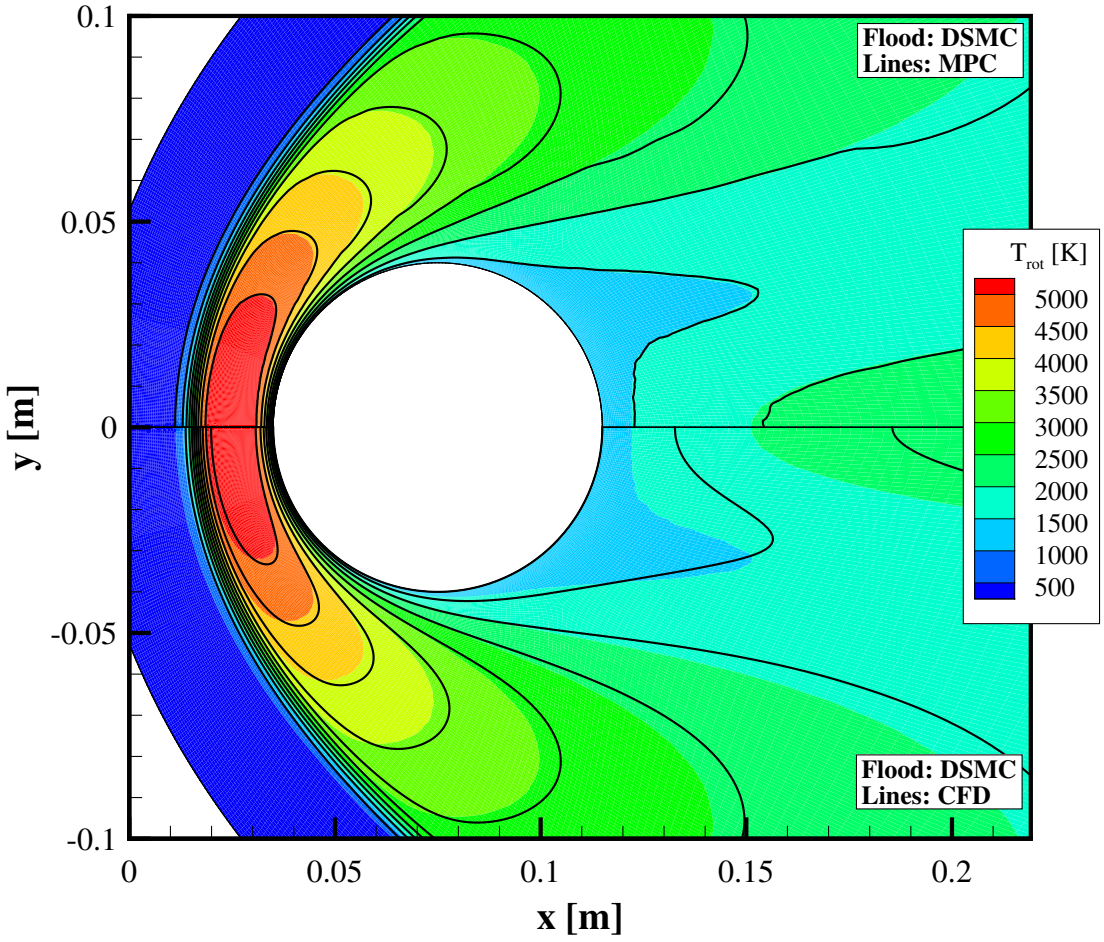

Figure 7.5: Contours of rotational temperature for the Mach 10, Kn_∞ 0.01 flow of 50% N_2/50% N over a two-dimensional cylinder.

Table 7.1: Ranges of errors relative to full DSMC for the Mach 10, Kn_∞ 0.01 flow of 50% N_2/50% N over a two-dimensional cylinder.

Property	**MPC Results**	**CFD Results**
T_{trans}	-0.11 $\leq \epsilon \leq$ 0.07	-0.76 $\leq \epsilon \leq$ 0.17
T_{rot}	-0.09 $\leq \epsilon \leq$ 0.07	-0.66 $\leq \epsilon \leq$ 0.06
ρ_{N2}	-0.10 $\leq \epsilon \leq$ 0.06	-0.05 $\leq \epsilon \leq$ 0.61
ρ_N	-0.08 $\leq \epsilon \leq$ 0.06	-0.13 $\leq \epsilon \leq$ 0.36

Table 7.2: Relative errors measured in the L_2 norm for the Mach 10, Kn_∞ 0.01 flow of 50% N_2/50% N over a two-dimensional cylinder.

Property	**MPC Results**	**CFD Results**
T_{trans}	0.008	0.054
T_{rot}	0.010	0.061
$\|V\|$	0.005	0.042
ρ_{N2}	0.011	0.035
ρ_N	0.012	0.175

those calculated for the full CFD results, as shown in Table 7.2. In terms of the locations of these errors throughout the computational domain, it appears that the extents of the errors in the fore body region are slightly more pronounced, while the extents of the errors in the upper shock region are slightly less pronounced, compared to the previous simple gas case. Again, because of the very large gradients in the shock wave, even very small discrepancies in the shock wave location can lead to remarkably large errors. Therefore, errors in this region are somewhat expected and may be unavoidable even in the most simple of simulations. As shown in Fig. 7.7, the most notable difference between the gas mixture and simple gas cases is observed in the rotational temperature prediction in the wake. Here, the MPC hybrid solution is within 5% of the full DSMC solution except for a few computational cells near the outflow boundary.

Although mass diffusion effects cannot be accurately simulated using the VHS collision model in DSMC, the variation of mixture composition as the flow of 50% N_2/50% N traverses the shock wave and boundary layer is observed. To illustrate this, the mole fraction of N_2 is plotted along the stagnation streamline in Fig. 7.11. Of particu-

lar interest is the reduced population of N_2 molecules within the shock wave, which is caused by the N_2 molecules having a larger average velocity than the N atoms. This separation effect is due to baro-diffusion, which tends to *accelerate* heavier molecules, overcoming thermal diffusion, which tends to *decelerate* heavier molecules [69]. It should be noted that in the approximate diffusion flux used in the present continuum approach, baro-diffusion and thermal diffusion are neglected. The MPC method reproduces the same separation effect predicted by full DSMC in the shock wave, whereas the limited ability of CFD to accurately simulate strong nonequilibrium effects results in a minor depression in the N_2 mole fraction.

As shown in Fig. 7.11, even though there is a region between the shock wave and boundary layer particle regions where the continuum module is used, because of the improved boundary conditions provided by these particle regions, the MPC method is in better agreement with full DSMC than CFD is able to achieve alone. Therefore, rather than predicting the same N_2 mole fraction as the freestream value of 0.5, the MPC method and full DSMC predict a slightly higher post-shock N_2 mole fraction, which then decreases prior to increasing in the boundary layer. Although there is a noticeable discrepancy between full DSMC and the MPC method near the pre-boundary layer hybrid interface, this discrepancy is less than 2%. Again, the full CFD simulation yields a slight increase in the N_2 mole fraction in the boundary layer, whereas both full DSMC and the MPC method predict mole fractions of approximately 0.57.

7.2.2 Surface Properties

As they were defined in Eqs. 5.10 through 5.12, the surface pressure, heat transfer, and shear stress coefficients calculated along the cylinder surface are plotted in Figs. 7.12 through 7.14. The MPC method is able to reproduce full DSMC results for this gas mixture case to within the same accuracy observed in the simple gas case.

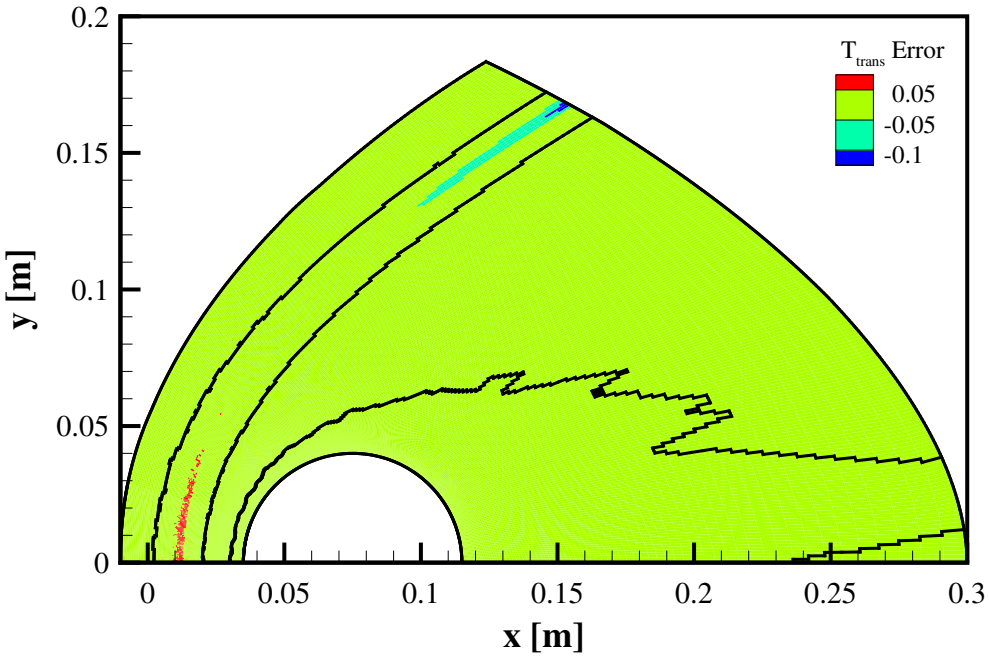

Figure 7.6: Contours of translational temperature errors of the MPC method relative to full DSMC for the Mach 10, Kn_∞ 0.01 flow of 50% N_2/50% N over a two-dimensional cylinder; hybrid interfaces are shown as black lines.

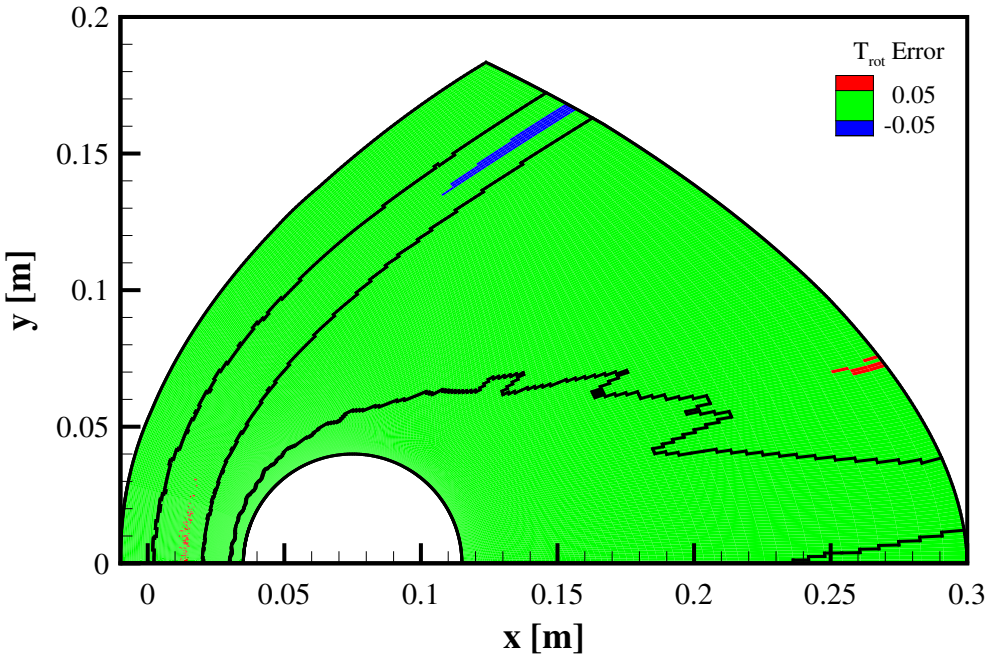

Figure 7.7: Contours of rotational temperature errors of the MPC method relative to full DSMC for the Mach 10, Kn_∞ 0.01 flow of 50% N_2/50% N over a two-dimensional cylinder; hybrid interfaces are shown as black lines.

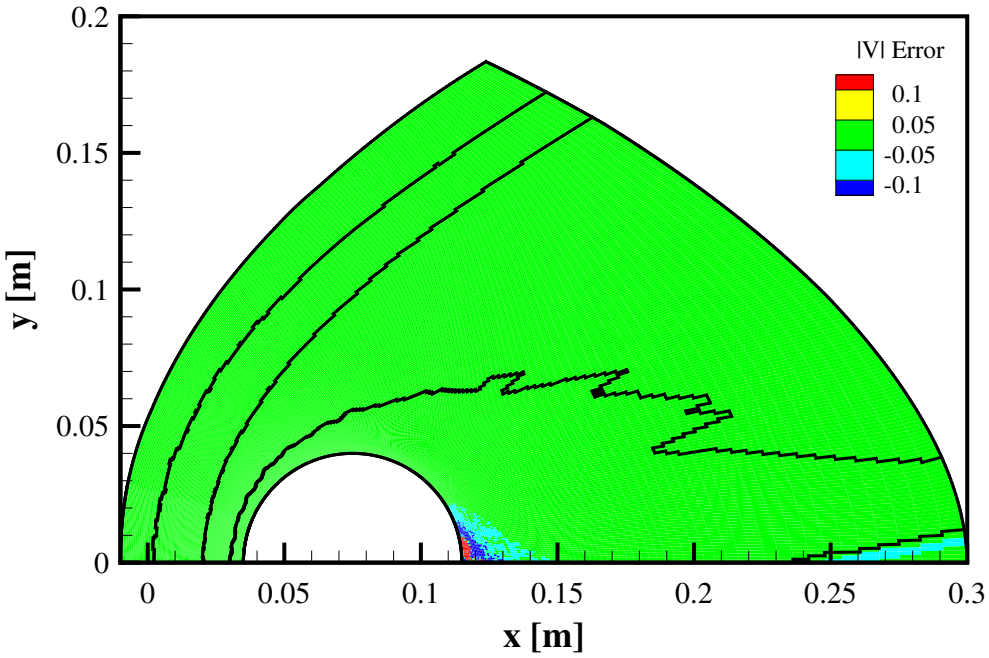

Figure 7.8: Contours of velocity magnitude errors of the MPC method relative to full DSMC for the Mach 10, Kn_∞ 0.01 flow of 50% N_2/50% N over a two-dimensional cylinder; hybrid interfaces are shown as black lines.

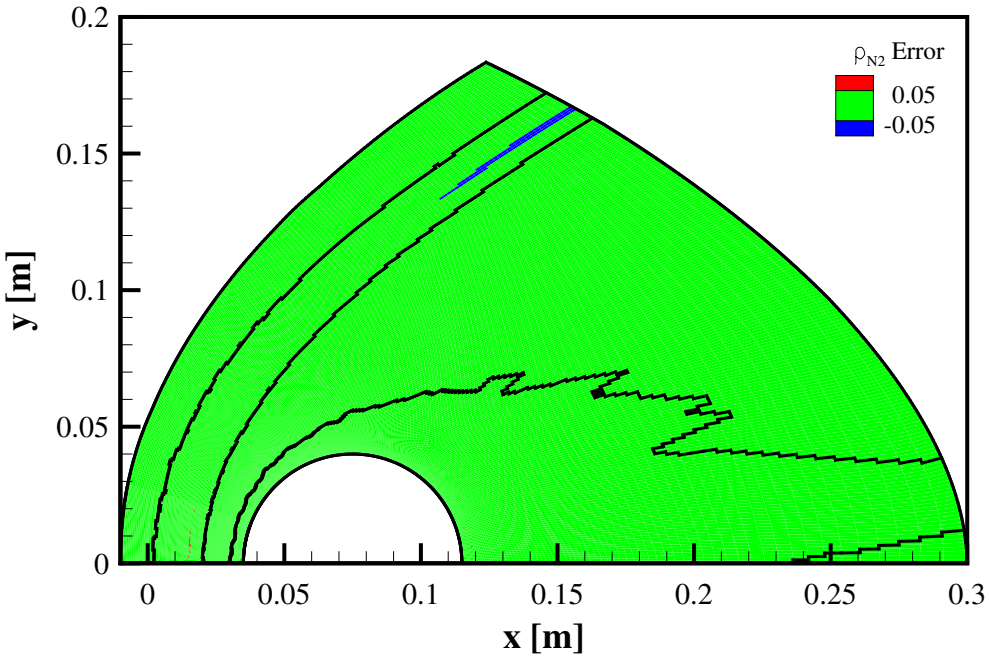

Figure 7.9: Contours of N_2 mass density errors of the MPC method relative to full DSMC for the Mach 10, Kn_∞ 0.01 flow of 50% N_2/50% N over a two-dimensional cylinder; hybrid interfaces are shown as black lines.

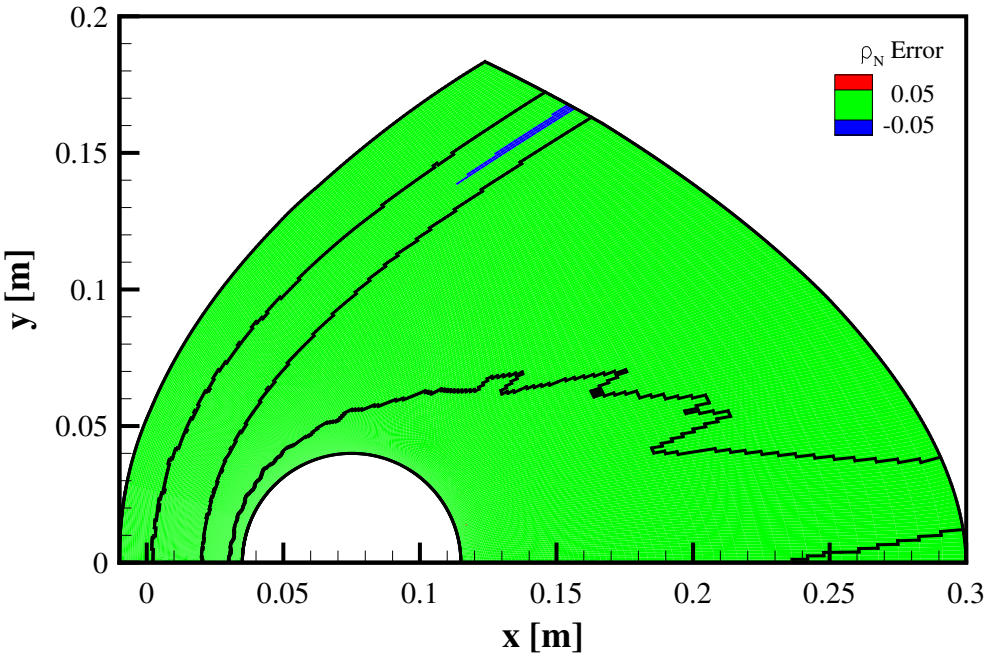

Figure 7.10: Contours of N mass density errors of the MPC method relative to full DSMC for the Mach 10, Kn_∞ 0.01 flow of 50% N_2/50% N over a two-dimensional cylinder; hybrid interfaces are shown as black lines.

Whereas CFD results over predict the surface pressure coefficient over the entire aft body, the solution obtained using the MPC method is within ±5% of that obtained using the DSMC method throughout the entire computational domain. Because of the no-slip condition imposed in the CFD simulation, the resulting heat transfer coefficient profile is over predicted across the entire cylinder surface, as shown in Fig. 7.13. The MPC method is able to improve upon this initial continuum solution and recover the profile of the heat transfer coefficient predicted by full DSMC to within ±5%. The profiles of shear stress coefficient along the cylinder surface are plotted in Fig. 7.14, where the larger wake region previously noted in the CFD solution is again illustrated. Because of the heightened level of statistical scatter observed near the fore stagnation point and in the wake, an accuracy of ±5% is maintained between the angular positions of 15° and 155°. The MPC method and full DSMC predict the point of incipient separation in the wake to occur within 1° of each other.

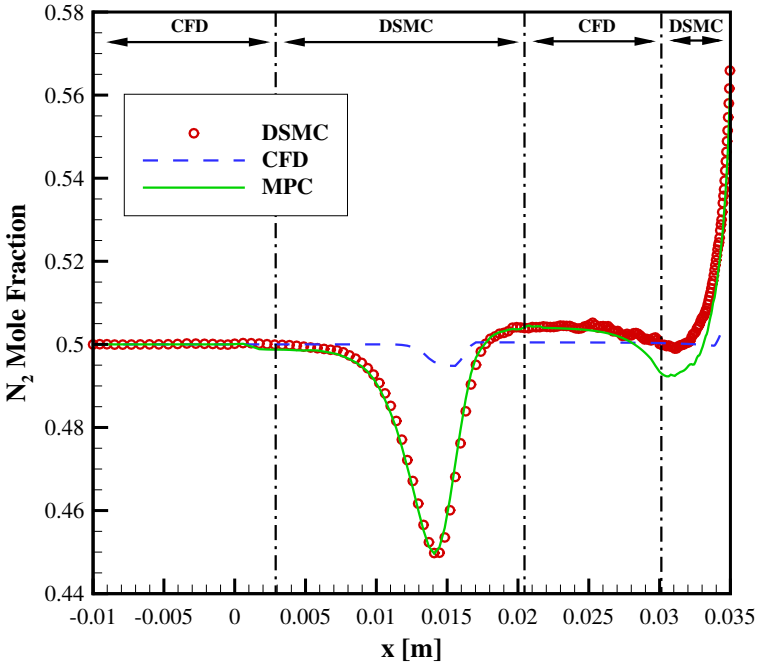

Figure 7.11: N_2 mole fraction along the stagnation streamline for the Mach 10, Kn_∞ 0.01 flow of 50% N_2/50% N over a two-dimensional cylinder.

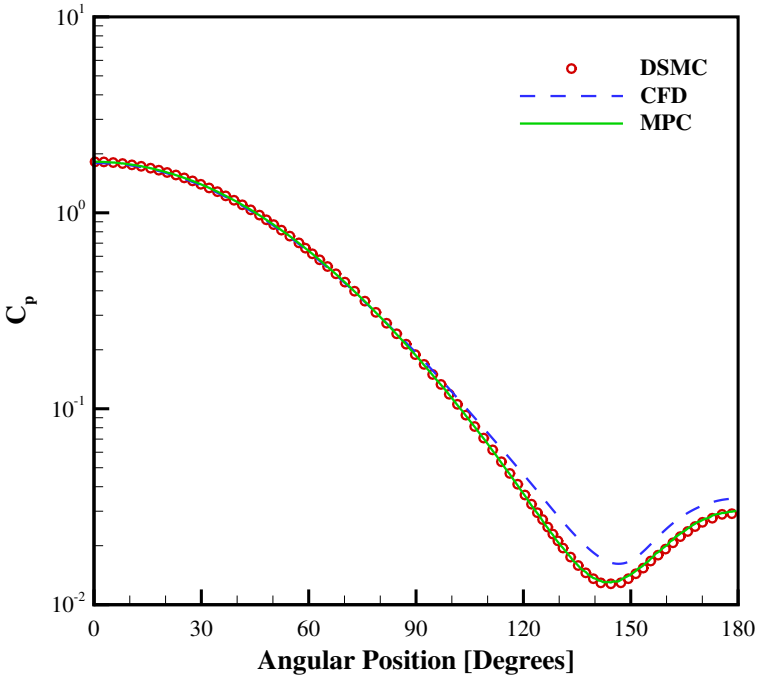

Figure 7.12: Surface pressure coefficient along the cylinder surface for the Mach 10, Kn_∞ 0.01 flow of 50% N_2/50% N.

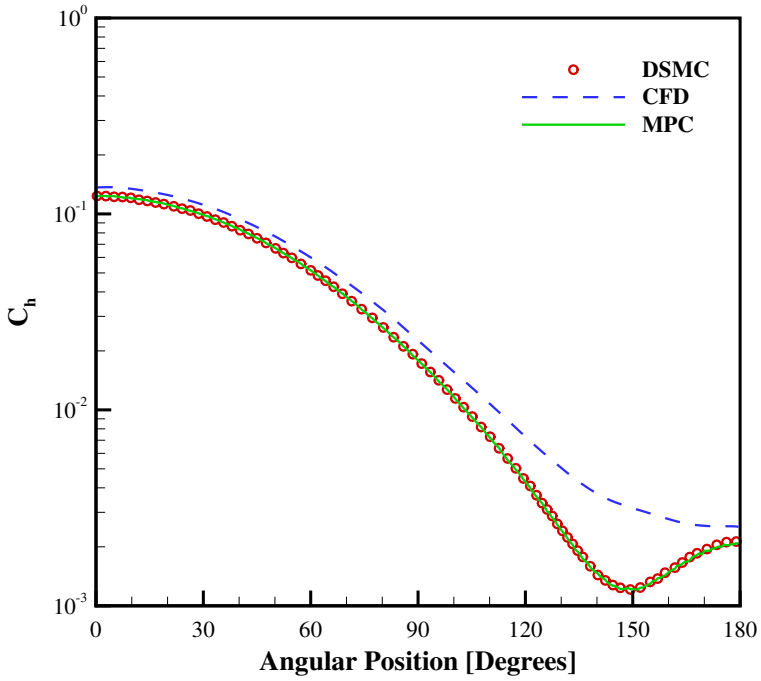

Figure 7.13: Heat transfer coefficient along the cylinder surface for the Mach 10, Kn_∞ 0.01 flow of 50% N_2/50% N.

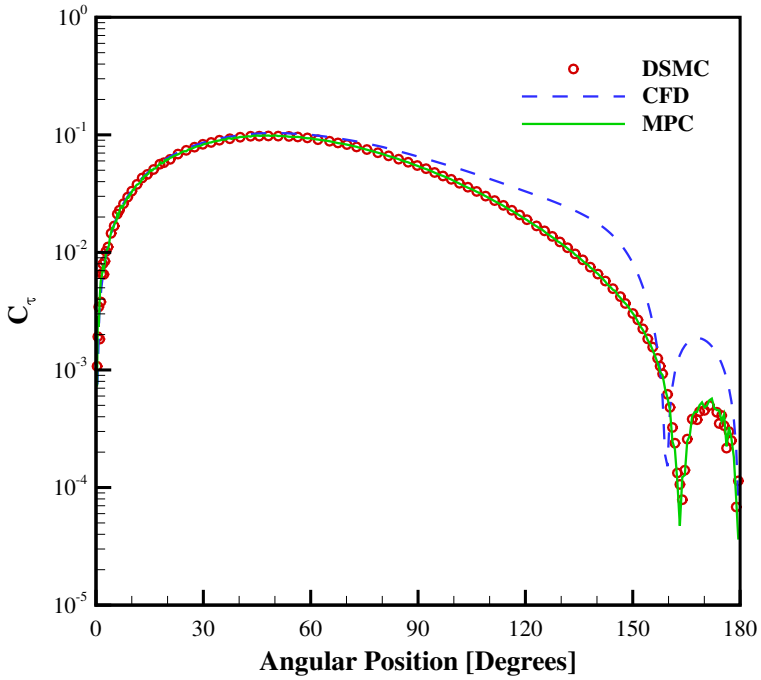

Figure 7.14: Shear stress coefficient along the cylinder surface for the Mach 10, Kn_∞ 0.01 flow of 50% N_2/50% N.

Table 7.3: Computational performance statistics for the Mach 10, Kn_∞ 0.01 flow of 50% N_2/50% N over a two-dimensional cylinder.

	CFD	**DSMC**	**MPC**
Normalized CPU Time	1.0	30.0	11.9
Normalized Memory	1.0	16.6	10.8
# Particles	-	47.1×10^6	21.3×10^6
# Continuum Cells	41,122	-	18,602
# Particle Cells	-	47,638	27,953
# Processors	4	40	18
Sampling/Total DSMC Steps	-	100,000/180,000	100,000/105,050

7.2.3 Computational Performance

Except for the computational cells near the cylinder surface, a constant numerical weight is specified throughout the simulation domain such that there are at least 40 particles per cell. Assuming the freestream mole fraction is maintained everywhere, this results in approximately 20 particles of each species per cell. As a result, the MPC hybrid simulation requires 21.3 million simulator particles, and the full DSMC simulation requires 47.1 million simulator particles, making this gas mixture case more computationally demanding than that for a simple gas. Therefore, the ideal speedup factor is approximately 2.21. Based on the total computational cost of each simulation, the actual speedup factor is approximately 2.52, which is higher than the ideal, as was the case with the simple gas simulation presented in Chapter VI. The number of processors was chosen such that the same number of particles are simulated on each processor. Whereas 80,000 time steps are required prior to sampling in the full DSMC simulation, the hybrid interfaces are locked and sampling begins after only 5,050 DSMC time steps in the hybrid simulation, which accounts for the better than ideal speedup factor. Also, the MPC simulation requires approximately 35% less memory than the full DSMC simulation. A summary of these computational performance statistics is provided in Table 7.3.

7.3 Verification of the MPC Method: 80% N_2/20% O_2

In order to accommodate even the most simple atmospheric gas mixture, the MPC method must allow for each polyatomic species to experience rotational relaxation independently. This is accomplished through the use of the particle selection methodology described in Chapter IV, where each collision partner is examined sequentially to determine whether or not a rotational relaxation event occurs. Both the MPC method and the MONACO DSMC code used for verification now employ this selection methodology. In the current section, these modifications are verified by simulating a Mach 10, Kn_∞ 0.01 flow of 80% N_2/20% O_2 (by mole) over a two-dimensional cylinder. Vibrational excitation is again neglected in this simulation, enabling a more straightforward assessment of the MPC method and its ability to accurately simulate mixtures of polyatomic species in rotational nonequilibrium. The global Knudsen number is calculated as the ratio of the freestream mean free path to the cylinder diameter, giving a freestream density of $6.415 \times 10^{-5} kg/m^3$ and $1.832 \times 10^{-5} kg/m^3$ for N_2 and O_2, respectively, assuming a freestream temperature of $217.45K$. The freestream velocity is specified to be $2965m/s$, and the cylinder surface is maintained at a constant temperature of $1{,}000K$. The physical models employed in the continuum and particle approaches are detailed in Chapter IV, and the relevant parameters for each species and collision class are provided in Appendix A.

The LeMANS finite volume CFD solver is first used to obtain a grid-independent continuum solution, which requires approximately 41,100 computational cells. The MPC method is then initialized with this continuum solution and mesh. The various continuum breakdown parameters defined in Eq. 6.5 are then calculated based on this initial continuum solution, and the computational domain is divided into particle and continuum regions, depending on the estimated level of thermodynamic nonequilibrium. Most importantly, the Kn_{rot} threshold value of 0.2 that was determined for the simple N_2 gas and the 50% N_2/50% N gas mixture is verified to be adequate for

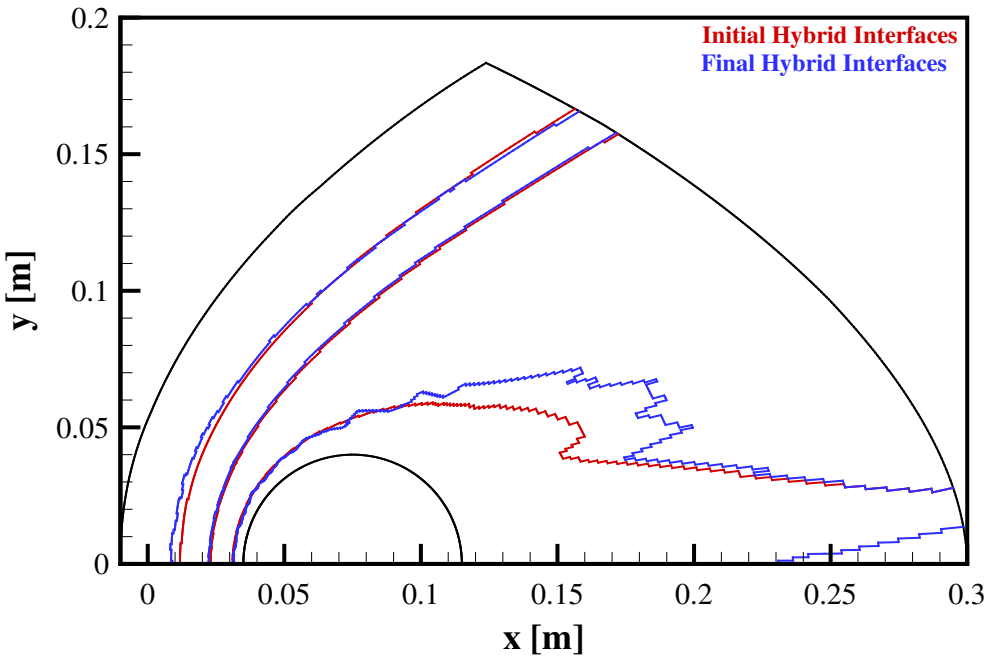

Figure 7.15: Initial and final hybrid interfaces for the Mach 10, Kn_∞ 0.01 flow of 80% N_2/20% O_2 over a two-dimensional cylinder.

this mixture by executing the same procedure detailed in Chapter VI. The initial and final hybrid interfaces for this MPC simulation are plotted in Fig. 7.15, and are similar to those shown for the cases that have been previously discussed.

The particle regions are updated using a constant time step of $1 \times 10^{-8}s$, which is verified to be less than the local mean collision time throughout the computational domain; the maximum time step allowed in the continuum regions is $1 \times 10^{-7}s$. A constant numerical weight of 2×10^{12} is adequate to maintain at least 40 DSMC simulator particles per cell. However, reduced cell-based numerical weights are employed near the cylinder surface to increase the number of particles that contribute to the calculation of various surface properties. It should be noted that for this mixture composition, approximately 100 particles per cell would be required in order to maintain at least 20 particles representing O_2 in each cell. However, this would result in the full DSMC simulation requiring more than 100 million particles—a very computationally intensive simulation.

7.3.1 Flow Field Properties

Contours of various macroscopic fluid properties as predicted by full CFD, full DSMC, and the MPC hybrid method are presented in Figs. 7.16 through 7.18. There is excellent agreement between the MPC method and DSMC, with minor differences in the near-wake region, as was also the case with the 50% N_2/50% N mixture. In addition, there appear to be discrepancies in both the translational and rotational temperatures in the fore body. Further investigation reveals, however, that this is merely an artifact of the chosen contour levels; although the full DSMC simulation predicts slightly higher post-shock temperatures along the stagnation streamline, the profiles are still in very good agreement. The numerical ranges of errors between the MPC method and full DSMC results are provided in Table 7.4, and the relative errors measured in the L_2 norm are given in Table 7.5. The locations of these errors throughout the simulation domain are plotted in Figs. 7.19 through 7.23. Comparisons of these error contours and those from the simple N_2 gas and the 50% N_2/50% N gas mixture show that both the magnitudes and locations of these flow field errors are fairly consistent. There are, however, substantially higher errors in the mass densities predicted by the MPC method in the current simulation. It is interesting to note that the level of error seems to be correlated with the number of time steps used to update the particle domains prior to locking the hybrid interfaces. In addition, the O_2 species concentration is the lowest of any mixture component examined here, and the range of errors exhibited by the O_2 mass density is also the largest, suggesting that use of more simulator particles to represent O_2 molecules would increase the agreement between the MPC and full DSMC results. Finally, the mixture composition varies very little through the shock wave and in the boundary layer, so comparisons of the N_2 mole fraction are not shown for this case.

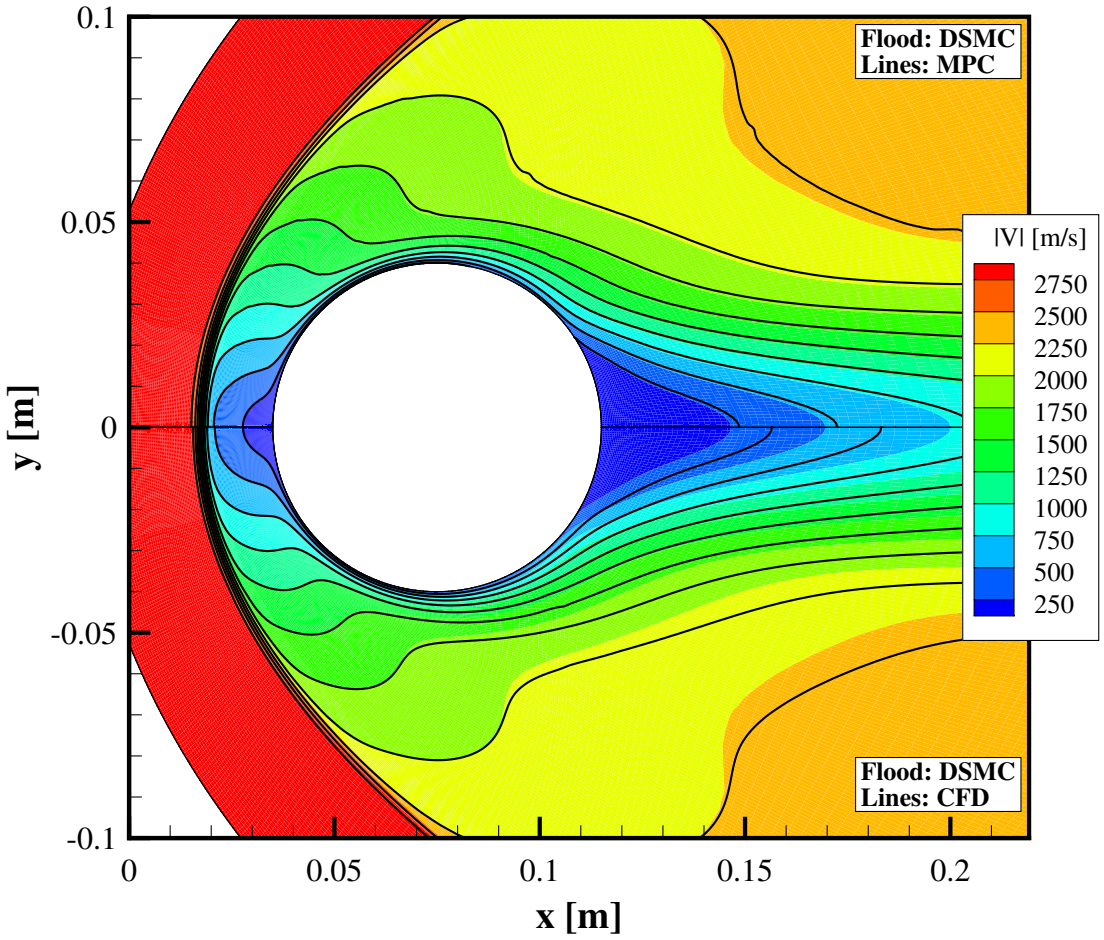

Figure 7.16: Contours of velocity magnitude for the Mach 10, Kn_∞ 0.01 flow of 80% N_2/20% O_2 over a two-dimensional cylinder.

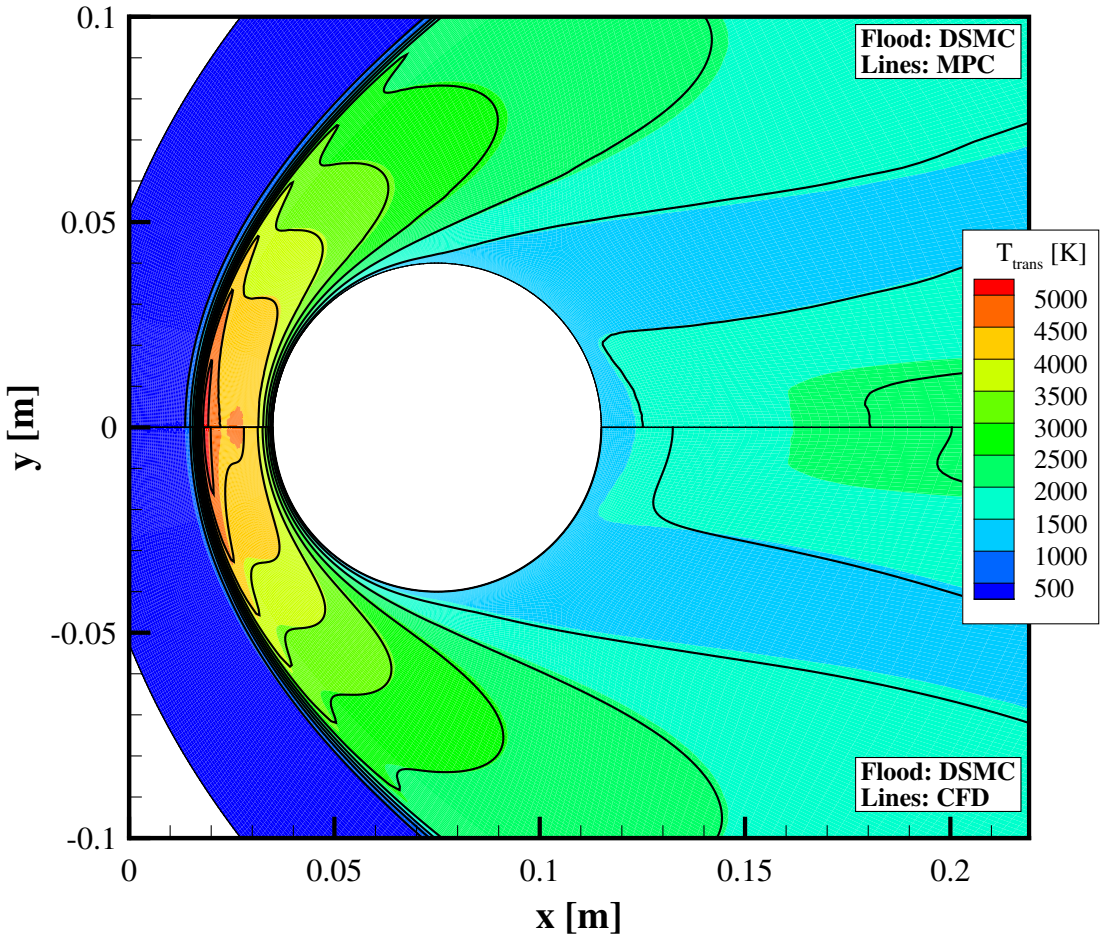

Figure 7.17: Contours of translational temperature for the Mach 10, Kn_∞ 0.01 flow of 80% N_2/20% O_2 over a two-dimensional cylinder.

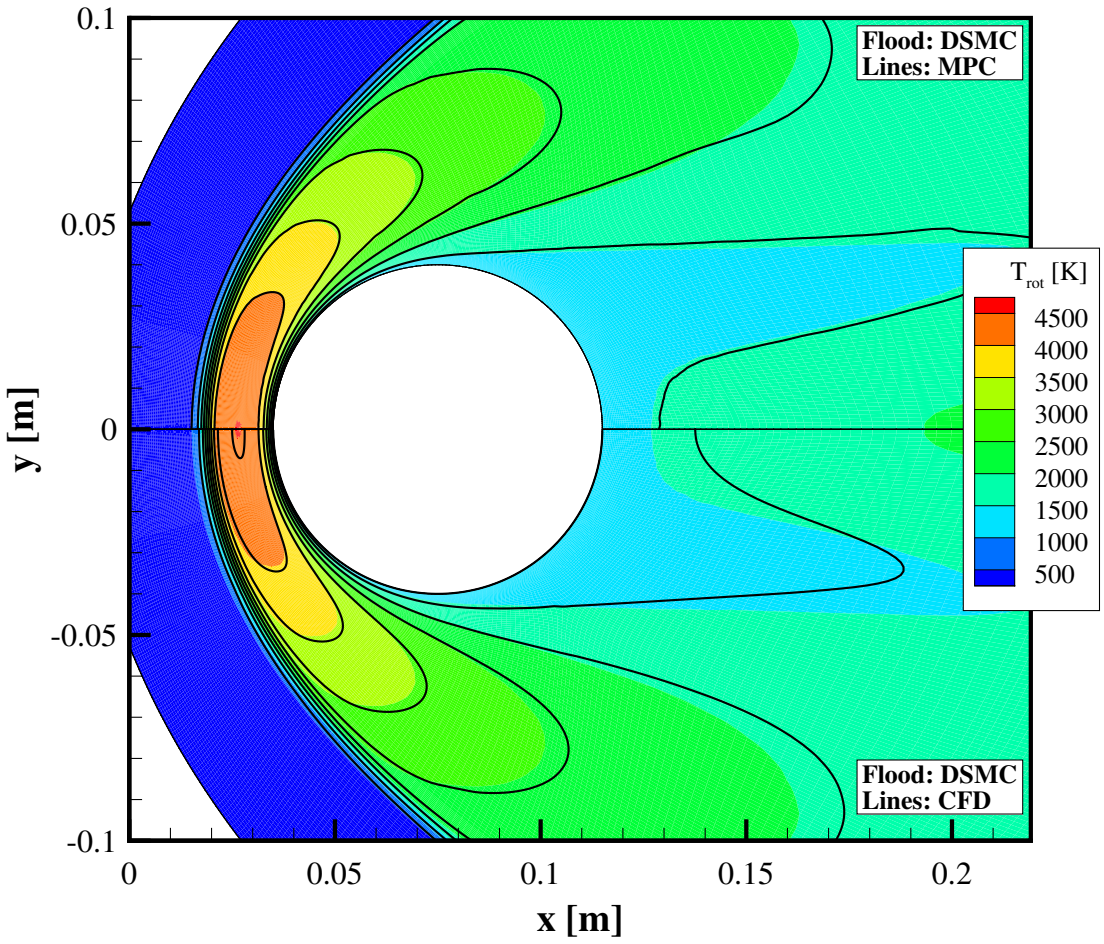

Figure 7.18: Contours of rotational temperature for the Mach 10, Kn_∞ 0.01 flow of 80% N_2/20% O_2 over a two-dimensional cylinder.

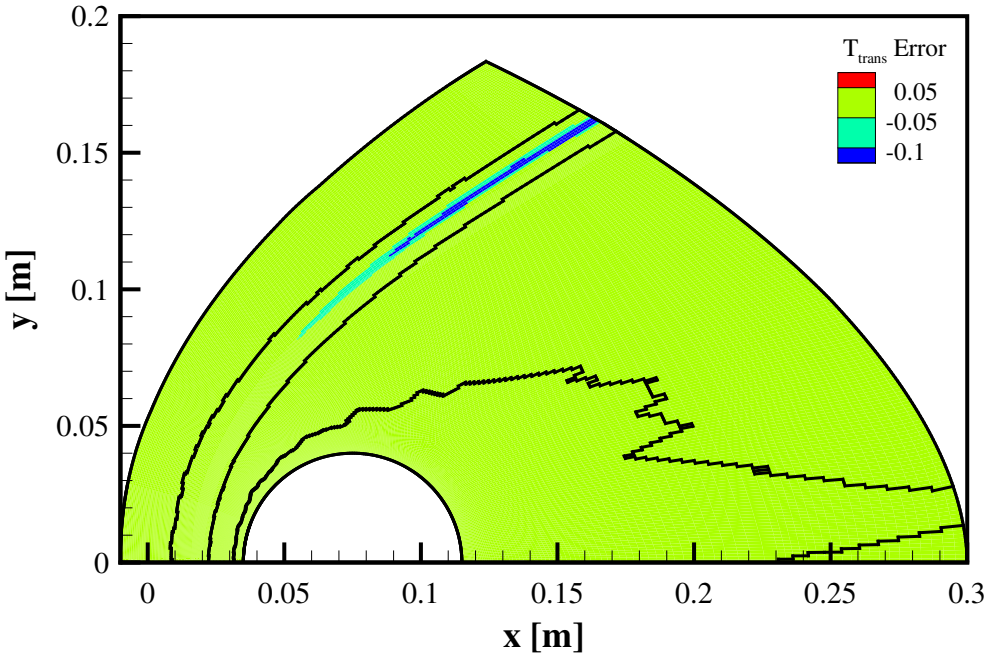

Figure 7.19: Contours of translational temperature errors of the MPC method relative to full DSMC for the Mach 10, Kn_∞ 0.01 flow of 80% N_2/20% O_2 over a two-dimensional cylinder; hybrid interfaces are shown as black lines.

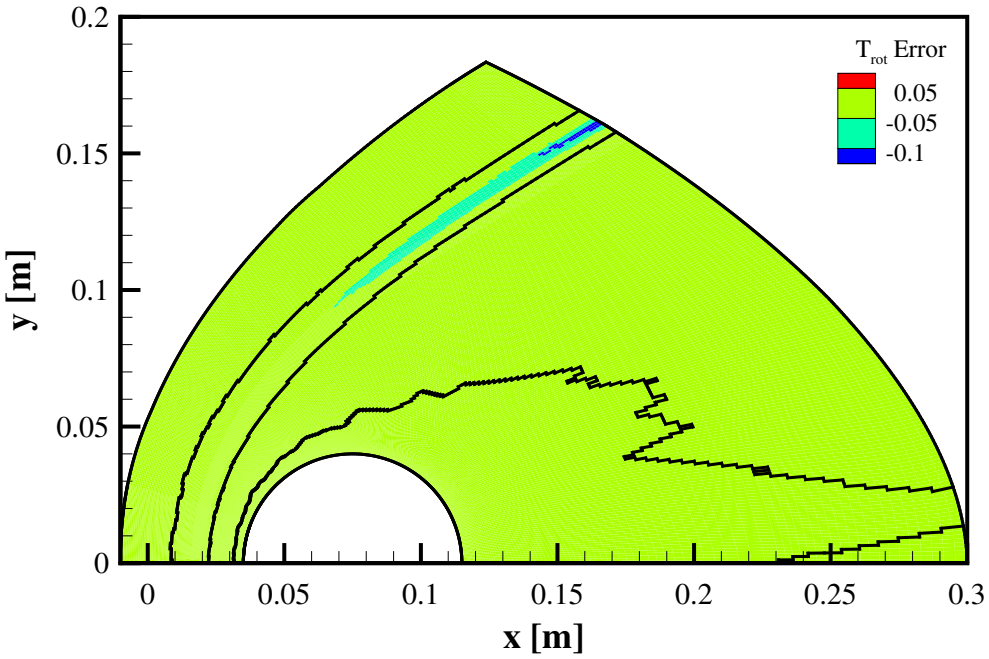

Figure 7.20: Contours of rotational temperature errors of the MPC method relative to full DSMC for the Mach 10, Kn_∞ 0.01 flow of 80% N_2/20% O_2 over a two-dimensional cylinder; hybrid interfaces are shown as black lines.

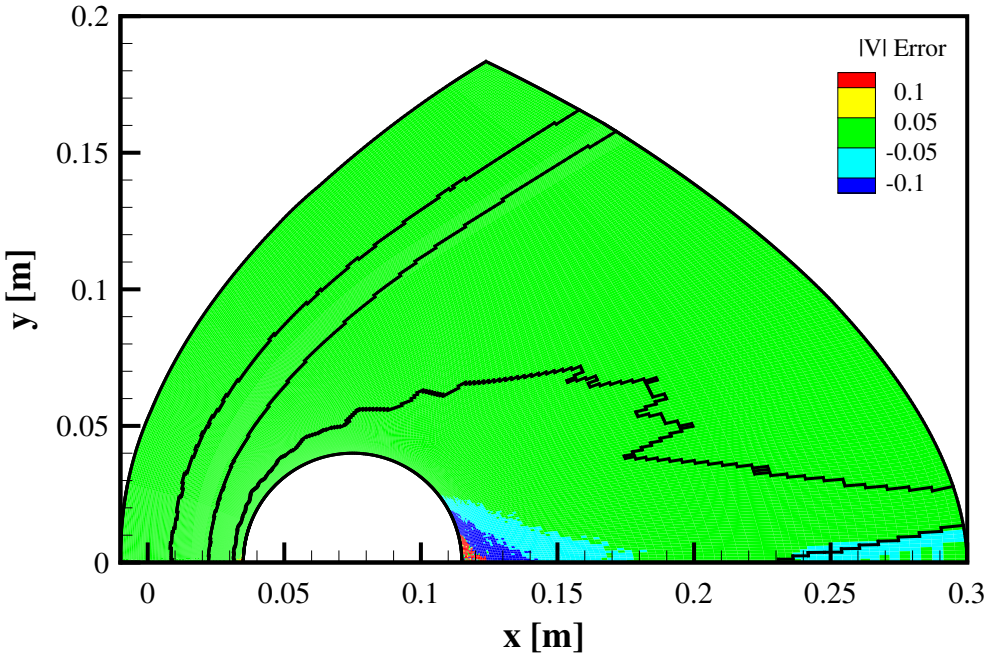

Figure 7.21: Contours of velocity magnitude errors of the MPC method relative to full DSMC for the Mach 10, Kn_∞ 0.01 flow of 80% N_2/20% O_2 over a two-dimensional cylinder; hybrid interfaces are shown as black lines.

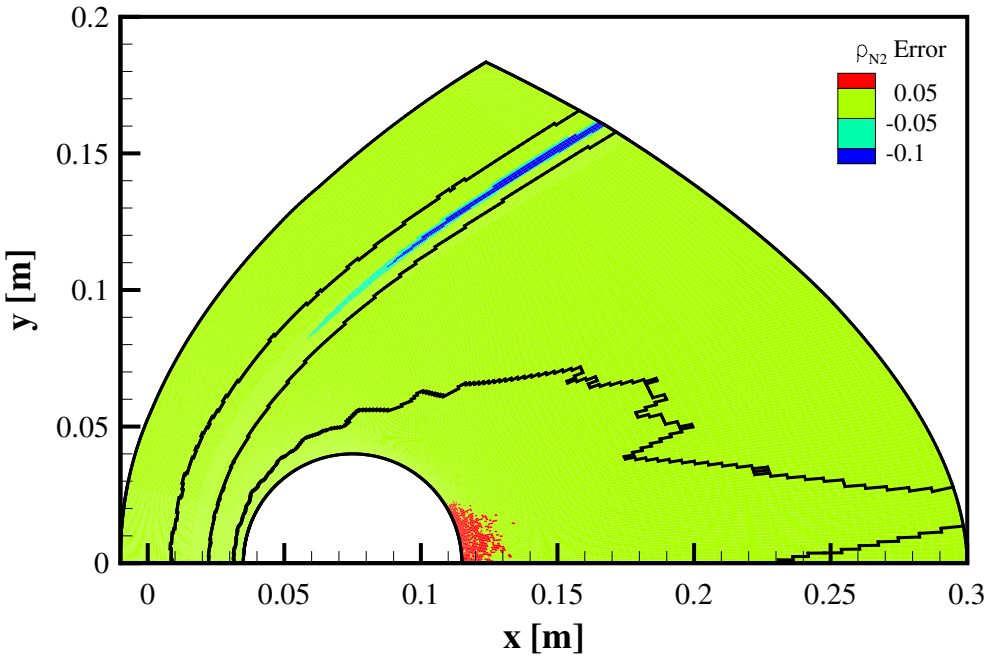

Figure 7.22: Contours of N_2 mass density errors of the MPC method relative to full DSMC for the Mach 10, Kn_∞ 0.01 flow of 80% N_2/20% O_2 over a two-dimensional cylinder; hybrid interfaces are shown as black lines.

Table 7.4: Ranges of errors relative to full DSMC for the Mach 10, Kn_∞ 0.01 flow of 80% N_2/20% O_2 over a two-dimensional cylinder.

Property	MPC Results	CFD Results
T_{trans}	$-0.14 \leq \epsilon \leq 0.04$	$-0.62 \leq \epsilon \leq 0.55$
T_{rot}	$-0.10 \leq \epsilon \leq 0.03$	$-0.63 \leq \epsilon \leq 0.07$
ρ_{N2}	$-0.20 \leq \epsilon \leq 0.08$	$-0.14 \leq \epsilon \leq 0.49$
ρ_N	$-0.20 \leq \epsilon \leq 0.10$	$-0.13 \leq \epsilon \leq 0.54$

Table 7.5: Relative errors measured in the L_2 norm for the Mach 10, Kn_∞ 0.01 flow of 80% N_2/20% O_2 over a two-dimensional cylinder.

Property	MPC Results	CFD Results
T_{trans}	0.011	0.042
T_{rot}	0.011	0.071
$\|V\|$	0.006	0.040
ρ_{N2}	0.012	0.082
ρ_N	0.012	0.064

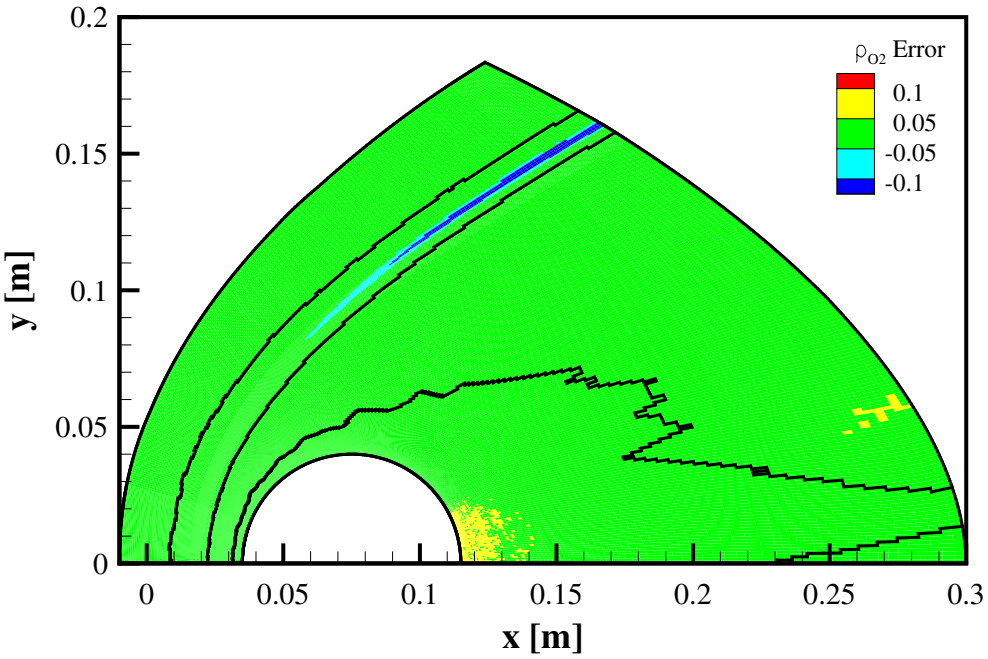

Figure 7.23: Contours of O_2 mass density errors of the MPC method relative to full DSMC for the Mach 10, Kn_∞ 0.01 flow of 80% N_2/20% O_2 over a two-dimensional cylinder; hybrid interfaces are shown as black lines.

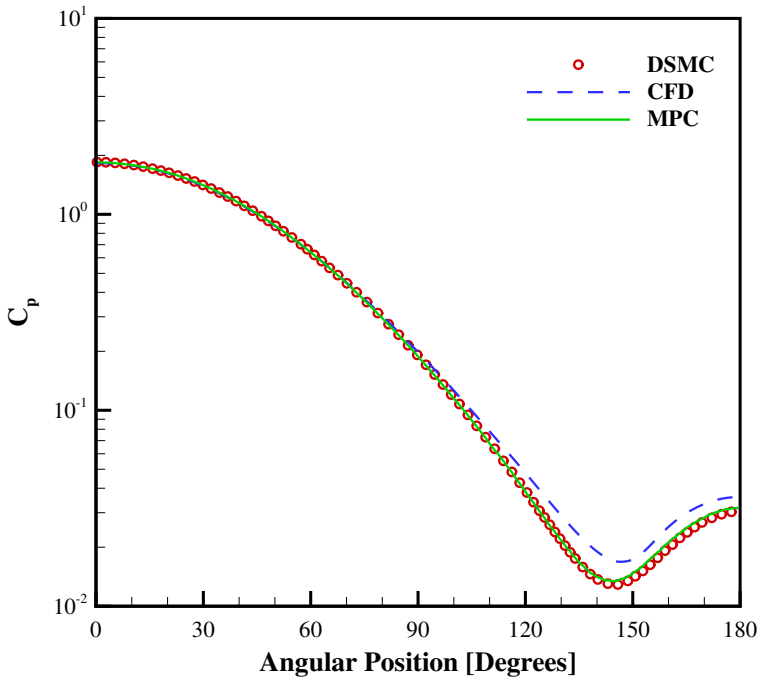

Figure 7.24: Surface pressure coefficient along the cylinder surface for the Mach 10, Kn_∞ 0.01 flow of 80% N_2/20% O_2.

7.3.2 Surface Properties

The surface pressure, heat transfer, and shear stress coefficients as calculated using CFD, DSMC, and the MPC hybrid method are plotted in Figs. 7.24 through 7.26. These results render conclusions that are very similar to those discussed regarding the 50% N_2/50% N gas mixture. A slightly higher level of error is observed between the MPC and DSMC profiles of the surface pressure coefficient, with a maximum error of approximately 7.4%. Likewise, the maximum error between the profiles of heat transfer coefficient is approximately 6.2%. The errors between the profiles of shear stress coefficient are within the original goal of ±5% between the angular positions of 15° and 149°, with the statistical scatter of the DSMC simulation obscuring the level of error near the fore stagnation point and in the wake.

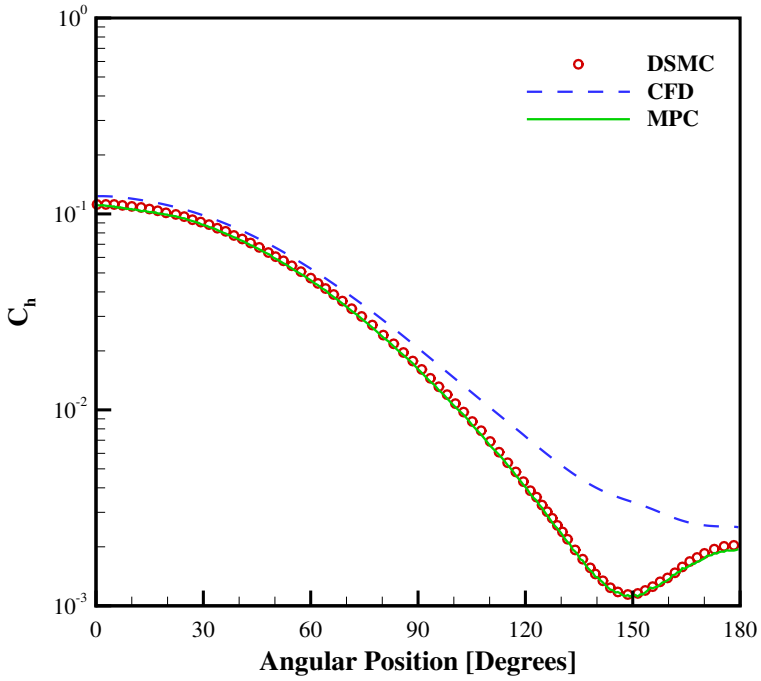

Figure 7.25: Heat transfer coefficient along the cylinder surface for the Mach 10, Kn_∞ 0.01 flow of 80% N_2/20% O_2.

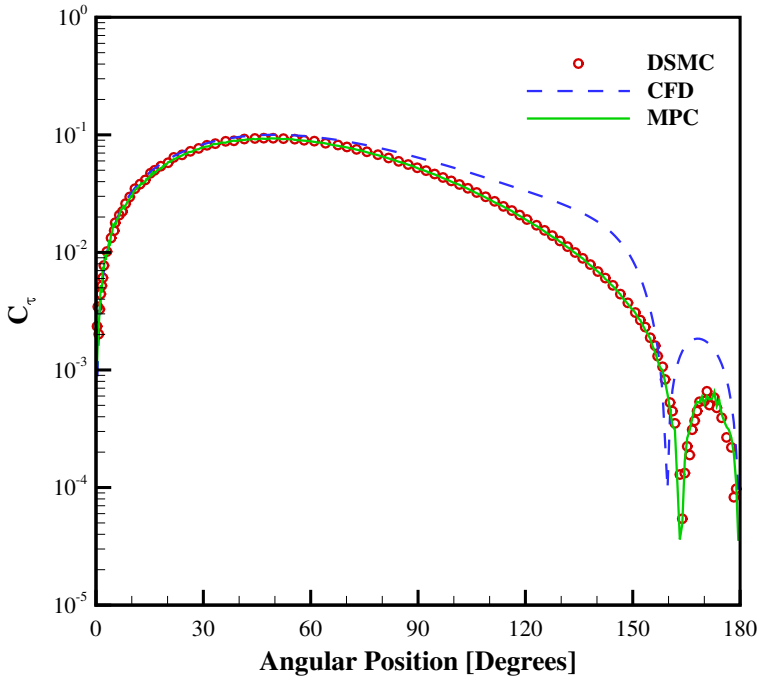

Figure 7.26: Shear stress coefficient along the cylinder surface for the Mach 10, Kn_∞ 0.01 flow of 80% N_2/20% O_2.

7.3.3 Computational Performance

By employing the more computationally involved DSMC method only where necessary to maintain physical accuracy, the MPC method is able to simulate this flow field using 17.9 million particles, whereas a full DSMC simulation requires 42.0 million particles. Therefore, an ideal speedup factor of 2.35 can be achieved. Upon comparing total computational times, it can be shown that the actual speedup factor is 2.22, which is slightly less than the ideal, despite the fact that each processor is assigned the same approximate number of particles in each simulation. However, this difference is of the order of the variation observed for repeated simulations, as discussed in Section 6.3.3. The MPC method also requires approximately 37% less memory than a full DSMC simulation.

Table 7.6: Computational performance statistics for the Mach 10, Kn_∞ 0.01 flow of 80% N_2/20% O_2 over a two-dimensional cylinder.

	CFD	**DSMC**	**MPC**
Normalized CPU Time	1.0	18.6	8.36
Normalized Memory	1.0	15.3	9.64
# Particles	-	42.0×10^6	17.9×10^6
# Continuum Cells	41,122	-	20,668
# Particle Cells	-	52,912	28,601
# Processors	4	38	16
Sampling/Total DSMC Steps	-	100,000/180,000	100,000/103,030

7.4 A Challenge for the MPC Method: 50% N_2/50% H

The largest difference between the molecular weights of constituent species in the gas mixtures analyzed thus far has been a factor of two. A gas mixture comprised of species with more disparate molecular weights presents an interesting challenge for the MPC method. To illustrate this, the case of a Mach 10, Kn_∞ 0.002 flow of 50% N_2/50% H (by mole) over a two-dimensional cylinder is examined. Note the lower Knudsen number of this case relative to the previous simulations. As

mentioned in Chapter III, the MPC method is meant to provide a correction to an initial continuum solution. The bow shock wave formed in this flow is extremely diffuse, and a CFD solution provides a very poor approximation to the full DSMC solution. Reducing the Knudsen number improves the agreement between the full CFD and full DSMC solutions, facilitating the ability of the MPC method to bridge the difference.

Because of the small molecular weight of atomic hydrogen, and the resulting large molecular velocities of the simulator particles representing these atoms, the mean collision time is greatly reduced compared to the previous simulations. The DSMC time step is now required to be $1 \times 10^{-9}s$ for the decoupled advection and collision steps in the DSMC method to be valid. Such a small time step, in turn, leads to a longer transient period that must be simulated prior to sampling particle properties. For example, since 80,000 time steps were required before sampling in the previous full DSMC simulations, where a time step of $1 \times 10^{-8}s$ was used, the current simulation requires approximately 800,000 time steps prior to sampling. The very slow development of this flow field poses particular difficulty for the MPC method, which relies on changes in the flow field to determine when the hybrid interfaces should be locked.

Furthermore, with the continuum breakdown parameters defined as in Eq. 6.5, the shock wave is automatically encompassed in a particle region, but the particle region surrounding the boundary layer does not form until some distance away from the stagnation point. Therefore, even the new Kn_{rot} parameter with a threshold value of 0.2 fails to predict the onset of nonequilibrium in the boundary layer of this flow field. Even with extended particle regions surrounding the shock wave and boundary layer, which is enabled by reducing the threshold value of the Kn_{rot} parameter, the MPC method has limited success in reproducing full DSMC simulation results. Figure 7.27 shows the translational temperature profiles along the stagnation streamline

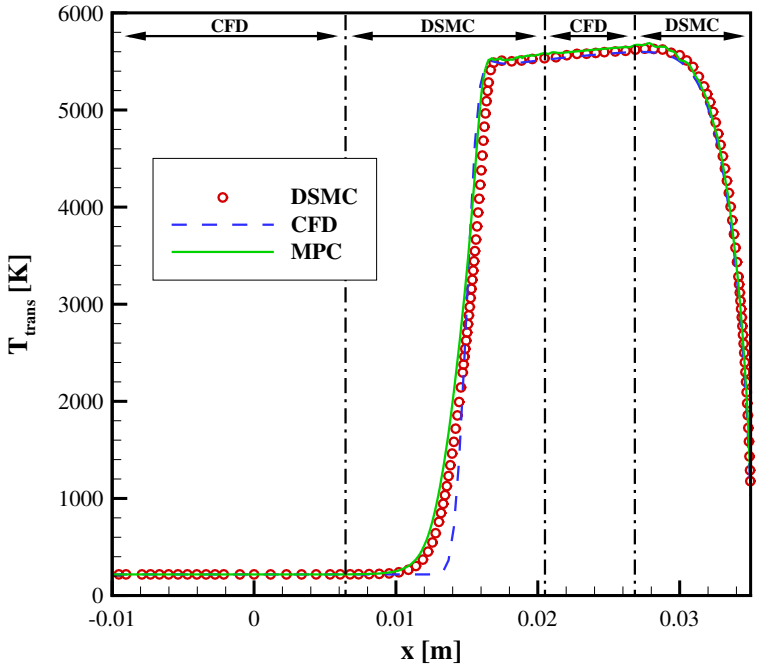

Figure 7.27: Translational temperature along the stagnation streamline for the Mach 10, Kn_∞ 0.002 flow of 50% N_2/50% H.

as predicted by full CFD, full DSMC, and MPC hybrid simulations, while Fig. 7.28 shows the rotational temperature profiles. Relative to the agreement in the translational and rotational temperature profiles exhibited in Figure 6.18 of Chapter VI, and knowing that the errors for the 50% N_2/50% N mixture are comparable, the current level of disagreement is quite high.

Perhaps the most compelling evidence that this particular mixture is problematic for the MPC method is provided by the surface properties plotted in Figs. 7.29 through 7.31. Even though it is apparent that more samples are needed to resolve these surface properties, the heightened level of disagreement between the MPC method and full DSMC is clear. The hybrid interfaces are automatically locked after 5,050 DSMC time steps, but it is estimated that an MPC simulation would have to be forced to run much longer in order to achieve improved physical accuracy relative to full DSMC results.

This simulation demonstrates the potential limitations of the automated MPC

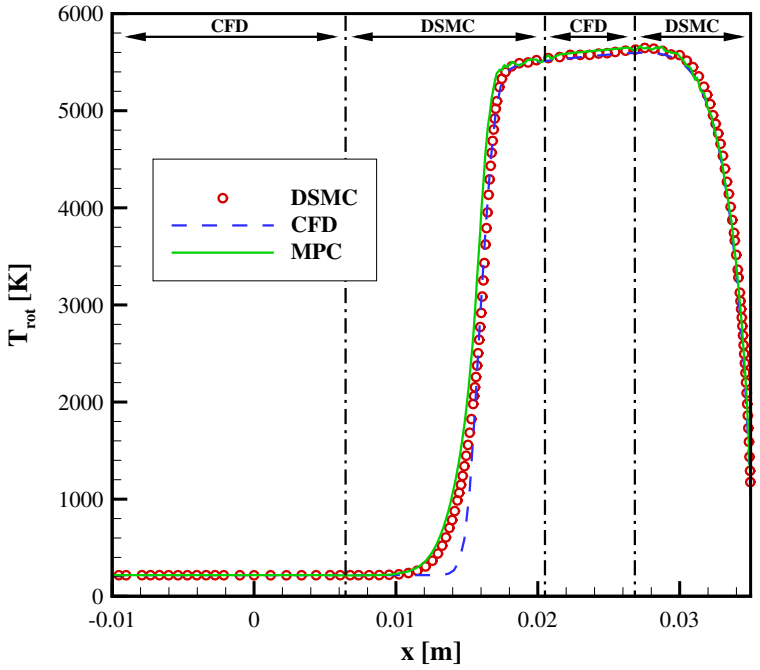

Figure 7.28: Rotational temperature along the stagnation streamline for the Mach 10, Kn_∞ 0.002 flow of 50% N_2/50% H.

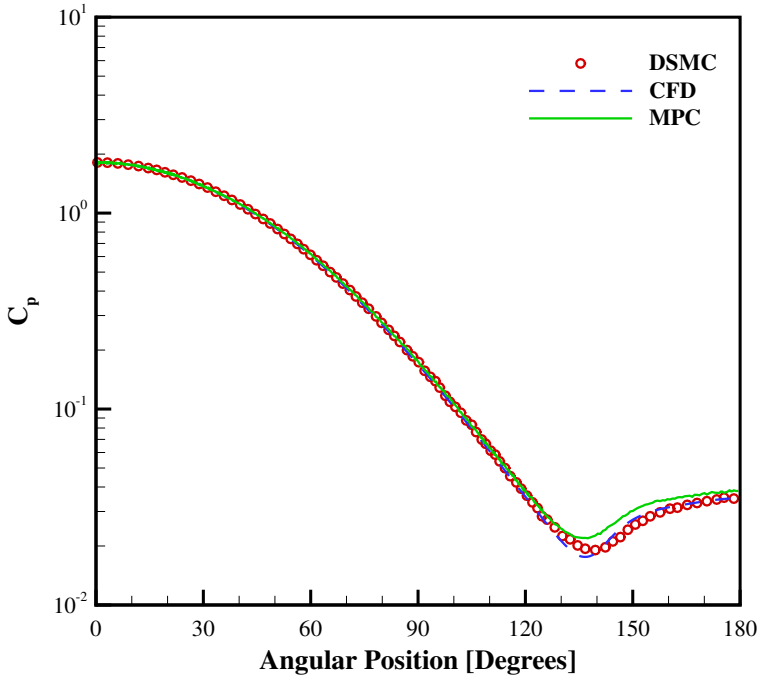

Figure 7.29: Surface pressure coefficient along the cylinder surface for the Mach 10, Kn_∞ 0.002 flow of 50% N_2/50% H.

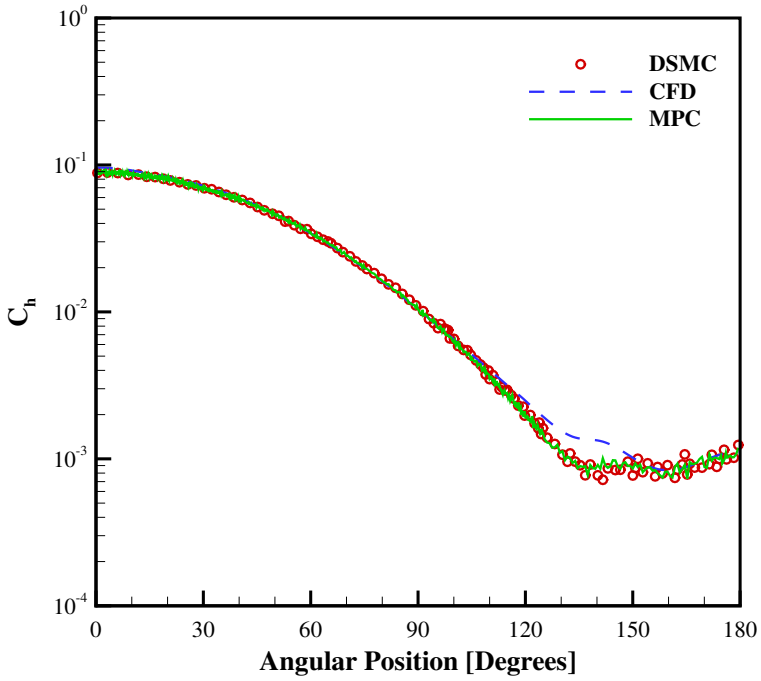

Figure 7.30: Heat transfer coefficient along the cylinder surface for the Mach 10, Kn_∞ 0.002 flow of 50% N_2/50% H.

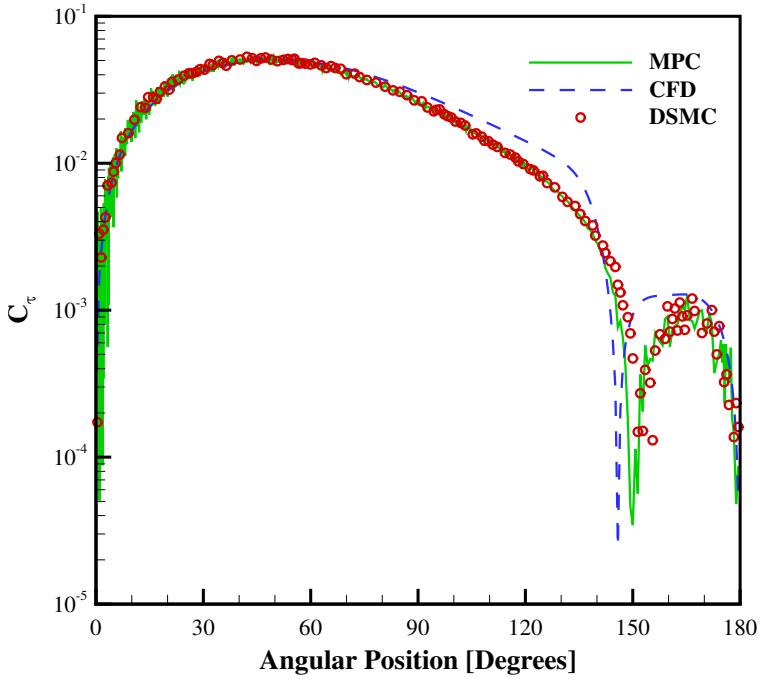

Figure 7.31: Shear stress coefficient along the cylinder surface for the Mach 10, Kn_∞ 0.002 flow of 50% N_2/20% H.

algorithm in a subset of transitional, hypersonic flows. Future simulations of five-species air mixtures comprised of N_2, O_2, NO, N, and O should not pose such difficulties, since the molecular weights of the constituent species are not nearly as disparate as in this test case. However, more advanced chemical mechanisms for Earth's atmosphere will include electrons, and atmospheric models for other planets include species with more widely varying molecular weights, so these obstacles will need to be overcome for the long-term development goals of the MPC hybrid method to be achieved.

7.5 Interim Conclusions

The MPC method was used to simulate three different gas mixtures in this chapter, with each case demonstrating either additional capabilities or potential limitations of the hybrid approach. First, the MPC method was shown to reproduce full DSMC results for a Mach 10, Kn_∞ 0.01 flow of 50% N_2/50% N (by mole) over a two-dimensional cylinder. The maximum error exhibited in any macroscopic fluid property of interest throughout the entire flow field was approximately 11%, which is consistent with the level of error observed in the simple gas case of the previous chapter. Discrepancies in the rotational temperature, however, suggest that either the hybrid interfaces may have been locked prematurely, or the more rigorous generalized Chapman-Enskog distribution may be necessary when assigning rotational energies to newly generated particles along hybrid interfaces. Neglecting the fore stagnation point and wake region where statistical scatter is especially problematic, the surface properties predicted by the MPC method and those obtained from the corresponding full DSMC simulation differed by less than $\pm$5%. These hybrid results were obtained with a speedup factor that exceeded the ideal estimate based on the number of simulator particles, and required a fraction of the memory necessary for a full DSMC simulation.

The second simulation was quite similar except the gas mixture was comprised of 80% N_2/20% O_2 (by mole), and each species was allowed to undergo rotational relaxation independently of the other. This represents a necessary step towards being able to accurately and efficiently simulate atmospheric flows with the MPC method. Although higher errors were observed for this case, results indicate that these errors could be reduced if a larger number of simulator particles were used. A final simulation of the Mach 10, Kn_∞ 0.002 flow of 50% N_2/50% H (by mole) over a two-dimensional cylinder was performed, and highlighted a potential limitation of the automated MPC algorithm. In particular, a flow field that develops on a much longer time scale than can be detected by the automated algorithm may prove difficult for the MPC method to simulate accurately. This was also proposed as a possible cause for errors in the wake regions of previous simulations, where the low collisionality of the flow may result in the hybrid method prematurely locking the hybrid interfaces.

CHAPTER VIII

Conclusion

In this final chapter, the results and conclusions that have been presented are further summarized, and the implications of this work are discussed. The unique contributions made towards the ongoing development of a hybrid particle-continuum method for simulating transitional, hypersonic flows over blunt-body, re-entry vehicles are emphasized, and several areas where future research efforts should be focused are also proposed.

8.1 Summary of Dissertation

Chapter I provided a brief introduction to the complex, multiscale nature of transitional, hypersonic, re-entry flows, and motivated the development of hybrid numerical simulation approaches. The Knudsen and Damköhler numbers were shown to characterize the relative importance of microscopic length and time scales in these flows, indicating whether the assumption of a continuum is warranted, or if the molecular nature of the gas must be considered. Both translational and thermal nonequilibrium phenomena were introduced, along with their association with hallmark features of re-entry flows, such as the strong bow shock wave, boundary and shear layers, and low-density wake. The last several decades of spaceflight have ushered in a deeper understanding of hypersonic aerothermodynamics, and advances in computational

resources have enabled higher-fidelity mathematical modeling of the re-entry environment. However, the mixed rarefied/continuum nature of transitional, hypersonic flows presents a formidable challenge to even the most well developed simulation techniques, such as the numerical solution of the Navier-Stokes equations using CFD and the DSMC method. In terms of both physical accuracy and numerical efficiency, hybrid simulation approaches provide many advantages over either CFD or DSMC alone.

In Chapter II, an overview of the mathematical models and numerical simulation techniques used to analyze transitional, hypersonic flows was provided. Beginning with a description of dilute gases that is grounded in kinetic theory, the Boltzmann equation was introduced. The Boltzmann equation provided the foundation for deriving the Euler equations of mass, momentum, and energy conservation for a continuum flow in thermodynamic equilibrium. The Navier-Stokes equations were also derived by assuming the distribution of molecular properties is a first-order perturbation of the equilibrium distribution function. Inherent to this derivation is the assumption that mass diffusion, viscosity, and heat conduction are linear functions of density, velocity, and temperature gradients in the flow field. Because of the difficulties associated with numerical solution of the Boltzmann equation, especially for mixtures of polyatomic species, and the physical limitations of the Navier-Stokes equations, a number of alternative simulation approaches were also discussed. The DSMC method was presented as the method of choice for obtaining flow field solutions that converge to those of the Boltzmann equation. The last section of this chapter provided a review of the published work regarding hybrid computational approaches, which offer the benefit of physical accuracy and numerical efficiency.

Chapter III focused on describing the MPC method, a hybrid framework that loosely couples two existing CFD and DSMC simulation codes. The current capabilities of LeMANS, a finite volume CFD solver, and MONACO, a general cell-based

implementation of the DSMC method, were discussed, along with the recent development of the MPC method. A detailed description of the hybrid algorithm was presented. This included the means by which regions of thermodynamic nonequilibrium are identified from an initial continuum solution, and the subsequent refinement of the coarse, continuum mesh to comply with DSMC cell-size requirements in particle regions. In addition, the mechanisms used to transfer updated solution information across hybrid interfaces, between the continuum and particle simulation modules, were discussed. Specifically, the procedures used to sample DSMC particle properties from distribution functions defined by macroscopic properties and, thus, provide continuum solution information to the particle domains, were detailed. The various equations needed to calculate macroscopic fluid properties from these simulator particles were also provided, which enables updated boundary solution information from the particle regions to be transferred back to the continuum domains. Finally, the modular organization of the CFD, DSMC, and hybrid functions and data structures was illustrated, and the previously described steps of the hybrid algorithm were assembled in a description of a typical hybrid cycle and complete MPC simulation.

The mathematical models used to simulate various physical processes, such as transport phenomena and thermal relaxation, were discussed in Chapter IV. Particular emphasis was placed on the consistency of these physical models in near-equilibrium flows. Assuming the hybrid interfaces are placed in near-equilibrium regions of a flow field, where both CFD and DSMC are physically appropriate simulation techniques, the physical models used in each approach should predict the same flow field solution in these regions. By verifying that these physical models are consistent, through simplified Couette flow and heat bath simulations, it is known that information is being consistently exchanged across these hybrid interfaces. Therefore, any differences between full CFD, full DSMC, and hybrid simulation results must be due to the limitations of the numerical approaches themselves and not inaccurate

information exchange. In this chapter, pertinent physical models were verified to be consistent for both simple gases and mixtures of chemical species.

A detailed and consistent evaluation of the physical accuracy of the MPC method relative to full DSMC was presented in Chapter V. A mapping procedure that introduces no interpolation errors, yet allows for different computational meshes to be used by MPC and DSMC simulations enables cell-by-cell comparisons of macroscopic fluid properties of interest. In this way, both the magnitude and location of errors incurred by using the hybrid approach are known, leading to deeper insight into what challenges remain for the continued development of the MPC method. A previously simulated test case was revisited for this investigation, which involves the Mach 12 flow of N_2 over a two-dimensional cylinder at a global Knudsen number of 0.01. This more detailed approach to accuracy quantification revealed errors that were much higher than reported in earlier publications, and the locations of these errors suggested a number of improvements that were then implemented. Specifically, the vacuum outflow boundary condition employed in the particle regions of hybrid simulations and in full DSMC simulations was replaced by a supersonic boundary condition that is consistent with that used in the continuum approach. In addition, attempts were made to improve the definition of macroscopic properties along hybrid interfaces, where differences in mesh refinement may lead to a loss of information. This enabled newly generated DSMC simulator particles to be assigned properties that are more consistent with those that would naturally occur in a full DSMC simulation. A reduction in flow field errors was observed after these changes were implemented, and this level of error was contextualized by quantifying the statistical scatter of the corresponding full DSMC simulation. Additional causes for the remaining errors were also investigated.

In Chapter VI, a new parameter for detecting rotational nonequilibrium effects was proposed. As was done for the gradient-length local Knudsen number, which is

the primary tool for determining continuum breakdown in the MPC hybrid method, detailed comparisons of full DSMC and full CFD simulation results for two test cases were performed. The first case was that of a Mach 12, Kn_∞ 0.01 flow of N_2 over a two-dimensional cylinder, while the second case was very similar except that a Mach 10 flow of 50% N_2/50% N was simulated. The magnitudes of the various continuum breakdown parameters, including the new rotational nonequilibrium parameter and that used in previous MPC simulations, were then calculated from the full CFD solution. The efficacy of these parameters was determined by how well their magnitudes correlated with the errors between the full DSMC and full CFD solutions. This new rotational nonequilibrium parameter was found to position the post-shock hybrid interfaces in these flows at the same approximate locations as the original parameter; failure of the gradient-length local Knudsen number to accurately predict continuum breakdown in this region is the reason why an additional parameter was initially proposed. In addition, the new rotational nonequilibrium parameter was shown to position the pre-boundary layer hybrid interfaces conservatively upstream of the stagnation points, where the other continuum breakdown parameters failed. An MPC hybrid simulation of the simple gas test case was then performed, and results obtained using the original and new rotational nonequilibrium parameters were compared. The agreement between hybrid and full DSMC results, in terms of both flow field and surface properties, was greatly improved through the use of this new rotational nonequilibrium parameter. In addition, the hybrid method achieved reductions in both computational time and memory usage relative to the corresponding full DSMC simulation.

Extension of the MPC method to include mixtures of chemical species was discussed and verified in Chapter VII. Additional considerations for accurately simulating gas mixtures using a hybrid approach were reviewed, including continuum breakdown detection and generation of DSMC simulator particles along hybrid in-

terfaces. Because of the simplifying assumptions made for these initial simulations involving gas mixtures, and additional findings published in the literature, very few changes to the hybrid algorithm were needed. The MPC method was first used to simulate the Mach 10, Kn_∞ 0.01 flow of 50% N_2/50% N over a two-dimensional cylinder, which is the same mixture test case examined in Chapter VI. The maximum error in any macroscopic property throughout the entire flow field was calculated to be 11%, while errors in surface properties were, for the most part, limited to ±5%. The MPC method was also shown to accurately predict the variation of mixture composition through the bow shock wave and in the boundary layer. A higher than ideal speedup factor was observed when computational times required by the MPC method and full DSMC were compared.

The particle selection methodology that allows for multiple polyatomic species to experience rotational relaxation independently was also verified by simulating a Mach 10, Kn_∞ 0.01 flow of 80% N_2/20% O_2 over a two-dimensional cylinder. Although the errors between MPC and full DSMC results were generally higher than in the previous simulation, it is believed that these errors could be reduced by using more DSMC particles to represent the lower concentration of O_2 in this mixture. Finally, a mixture comprised of species with widely disparate molecular weights was simulated using the MPC method. The Mach 10, Kn_∞ 0.002 flow of 50% N_2/50% H over a two-dimensional cylinder proved to be a challenge for the MPC method because of the much longer time required for this flow field to fully develop. Although this should not be problematic for future simulations of a five-species air mixture, for example, an appropriate solution will have to be determined for more complex air chemistry mechanisms.

8.2 Unique Contributions

As discussed in Chapter III, the MPC hybrid method was first developed by Schwartzentruber [64], and was shown to yield physically accurate results at a reduced computational cost for one-dimensional shock waves [65], two-dimensional and axisymmetric, steady, hypersonic blunt-body flows [66, 68], and shock-boundary layer interaction flows [67]. This initial demonstration of the loosely-coupled hybrid framework was limited to simple gases. Deschenes [19] later extended the capabilities of the MPC method to simple gases in rotational and vibrational nonequilibrium [21, 22]. The MPC algorithm was also parallelized to enable efficient simulation of more complicated physics and larger computational domains [20]. Building from these existing capabilities, this dissertation provides several unique contributions towards the ongoing development of the MPC hybrid method and its ability to simulate realistic atmospheric flows in an automated, numerically efficient, and physically accurate manner. A summary of these contributions and their implications is provided in this section, and additional details are provided in Refs. [79, 80, 81].

1. For the first time, a comprehensive assessment of the physical accuracy of the MPC hybrid method has been performed. Previous accuracy verification studies have been limited to comparisons between hybrid and full DSMC results along streamlines and other flow field extraction lines only. In this dissertation, hybrid and full DSMC results are quantitatively compared on a cell-by-cell basis without relying on interpolation procedures. As a result, both the magnitudes and locations of errors are known throughout the entire simulation domain. This enables a deeper level of understanding in terms of the causes of existing errors and potential improvements that should be made to the MPC method. These existing errors were also contextualized by quantifying the level of statistical scatter in a corresponding DSMC simulation, resulting in the conclusion that

the original accuracy objective of ±5% is unreasonable for typical simulations.

2. A commercial memory profiling software has been vetted in this dissertation, and provides a more accurate and detailed measure of the computational requirements of *parallel* MPC simulations. Profiling of the MPC code has also given insight into specific functions and subroutines that may impede further improvements in computational efficiency.

3. Improvements in the physical accuracy of the MPC method relative to full DSMC were achieved by implementing more consistent boundary conditions along the outflow boundary of the computational domain and hybrid interfaces. Most directly related to the ongoing development of hybrid particle-continuum methods, it was observed that differences in grid refinement along the hybrid interfaces contributes to a loss of information when newly generated simulator particles are generated from macroscopic fluid properties. By utilizing the gradients in these macroscopic fluid properties, better estimates of both particle properties and their positions can be obtained. Further investigation into the consistent exchange of information across hybrid interfaces also revealed that the transient nature of the DSMC method, especially in regions where the flow field develops more slowly, may lead to premature locking of the hybrid interfaces and inaccurate results.

4. The ability of the MPC hybrid method to *automatically* identify regions of thermodynamic nonequilibrium throughout the course of a simulation was also improved by the work presented in this dissertation. A new parameter for identifying rotational nonequilibrium effects was proposed and found to offer advantages over the gradient-length local Knudsen number and the previously employed rotational nonequilibrium parameter. Prior to this investigation, it was commonplace for these continuum breakdown parameters to fail to pre-

dict an adequately thick particle region surrounding the boundary layers of transitional, hypersonic, blunt-body flows. This new rotational nonequilibrium parameter was shown to obviate the need for human intervention in the MPC algorithm for a simple gas and two different gas mixtures.

5. This dissertation research enabled the accurate simulation of gas mixtures using the MPC method. Particle and continuum models for transport properties and thermal nonequilibrium were verified to be consistent for simple gases and gas mixtures. Specifically, a simple approach to calculating VHS collision model parameters that are consistent with the Gupta Mixing Rule in CFD was proposed, and was verified to give results that are comparable to those obtained using a more rigorous approach. Improved agreement between translational-rotational energy exchange models was obtained for both simple gases and gas mixtures through detailed heat bath simulations. To achieve consistent vibrational relaxation rates between CFD and DSMC when simulating gas mixtures, a new "mixture rule" was used in the continuum approach that is unlike others proposed in the literature.

6. The MPC method is now able to accommodate more realistic atmospheric flows in which multiple species are in rotational nonequilibrium and equilibrate at different rates. A particle selection methodology for calculating translational-rotational energy exchange probabilities was implemented and shown to yield relaxation rates that are consistent with the continuum approach.

7. This dissertation discussed the challenges of simulating gas mixtures comprised of species with widely disparate molecular weights. Simulated flow fields that develop on much longer time scales than were previously considered pose difficulties for the automatic detection of steady state in a hybrid simulation.

8.3 Future Work

The current capabilities of the MPC hybrid method enable the physically accurate and numerically efficient simulation of a large class of transitional, hypersonic flows over simple blunt bodies. However, continued research efforts are required to further develop the physical and chemical modeling capabilities, algorithm robustness, and general applicability of the method to more complex hypersonic vehicles of engineering interest. These recommended areas of future work are described in more detail in this section.

8.3.1 VSS Collision Model

In order to accurately simulate viscosity *and* mass diffusion effects in a gas mixture, the VSS collision model should be used in the DSMC method instead of the VHS collision model. The latter collision model was employed in these initial simulations of gas mixtures because the simple approach proposed in Chapter IV for determining collision parameters that are consistent with the Gupta Mixing Rule facilitated the calculation of only a reference diameter and temperature exponent for each collision class. The more rigorous Nelder-Mead simplex algorithm enables the minimization of functions of many independent variables, and provides a means to calculate a reference collision diameter, temperature exponent, and scattering parameter for each collision class in a gas mixture. Therefore, the capability already exists to perform MPC hybrid simulations of gas mixtures that account for all transport processes in a physically meaningful manner.

8.3.2 Generalized Chapman-Enskog Distribution

There is limited evidence to suggest that the mass diffusion and internal heat flux perturbation terms of the generalized Chapman-Enskog distribution are unimportant relative to other transport processes in transitional, hypersonic flows over blunt

bodies. In addition, when DSMC simulator particles are generated along hybrid interfaces in the MPC hybrid method, rotational energies are sampled from a Boltzmann equilibrium distribution. However, it is unclear how valid these approximations are until current MPC results are compared to those obtained when particle properties are sampled from the more rigorous generalized Chapman-Enskog distribution. Only after such a comparison is made can these approximations be eliminated as possible sources of the remaining errors between hybrid and full DSMC results. Of particular concern is the sudden disagreement between the contours of rotational temperature across the hybrid interfaces, as discussed in this dissertation. Also, when mass diffusion effects are accurately simulated through the use of the VSS collision model in particle domains, it will become even more important to determine the relative importance of the mass diffusion perturbation terms of the generalized Chapman-Enskog distribution throughout flow fields of interest.

8.3.3 Continuum Breakdown

One of the most challenging aspects of developing a hybrid particle-continuum method is the accurate and reliable prediction of continuum breakdown. Because one of the goals of the MPC method is to reduce the computational effort of obtaining physically accurate solutions of transitional, hypersonic flows, these measures of continuum breakdown are calculated from an initial continuum solution which is then improved throughout the course of the simulation. The downfall of such measures, however, is that a threshold value is required to distinguish computational cells that are in thermodynamic nonequilibrium from those that can be accurately simulated using CFD. Therefore, the generality of these continuum breakdown parameters and their associated threshold values is a concern. A more reliable mechanism for determining rotational nonequilibrium was proposed in this dissertation, but a deeper understanding of nonequilibrium phenomena and continuum breakdown is needed.

Until then, the efficacy of current measures of continuum breakdown should not be assumed in every situation. For example, even though a parameter for detecting vibrational nonequilibrium effects in the MPC method has already been proposed, a procedure similar to that presented in this dissertation for identifying rotational nonequilibrium effects should also be carried out.

8.3.4 Mesh Refinement Algorithm

Currently, the MPC method is able to accommodate structured computational meshes only, and does not allow for hanging nodes. This leads to more refinement in certain particle regions than is necessary to comply with DSMC cell-size requirements. Therefore, gains in efficiency may be achieved by allowing for hanging nodes in the computational mesh. Additional benefits could also be realized through more complex mesh refinement algorithms. For example, in a typical CFD simulation, the alignment of the computational mesh with the bow shock wave and boundary layer are essential because the numerical solution of the Navier-Stokes equations relies heavily on flow field gradients. Resolution of the viscous boundary layer also requires a very refined grid near simulated wall boundaries. A computational mesh that is optimized for a DSMC simulation will be quite different. Each cell is simply used for binning simulator particles for collision partner selection and calculating macroscopic averages. Use of an unstructured mesh is, thus, preferred because the grid generation process is greatly simplified without diminishing the accuracy of the simulation, as long as the computational cells are appropriately sized. Similar to the CFL condition in CFD, however, DSMC cells that are too small for a given time step can lead to a loss of accuracy; simulator particles do not spend enough time in these cells to obtain physically meaningful averages. This can easily happen when the current MPC algorithm is initialized with a continuum solution and corresponding mesh that is greatly refined to resolve the viscous boundary layer, for example. Through the use

of involved interpolation procedures, the particle and continuum regions of a hybrid simulation could employ computational meshes that are optimally suited for each approach. Such a complete separation of length scales between simulation domains is only advised after the basic hybrid algorithm is more thoroughly tested.

8.3.5 Chemical Reactions

In the case of high-enthalpy re-entry trajectories, chemical reactions among atmospheric species are expected to occur. Such chemical reactions, including dissociation of molecular species and ionization, may significantly alter the shock stand-off distance, heat loads, and aerodynamic forces on the vehicle, to name a few. Accurate simulation of chemical reactions is a long-term goal of the MPC hybrid method. Both the MONACO and LeMANS codes already account for atmospheric chemistry, but the *consistency* of these chemical models remains a formidable challenge for several reasons. For one, the interdependent nature of dissociative reactions, vibrational energy relaxation, and the temperatures that characterize each energy mode further complicates these already complex processes. In addition, chemical reactions usually introduce trace species which may require the use of species-based numerical weights in DSMC simulations; the effect of variable species-based and cell-based numerical weights on the statistics of the DSMC method is still an active area of research.

8.3.6 Three-Dimensional Geometries

The transitional, hypersonic flow over a two-dimensional cylinder provides a flow field that is rich in the same physics of a more realistic, blunt-body vehicle. However, to enable widespread use in the engineering community, the MPC method must be capable of simulating more complex, three-dimensional flows. Actual re-entry capsules, for example, even if they can be assumed axisymmetric, often fly at non-zero angles of attack and employ reaction control system thrusters or propulsive deceleration, so

that the three-dimensionality of the flow field cannot be ignored. The extension of the MPC method to include three-dimensional simulation domains becomes an issue of coding, since both MONACO and LeMANS already have this capability. Even larger improvements in computational savings are expected for the MPC method relative to full DSMC when three-dimensional simulations are performed because of the additional dimension. For example, neglecting any flow field gradients, if a single continuum cell must be refined to include two particle cells in one dimension to comply with the local mean free path, then the corresponding cell in a three-dimensional simulation will be comprised of eight particle cells, all of which must contain the required number of simulator particles.

APPENDIX

APPENDIX A

Physical Model Parameters

Table A.1: Variable Hard Sphere (VHS) collision model reference diameters, d_{ref} [Å].

	N_2	N	O_2	H
N_2	3.99	3.69	3.79	3.58
N	3.69	3.36	–	–
O_2	3.79	–	3.85	–
H	3.58	–	–	3.35

Table A.2: Variable Hard Sphere (VHS) collision model temperature exponents, ω.

	N_2	N	O_2	H
N_2	0.675	0.701	0.690	0.793
N	0.701	0.746	–	–
O_2	0.690	–	0.683	–
H	0.793	–	–	0.801

Table A.3: Molecular species constants.

	T^* $[K]$	$(Z_{rot})_\infty$	θ_{rot} $[K]$	θ_{vib} $[K]$
N_2	91.5	18.0	2.88	3395
O_2	113.5	16.5	2.07	2256

BIBLIOGRAPHY

BIBLIOGRAPHY

[1] Allinea, *Allinea DDT and MAP User Guide, Version 4.2.2*, 2014.

[2] Anderson, Jr., J. D., *Introduction to Flight*, McGraw-Hill, Inc., 1989.

[3] Anderson, Jr., J. D., *Fundamentals of Aerodynamics*, McGraw-Hill, Inc., 2007.

[4] Bergemann, F. and Boyd, I. D., "New Discrete Vibrational Energy Model for the Direct Simulation Monte Carlo Method," *Rarefied Gas Dynamics: Experimental Techniques and Physical Systems*, edited by Shizgal, B. D., and Weaver, D. P., Vol. 158, 1994, pp. 174–183.

[5] Bhatnagar, P. L., Gross, E. P., and Krook, M., "A Model for Collision Processes in Gases. I. Small Amplitude Processes in Charged and Neutral One-Component Systems," *Phys. Rev.*, Vol. 94, No. 3, May 1954, pp. 511–525.

[6] Bird, G. A., "Approach to Translational Equilibrium in a Rigid Sphere Gas," *Phys. Fluids*, Vol. 6, No. 10, October 1963, pp. 1518–1519.

[7] Bird, G. A., "Breakdown of Translational and Rotational Equilibrium in Gaseous Expansions," *AIAA J.*, Vol. 8, No. 11, November 1970, pp. 1998–2003.

[8] Bird, G. A., *Molecular Gas Dynamics and the Direct Simulation of Gas Flows*, Oxford University Press, 1994.

[9] Bird, R. B., Stewart, W. E., and Lightfoot, E. D., *Transport Phenomena*, John Wiley and Sons, 1960.

[10] Borgnakke, C. and Larsen, P. S., "Statistical Collision Model for Monte Carlo Simulation of Polyatomic Gas Mixture," *J. Comput. Phys.*, Vol. 18, No. 4, August 1975, pp. 405–420.

[11] Boyd, I. D., "Analysis of Rotational Nonequilibrium in Standing Shock Waves of Nitrogen," *AIAA J.*, Vol. 28, No. 11, November 1990, pp. 1997–1999.

[12] Boyd, I. D., "Rotational-Translational Energy Transfer in Rarefied Nonequilibrium Flows," *Phys. Fluids*, Vol. 2, No. 3, March 1990, pp. 447–452.

[13] Boyd, I. D., "Analysis of Vibrational-Translational Energy Transfer Using the Direct Simulation Monte Carlo Method," *Phys. Fluids*, Vol. 3, No. 7, July 1991, pp. 1785–1791.

[14] Boyd, I. D., Chen, G., and Candler, G. V., "Predicting Failure of the Continuum Fluid Equations in Transitional Hypersonic Flows," *Phys. Fluids*, Vol. 7, No. 1, January 1995, pp. 210–219.

[15] Camberos, J. A. and Chen, P.-H., "Continuum Breakdown Parameter Based on Entropy Generation Rates," *AIAA Paper 2003-0157*, January 2003, presented at the 41st AIAA Aerospace Sciences Meeting and Exhibit, Reno, NV.

[16] Chang, C. S. and Uhlenbeck, G. E., "Transport Phenomena in Polyatomic Gases," *Report No. CM-681*, July 1951, Engineering Research Institute, University of Michigan, Ann Arbor, MI.

[17] Chapman, S. and Cowling, T. G., *The Mathematical Theory of Non-Uniform Gases*, Cambridge University Press, 1939.

[18] Chen, G. and Boyd, I. D., "Statistical Error Analysis for the Direct Simulation Monte Carlo Technique," *J. Comput. Phys.*, Vol. 126, No. 2, July 1996, pp. 434–448.

[19] Deschenes, T. R., *Extension of a Modular Particle-Continuum Method for Nonequilibrium, Hypersonic Flows*, Ph.D. thesis, University of Michigan, 2011.

[20] Deschenes, T. R. and Boyd, I. D., "Parallelization of a Modular Particle-Continuum Method for Hypersonic, Near Equilibrium Flows," *AIAA Paper 2010-808*, January 2010, presented at the 48th AIAA Aerospace Sciences Meeting Including the New Horizons Forum and Aerospace Exposition, Orlando, FL.

[21] Deschenes, T. R. and Boyd, I. D., "Extension of a Modular Particle-Continuum Method to Vibrationally Excited, Hypersonic Flows," *AIAA J.*, Vol. 49, No. 9, September 2011.

[22] Deschenes, T. R., Holman, T. D., and Boyd, I. D., "Effects of Rotational Energy Relaxation in a Modular Particle-Continuum Method," *J. Thermophys. Heat Tr.*, Vol. 25, No. 2, April-June 2011.

[23] Dietrich, S. and Boyd, I. D., "Scalar and Parallel Optimized Implementation of the Direct Simulation Monte Carlo Method," *J. Comput. Phys.*, Vol. 126, No. 2, July 1996, pp. 328–342.

[24] Fallavollita, M. A., Baganoff, D., and McDonald, J. D., "Reduction of Simulation Cost and Error for Particle Simulations of Rarefied Flows," *J. Comput. Phys.*, Vol. 109, No. 1, November 1993, pp. 30–36.

[25] Fan, J. and Shen, C., "Statistical Simulation of Low-Speed Rarefied Gas Flows," *J. Comput. Phys.*, Vol. 167, No. 2, March 2001, pp. 393–412.

[26] Garcia, A. L. and Alder, B. J., "Generation of the Chapman-Enskog Distribution," *J. Comput. Phys.*, Vol. 140, No. 1, February 1998, pp. 66–70.

[27] Garcia, A. L., Bell, J. B., Crutchfield, W. Y., and Alder, B. J., "Adaptive Mesh and Algorithm Refinement using Direct Simulation Monte Carlo," *J. Comput. Phys.*, Vol. 154, No. 1, September 1999, pp. 134–155.

[28] Gimelshein, N. E., Gimelshein, S. F., and Levin, D. A., "Vibrational Relaxation Rates in the Direct Simulation Monte Carlo Method," *Phys. Fluids*, Vol. 14, No. 12, December 2002, pp. 4452–4455.

[29] Gnoffo, P. A., Gupta, R. N., and Shinn, J. L., "Conservation Equations and Physical Models for Hypersonic Air Flows in Thermal and Chemical Nonequilibrium," *NASA-TP-2867*, 1989.

[30] Golse, F., "Applications of the Boltzmann Equation Within the Context of Upper Atmosphere Vehicle Aerodynamics," *Comput. Method Appl. M.*, Vol. 75, 1989, pp. 299–316.

[31] Grad, H., "On the Kinetic Theory of Rarefied Gases," *Comm. Pure Appl. Math.*, Vol. 2, No. 4, 1949, pp. 331–407.

[32] Gupta, R. N., Yos, J. M., Thompson, R. A., and Lee, K. P., "A Review of Reaction Rates and Thermodynamic and Transport Properties for an 11-Species Air Model for Chemical and Thermal Nonequilibrium Caclulations to 30,000 K," *NASA-RP-1232*, 1990.

[33] Haas, B. L., Hash, D. B., Bird, G. A., Lumpkin, F. E., and Hassan, H. A., "Rates of Thermal Relaxation in Direct Simulation Monte Carlo Methods," *Phys. Fluids*, Vol. 6, No. 6, June 1994, pp. 2191–2201.

[34] Hadjiconstantinou, N. G., Garcia, A. L., Bazant, M. Z., and He, G., "Statistical Error in Particle Simulations of Hydrodynamic Phenomena," *J. Comput. Phys.*, Vol. 187, No. 1, May 2003, pp. 274–297.

[35] Hash, D. B. and Hassan, H. A., "Assessment of Schemes for Coupling Monte Carlo and Navier-Stokes Solution Methods," *J. Thermophys. Heat Tr.*, Vol. 10, No. 2, April-June 1996.

[36] Hash, D. B. and Hassan, H. A., "Two-Dimensional Coupling Issues of Hybrid DSMC/Navier-Stokes Solvers," *AIAA Paper 1997-2507*, 1997, presented at the 32nd AIAA Thermophysics Conference.

[37] Hirschfelder, J. O., Curtiss, C. F., and Bird, R. B., *Molecular Theory of Gases and Liquids*, John Wiley and Sons, 1954.

[38] Holman, T. D. and Boyd, I. D., "Effects of Continuum Breakdown on the Surface Properties of a Hypersonic Sphere," *J. Thermophys. Heat Tr.*, Vol. 23, No. 4, October-December 2009, pp. 660–673.

[39] Holman, T. D. and Boyd, I. D., "Effects of Continuum Breakdown on Hypersonic Aerothermodynamics for Reacting Flow," *Phys. Fluids*, Vol. 23, No. 2, February 2011, pp. 1–15.

[40] Incropera, F. P., *Introduction to Molecular Structure and Thermodynamics*, John Wiley and Sons, 1974.

[41] Jawahar, P. and Kamath, H., "A High-Resolution Procedure for Euler and Navier-Stokes Computations on Unstructured Grids," *J. Comput. Phys.*, Vol. 164, 2000, pp. 165–203.

[42] Jeans, J. H., *The Dynamical Theory of Cases*, Cambridge University Press, 1916.

[43] Karypis, G. and Kumar, V., "METIS: A Software Package for Partitioning Unstructured Graphs, Partitioning Meshes, and Computing Fill-Reducing Orderings of Sparse Matrices," University of Minnesota, MN, 1998.

[44] Landau, L. and Teller, E., "Zur theorie der schalldispersion," *Phys. Z. Sowjetunion*, Vol. 10, No. 14, 1936.

[45] Lee, J. H., "Basic Governing Equations for the Flight Regimes of Aeroassisted Orbital Transfer Vehicles," *AIAA Paper 1984-1729*, June 1984, presented at the 19th AIAA Thermophysics Conference, Snowmass, CO.

[46] Lofthouse, A. J., Boyd, I. D., and Wright, M. J., "Effects of Continuum Breakdown on Hypersonic Aerothermodynamics," *Phys. Fluids*, Vol. 19, No. 2, February 2007, pp. 1–12.

[47] Lofthouse, A. J., Scalabrin, L. C., and Boyd, I. D., "Velocity Slip and Temperature Jump in Hypersonic Aerothermodynamics," *J. Thermophys. Heat Tr.*, Vol. 22, No. 1, January-March 2008.

[48] Lumpkin, F. E., Haas, B. L., and Boyd, I. D., "Resolution of Differences Between Collision Number Definitions in Particle and Continuum Simulations," *Phys. Fluids*, Vol. 3, No. 9, 1991, pp. 2282–2284.

[49] MacCormack, R. W. and Candler, G. V., "The Solution of the Navier-Stokes Equations using Gauss-Seidel Line Relaxation," *Computers and Fluids*, Vol. 17, 1989, pp. 135–150.

[50] Martin, A., Scalabrin, L. C., and Boyd, I. D., "High Performance Modeling of Atmospheric Re-Entry Vehicles," *J. Phys.: Conf. Ser.*, Vol. 341, No. 012002, 2012.

[51] Millikan, R. C. and White, D. R., "Systematics of Vibrational Relaxation," *J. Chem. Phys.*, Vol. 39, No. 12, December 1963, pp. 3209–3213.

[52] Mott-Smith, H. M., "The Solution of the Boltzmann-Equation for a Shock Wave," *Phys. Rev.*, Vol. 82, No. 6, 1951, pp. 885–892.

[53] Nagnibeda, E. and Kustova, E., *Non-Equilibrium Reacting Gas Flows: Kinetic Theory of Transport and Relaxation Processes*, Springer-Verlag, Berlin, Germany, 2009.

[54] Nelder, J. A. and Mead, R., "A Simplex Method for Function Minimization," *Comput. J.*, Vol. 7, 1965, pp. 308–313.

[55] Palmer, G. E., Pulsonetti, M., Wood, W. A., Alter, S., Gnoffo, P., and Tang, C., "Computational Assessment of Thermal Protection System Damage Experienced During STS-118," *J. Spacecraft Rockets*, Vol. 46, No. 6, November-December 2009, pp. 1110–1116.

[56] Palmer, G. E. and Wright, M. J., "A Comparison of Methods to Compute High Temperature Gas Thermal Conductivity," *AIAA Paper 2003-3913*, June 2003, presented at the 36th AIAA Thermophysics Conference, Orlando, FL.

[57] Palmer, G. E. and Wright, M. J., "Comparison of Methods to Compute High-Temperature Gas Viscosity," *J. Thermophys. Heat Tr.*, Vol. 17, No. 2, April-June 2003, pp. 232–239.

[58] Park, C., "Problems of Rate Chemistry in the Flight Regimes of Aeroassisteed Orbital Transfer Vehicles," *AIAA Paper 1984-1730*, June 1984, presented at the 19th AIAA Thermophysics Conference, Snowmass, CO.

[59] Parker, J. G., "Rotational and Vibrational Relaxation in Diatomic Gases," *Phys. Fluids*, Vol. 2, No. 4, July-August 1959, pp. 449–462.

[60] Ramshaw, J. D., "Self-Consistent Effective Binary Diffusion in Multicomponent Gas Mixtures," *J. Non-Equilib. Thermodyn.*, Vol. 15, No. 3, 1990, pp. 295–300.

[61] Ried, R. C., "Orbiter Entry Aerothermodynamics," *NASA CP-2342, Part 2*, 1983, pp. 1051–1061.

[62] Roveda, R., Goldstein, D. B., and Varghese, P. L., "Hybrid Euler/Particle Approach for Continuum/Rarefied Flows," *J. Spacecraft Rockets*, Vol. 35, No. 3, May-June 1998, pp. 258–265.

[63] Scalabrin, L. C., *Numerical Simulation of Weakly Ionized Hypersonic Flow over Reentry Capsules*, Ph.D. thesis, University of Michigan, 2007.

[64] Schwartzentruber, T. E., *A Modular Particle-Continuum Numerical Algorithm for Hypersonic Non-Equilibrium Flows*, Ph.D. thesis, University of Michigan, 2007.

[65] Schwartzentruber, T. E. and Boyd, I. D., "A Hybrid Particle-Continuum Method Applied to Shock Waves," *J. Comput. Phys.*, Vol. 215, No. 2, July 2006, pp. 402–416.

[66] Schwartzentruber, T. E., Scalabrin, L. C., and Boyd, I. D., "A Modular Particle-Continuum Numerical Method for Hypersonic Non-Equilibrium Gas Flows," *J. Comput. Phys.*, Vol. 225, No. 1, July 2007, pp. 1159–1174.

[67] Schwartzentruber, T. E., Scalabrin, L. C., and Boyd, I. D., "Hybrid Particle-Continuum Simulations of Hypersonic Flow over a Hollow-Cylinder-Flare Geometry," *AIAA J.*, Vol. 46, No. 8, August 2008, pp. 2086–2095.

[68] Schwartzentruber, T. E., Scalabrin, L. C., and Boyd, I. D., "Multiscale Particle-Continuum Simulations of Hypersonic Flow over a Planetary Probe," *J. Spacecraft Rockets*, Vol. 45, No. 6, November-December 2008, pp. 1196–1206.

[69] Sherman, F. S., "Shock-Wave Structure in Binary Mixtures of Chemically Inert Perfect Gases," *J. Fluid Mech.*, Vol. 8, No. 3, July 1960, pp. 465–480.

[70] Stallcop, J. R., Levin, E., and Partridge, H., "Transport Properties of Hydrogen," *J. Thermophys. Heat Tr.*, Vol. 12, No. 4, October-December 1998.

[71] Stallcop, J. R., Partridge, H., Walch, S. P., and Levin, E., "H-N2 Interaction Energies, Transport Cross Sections, and Collision Integrals," *J. Chem. Phys.*, Vol. 97, No. 5, September 1992, pp. 3431–3436.

[72] Steger, J. L. and Warming, R. F., "Flux Vector Splitting of the Inviscid Gasdynamics Equations with Application to Finite-Difference Methods," *J. Comput. Phys.*, Vol. 40, 1981, pp. 263–293.

[73] Stephani, K. A., *Development of a Hybrid DSMC/CFD Method for Hypersonic Boundary Layer Flow over Discrete Surface Roughness*, Ph.D. thesis, University of Texas at Austin, 2012.

[74] Stephani, K. A., Goldstein, D. B., and Varghese, P. L., "Consistent Treatment of Transport Properties for Five-Species Air Direct Simulation Monte Carlo/Navier-Stokes Applications," *Phys. Fluids*, Vol. 24, No. 7, July 2012, pp. 1–23.

[75] Stephani, K. A., Goldstein, D. B., and Varghese, P. L., "A Non-Equilibrium Surface Reservoir Approach for Hybrid DSMC/Navier-Stokes Particle Generation," *J. Comput. Phys.*, Vol. 232, 2013, pp. 468–481.

[76] Sun, Q. and Boyd, I. D., "Evaluation of Macroscopic Properties in the Direct Simulation Monte Carlo Method," *J. Thermophys. Heat Tr.*, Vol. 19, No. 3, July-September 2005, pp. 329–335.

[77] Sutton, K. S. and Gnoffo, P. A., "Multi-Component Diffusion with Application to Computational Aerothermodynamics," *AIAA Paper 1998-2575*, 1998, presented at the 7th AIAA/ASME Joint Thermophysics and Heat Transfer Conference.

[78] Tannehill, J. C., Anderson, D. A., and Pletcher, R. H., *Computational Fluid Mechanics and Heat Transfer*, Taylor and Francis, 1997.

[79] Verhoff, A. M. and Boyd, I. D., "Extension of a Hybrid Particle-Continuum Method for a Mixture of Chemical Species," *28th International Symposium on Rarefied Gas Dynamics*, AIP Conf. Proc. 1501, 2012, pp. 342–349.

[80] Verhoff, A. M. and Boyd, I. D., "Consistent Modeling of Rotational Nonequilibrium in a Hybrid Particle-Continuum Method," *AIAA Paper 2013-3145*, June 2013, presented at the 44th AIAA Thermophysics Conference, San Diego, CA.

[81] Verhoff, A. M. and Boyd, I. D., "Further Development of a Hybrid Particle-Continuum Method for Transitional Hypersonic Flows," *29th International Symposium on Rarefied Gas Dynamics*, AIP Conf. Proc. 1628, 2014, pp. 510–518.

[82] Vincenti, W. G. and Kruger, C. H. J., *Introduction to Physical Gas Dynamics*, John Wiley and Sons, 1965.

[83] Wadsworth, D. C. and Erwin, D. A., "One-Dimensional Hybrid Continuum/Particle Simulation Approach for Rarefied Hypersonic Flows," *AIAA Paper 1990-1690*, June 1990, presented at the 5th AIAA/ASME Joint Thermophysics and Heat Transfer Conference.

[84] Wadsworth, D. C. and Erwin, D. A., "Two-Dimensional Hybrid Continuum/Particle Approach for Rarefied Flows," *AIAA Paper 1992-2975*, July 1992, presented at the 23rd AIAA Plasmadynamics and Lasers Conference.

[85] Wagner, W., "A Convergence Proof for Bird's Direct Simulation Monte Carlo Method for the Boltzmann Equation," *J. Stat. Phys.*, Vol. 66, No. 3, 1992, pp. 1011–1044.

[86] Wang, W.-L. and Boyd, I. D., "A New Energy Flux Model in the DSMC-IP Method for Nonequilibrium Flows," *AIAA Paper 2003-3774*, June 2003, presented at the 36th AIAA Thermophysics Conference, Orlando, FL.

[87] Wang, W.-L. and Boyd, I. D., "Hybrid DSMC-CFD Simulations of Hypersonic Flow over Sharp and Blunted Bodies," *AIAA Paper 2003-3644*, June 2003, presented at the 36th AIAA Thermophysics Conference, Orlando, FL.

[88] Wang, W.-L. and Boyd, I. D., "Predicting Continuum Breakdown in Hypersonic Viscous Flows," *Phys. Fluids*, Vol. 15, No. 1, January 2003, pp. 91–100.

[89] Wijesinghe, H. S., *Hybrid Atomistic-Continuum Formulations for Gaseous Flows*, Ph.D. thesis, Massachusetts Institute of Technology, September 2003.

[90] Wright, M. J., Bose, D., Palmer, G. E., and Levin, E., "Recommended Collision Integrals for Transport Property Computations, Part 1: Air Species," *AIAA J.*, Vol. 43, No. 12, December 2005, pp. 2558–2564.

[91] Wu, J. S., Lian, Y.-Y., Cheng, G., Koomullil, R. P., and Tseng, K.-C., "Development and Verification of a Coupled DSMC-NS Scheme Using Unstructured Mesh," *J. Comput. Phys.*, Vol. 219, No. 2, December 2006, pp. 477–1014.

[92] Zhang, C. and Schwartzentruber, T. E., "Inelastic Collision Selection Procedures for Direct Simulation Monte Carlo Calculations of Gas Mixtures," *Phys. Fluids*, Vol. 25, No. 10, October 2013, pp. 1–13.